Syracuse University

SURFACE

Dissertations - ALL

December 2017

Adsorption of Iodine and Water on Silver-Exchanged Mordenite

Yue Nan
Syracuse University

Follow this and additional works at: https://surface.syr.edu/etd

Part of the Engineering Commons

Recommended Citation

Abstract

The reprocessing of used nuclear fuel to recover the fissile materials generates off gases including radioactive nuclides namely ^{3}H (tritiated water, H^{3}HO), ^{129}I, ^{85}Kr, ^{135}Xe, and ^{14}C. Due to its high quantity in off-gas streams and long half-life (1.59 million years), ^{129}I removal from the off-gas streams is a significant objective of off-gas treatment.

^{129}I retention by solid adsorbents was recognized a better strategy in comparison to liquid scrubbers due to the simplicity of system design and low cost. Among the studied adsorbents, reduced silver-exchanged mordenite (Ag^{0}Z) was widely recognized as the state-of-art adsorbent for iodine removal. It has been selected to be used in the Hanford Treatment and Immobilization Plant in Washington State, US, to control releases of the radioactive iodine in off-gases of spent nuclear fuel reprocessing facilities.

Previous studies have shown the outstanding performance of Ag^{0}Z for adsorption of both molecular iodine and organic iodide. However, the detailed adsorption kinetics of I$_2$ on Ag^{0}Z was never reported. Therefore, this study included determining the adsorption dynamics of I$_2$ adsorption on Ag^{0}Z through continuous -flow experiments and data analyses by kinetic models. Mass transfer, diffusion and reaction processes involved in the adsorption process were evaluated.

In addition, one issue that has to be addressed when using Ag^{0}Z for iodine removal is the potential co-adsorption of other gas species, among which is H$_2$O vapor. Mordenites have been shown to have a considerable adsorption capacity for H$_2$O vapor, which is also a major component in the off-gases of spent nuclear fuel reprocessing facilities. Therefore, understanding the kinetics of H$_2$O vapor adsorption on Ag^{0}Z is necessary for a better design

of off-gas treatment systems. The kinetics and equilibrium of H_2O adsorption on Ag^0Z were studied. Uptake curves and isotherms were obtained at temperatures from 25 to 200 $^{\circ}C$. Data were analyzed by kinetic and isotherm models, and parameters related to the adsorption kinetics and thermodynamics were determined.

Moreover, the co-adsorption on I_2 and H_2O on Ag^0Z were studied. Co-adsorption uptake curves were obtained to determine the performance of Ag^0Z in humid gas streams and effect of H_2O concentration on the capacity of Ag^0Z for I_2 adsorption. It was found that H_2O vapor in the gas stream deactivated the iodine adsorption sites (Ag particles) in Ag^0Z. The deactivation mechanism was determined by chemical analyses with XRD and SEM-EDX.

Adsorption of Iodine and Water on Silver-Exchanged Mordenite

by

Yue Nan

B.S. Chemical Engineering, Tianjin University of Sci & Tech, 2011

M.S. Chemical Engineering, Syracuse University, 2013

Dissertation

Submitted in partial fulfillment of the requirements for the degree of

Doctor of Philosophy in Chemical Engineering

Syracuse University

December 2017

Acknowledgment

is invaluable. I would also like to thank undergraduate students, Tyler B Crowl and Siqi Tang, for their friendship and assistance on the experimental work.

Special thanks to my parents, Zhiping Nan and Xian'e Liang, and my sister, Fang Nan, for their endless love, support and encouragements.

I would like to express my sincere thankfulness to my wife, Wanqi Yu. Completion of this work could not be possible without her love and being understanding and supportive.

Contents

List of Figures

xi

List of Tables

Chapter 1. Introduction[*]

Nuclear power, as clean energy, has significant advantages comparing to fossil fuels in terms of low carbon emissions and high sustainability.[1-2] Although it is a mature technology and contributes a great portion to the total power generation in many countries such as France and Belgium, the development of nuclear technology never stops. It has been a major objective in electricity production for more and more countries. In the United States, there are more than 100 nuclear power statements in operation, and the energy generated shares about 20% of the total energy used by the country.[3]

The fission reaction of uranium in a nuclear power reactor results in numerous radioactive products which are subsequently mixed with the unreacted uranium as spent nuclear fuel. Instead of long-term storage, the spent nuclear fuel can be reprocessed, and the recovered fuel can be fed back to the fuel cycle. Through reprocessing, fissile materials such as uranium-235, plutonium-239 and minor actinides of high value can be retrieved for subsequent nuclear energy production.[4-5] During the head-end reprocessing processes as shown in **Figure 1-1**, several volatile radioactive nuclides including ^{129}I, ^{3}H, ^{85}Kr, ^{135}Xe

[*] Permission granted by American Chemical Society and John Wiley and Sons to use the text of published articles [63,88,122] in this chapter.

66. Nan, Y.; Ladshaw, A. P.; Yiacoumi, S.; Tsouris, C.; DePaoli, D. W.; Tavlarides, L. L., Co-adsorption of I$_2$ and H$_2$O on Ag0Z and Kinetics of Silver-Iodine Reaction. In 2016 ANS Anual Meeting, Transactions of the American Nuclear Society, New Orleans, LA, 2016; Vol. 114, pp 165-166.

88. Nan, Y.; Tavlarides, L. L.; DePaoli, D. W., Adsorption of iodine on hydrogen-reduced silver-exchanged mordenite: Experiments and modeling. AIChE Journal 2017 63 (3), 1024 – 1035.

122. Abney, C. W.; Nan, Y.; Tavlarides, L. L., X-ray Absorption Spectroscopy Investigation of Iodine Capture by Silver-Exchanged Mordenite. Industrial & Engineering Chemistry Research 2017, 56 (16), 4837-4846.

and ^{14}C release into the off gases and require further management to prevent uncontrolled

environmental release.[4, 6]
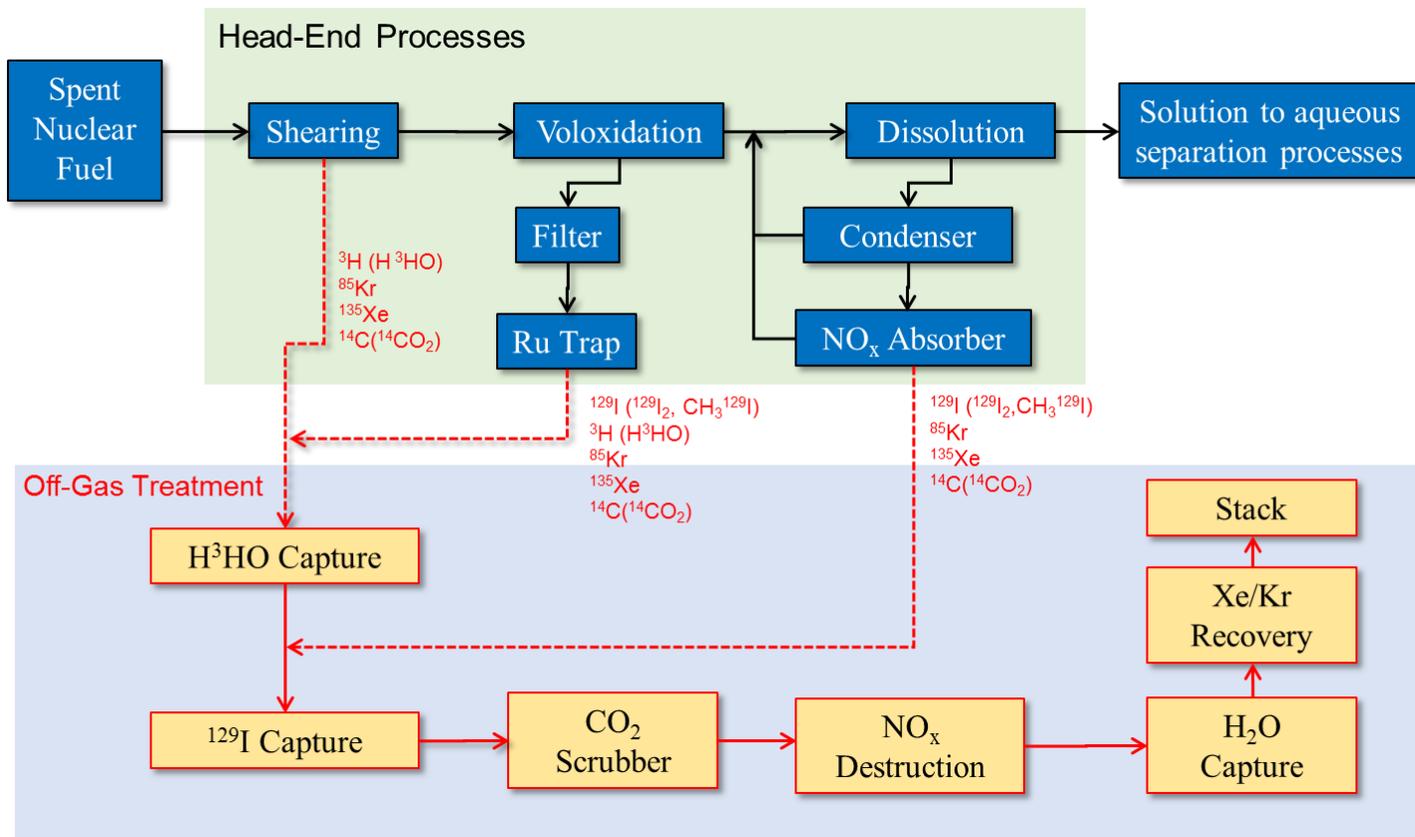
Figure 1-1. Head-end processes of spent nuclear fuel reprocessing and off-gas treatment systems.[7]

Radioactive iodine is a primary volatile radionuclide released in the off-gas streams of spent nuclear fuel reprocessing facilities.[8-13] The adverse impact on human health and long decay half-life (15.7 million years) make the removal and immobilization of gaseous ^{129}I crucial. The U.S. Environment Protection Agency (EPA) and Nuclear Regulatory Commission (NRC) have issued regulatory emission limits for radioactive elements. According to the US Code of Federal Regulations (CFR) Title 10 Part 20 and Title 40 Part 190,[14-15] the release limit for ^{129}I from a LWR fuel cycle is 1.9×10^8 Bq/Gw(e)year, which requires the decontamination factor (DF)- the ratio between initial and final radioactivity following a separation - to be at least 200 before off-gas streams are exhausted to the environment.[7, 16] It is noted that with a half-life of 16 million years it will be a challenge that has to be considered when designing the strategy for disposal as described by Burger and recently by Jubin. [17-18]

Liquid scrubbing systems using caustic solution, nitric acid or Mercurex solution have been considered for capturing iodine, [19-22] but shortcomings exist. These systems are capable of removing iodine at high concentrations but are less efficient with dilute streams which could be as low as 0.1 – 0.5 ppm.[23-25] Additionally, the corrosive systems require acid or alkaline resistant constructions and complicated procedures for solution disposal, especially for the IODOX process which uses essentially 100% nitric acid for oxidation of organic iodides and hydrolysis-oxidation of free iodine to the stable iodate form.

Using solid adsorbents to remove gaseous iodine can avoid the complication in system design and high maintenance costs. Studies on activated carbon, macro reticular resins, silver impregnated alumina silicates, silver nitrate impregnated silicic acid (AC-6120) and silver exchanged molecular sieves have shown potentials as alternatives to liquid

scrubbers.[25-36] However, not all of these adsorbents are good options for iodine retention under off-gas conditions. For example, activated carbon does not perform well at high temperatures as it has a relatively low ignition point, and it loses iodine adsorption capacity with the presence of NO and NO_2 in off-gas streams. Also, the reaction of carbon with NO_x may form unstable and explosive compounds which are entirely undesired.[22, 35] Although recent literature showed good performances of emerging materials such as chalcogels,[37-40] metal-organic frameworks,[41-46] metals supported on Engelhard titanosilicate,[36, 47-49] and nanostructured inorganic adsorbents,[50-52] reduced silver-exchanged mordenite (Ag^0Z) was widely recognized as state-of-art for iodine retention.[6, 53-54] Mordenite is high in silicon-aluminum ratio (typically 5:1), and therefore is thermally stable at high temperatures and resistant to acidic off-gas streams. Even though studies[33, 55] have shown the existence of other chemical forms in addition to the primary form (AgI) when iodine is adsorbed into Ag zeolites, the stronger Ag-I chemical bond makes AgZ preferred over adsorbents that adsorb iodine molecules physically.

The adsorption of molecular iodine (I_2) on Ag^0Z has been studied since the 1970s, and results have demonstrated the high capacity of Ag^0Z for adsorbing I_2 in dry air streams.[56-61] However, the micro-scale adsorption process and detailed kinetics remain unexplored. There are no data available on the kinetics of I_2 adsorption on Ag^0Z, which are important for the thorough understanding of the adsorption mechanisms and model development for simulating the off-gas treatment units in spent nuclear fuel reprocessing facilities. Accordingly, the objective of this study included determination of the kinetics on a micro-scale and shortened the data gap in the open literature.

The real off-gas streams include several other gas species, and the adsorption of iodine on Ag^0Z would proceed with the co-adsorption of other gases. One issue that has to be addressed when using Ag^0Z for iodine removal is the potential co-adsorption with tritiated H_2O vapor, which is the most abundant components in the off-gas streams. Ag^0Z has been shown to have a considerable adsorption capacity for H_2O in gas phases, and previous co-adsorption studies of iodine and H_2O vapor have demonstrated that the presence of H_2O vapor influences the performance of Ag^0Z for iodine adsorption.[62-66] Therefore, it is crucial to understand the co-adsorption process of iodine and H_2O for better design of off-gas treatment systems using Ag^0Z. To understand the co-adsorption, the adsorption process of each single component needs to be first determined. Thus, in addition to I_2 adsorption, H_2O adsorption on Ag^0Z was also studied in this work, and finally, the co-adsorption of I_2 and H_2O on Ag^0Z were investigated.

In addition, this study was also conducted to support the development and verification of models for the off-gas treatment systems. Efforts are being made by the U.S. Department of Energy (DOE) Fuel Cycle Research and Development (FCR&D) on developing a dynamic plant-level modeling and simulation toolkit to support the development of sustainable nuclear fuel systems. The toolkit will include a unit operation model to simulate the adsorption processes of the off-gases by columns of solid adsorbents.[23] A complex model has been preliminarily developed to predict the adsorption processes for single and multi-component in the adsorbent columns, which requires the input of the parameters related to the adsorbents properties and adsorption kinetics and equilibrium, as well as experimental adsorption data to validate the model. [67] This requires fundamental laboratory studies to determine the properties of the adsorption system and

collect adsorption data of kinetics and equilibrium. Previous work has shown good examples of modeling development and validation supported by experimental studies.

Towards the objectives mentioned above, I_2 and H_2O adsorption were systematically studied, respectively, via adsorption experiments with single-layer Ag^0Z pellets in continuous-flow adsorption systems of high precision. Kinetic and equilibrium data of I_2 and H_2O adsorption on Ag^0Z were obtained at wide ranges of conditions that covered the potential operating conditions of the off-gas treatment systems. Adsorption mechanisms were determined using different material characterization techniques. Kinetics of the adsorption process work studied with various models that describe the inter-crystalline and intro-crystalline mass transfer process. The rate controlling factors and parameters associated with the adsorption processes were determined. Adsorption equilibria were analyzed with isothermal models, and thermal dynamic parameters were obtained. In addition, co-adsorption of H_2O and I_2 were studied experimentally. The impact of H_2O vapor in the gas stream on the I_2 adsorption capacity of Ag^0Z were determined. Mechanism of the co-adsorption was also assessed.

Chapter 2. Literature Review

2.1. Performance of Ag^0Z for Iodine Adsorption

The retention of radioactive iodine (^{129}I) by solid adsorbents has been investigated for decades. Experimental and analytical results in numerous studies have shown that Ag^0Z is the most outstanding adsorbent for iodine removal from used nuclear fuel processing off-gases. It has been selected to be used in the Hanford Treatment and Immobilization Plant in Washington State, US, to control releases of ^{129}I in off-gases of spent nuclear fuel reprocessing facilities.[55, 61, 68]

Staple et al.[56] and Thomas et al.[57] first investigated the I_2 adsorption capacity of both reduced and unreduced AgZ via column tests. Results showed that the reduced Ag^0Z performed better than the unreduced AgZ. A 17 wt.% of I_2 loading capacity was achieved at the optimal adsorption temperature of 150 ^oC with the Ag^0Z containing 20 wt.% of Ag. The consequent regeneration tests indicated that the I_2 capacity could be well maintained for after a 13-recycle test, and 20 % capacity loss was observed at the 14th cycle.

Jubin[69], in 1980, studied the adoption of methyl iodide (CH_3I), the second abundant volatile iodine species in off-gas streams, on Ag^0Z. It was found that Ag^0Z has a weaker adsorption capacity for CH_3I, 3.4 wt.%, than I_2. Kinetics of CH_3I on Ag^0Z pellets was determined in his later study.[70] Via analyses with kinetic models including the shrinking core model, volume reaction model, and micropore/macropore diffusion models, the adsorption process of CH_3I on Ag^0Z pellets was found to be a macropore diffusion controlling process. The macropore diffusivity of CH_3I in Ag^0Z pellets was determined.

Since then, numerous studies have been conducted on iodine (I_2 and CH_3I) adsorption by Ag^0Z [7, 10, 23-25, 32-33, 60-62, 71-102]. The adsorption tests mainly focused on evaluating the performances of Ag^0Z deep beds (columns) under off-gas conditions. Experiments were performed with high gas velocity around 10 m/min (real off-gas streams are expected at high gas velocity) with iodine concentrations ranged between 40 ppb to ~80 ppm at various temperatures. The concentration of the iodine species in the off-gas steam varies with generating source. The off-gases generated from the Dissolution process (**Figure 1-1**) has much higher iodine concentration (ppm level) than that from the Voloxidation process (ppb level). Results indicated that Ag^0Z columns were able to achieve the DF (decontamination factor- the ratio between initial and final radioactivity following a separation) required by the regulatory requirements. The optimal adsorption temperature for I_2 and CH_3I on Ag^0Z was found to be 150 ^oC.

It was noted that, in the previous studies mentioned above, the reduction conditions for reduction of AgZ varied. The AgZ was reduced in a hydrogen stream at temperatures between 150-500 ^oC for a period ranged from hours to days. For instance, in the study by Thomas et al.,[57] Ag^0Z was prepared by reducing AgZ (Ag content: 20 wt.%) at 500 ^oC for 24 hours. The same reduction conditions were used by Scheele et al.[61] In comparison, Ag^0Z (Ag content: 9.5 wt.%) used in the study by Bruffey et al.[79] was reduced at 170 ^oC for ten days. The different reduction conditions could be due to the differences in Ag content and possible physical/chemical differences between the adsorbents.

2.2. Mechanism of AgZ Reduction and I_2 Adsorption

Zhao et al.[103] studied the mechanism and kinetics of Ag^0Z reduction in hydrogen streams using the in situ pair distribution function (PDF) methods. They reported the

formation of Ag nanoparticle inside the channels and on the surfaces of the mordenite crystals. According to the modeling results, the formation of Ag nanoparticles occurs in 5 steps: 1) Ag^+ are reduced to Ag^0 in the 8-member ring (MR) pores and 12 MR channels at different rates; 2) the Ag^0 in the 8 MR migrates to 12 MR channels; 3) Ag^0 forms clusters in the 12 MR channels; 4) the Ag^0 clusters in 12MR channels migrates to the external mordenite surface; and 5) Ag^0 clusters aggregate into nanoparticles. By comparing the PDF data at different reduction temperatures between $130 - 227\ ^{\circ}C$ and periods up to 12 hours, they found that the amount and size of the nanoparticles increased with reduction temperature and time.

The mechanism for I_2 adsorption on Ag^0Z was investigated by Chapman et al. through a differential pair distribution function (d-PDF) study.[49] They reported that I_2 was chemically adsorbed by the Ag particles on Ag^0Z via formation of AgI. By analyses of the crystalline structure of the products, it was found that the silver-iodine reaction at the surface of the Ag^0Z crystals mainly formed γ-AgI (in a cubic zincblende type structure) while that at the inside of the crystals formed α-AgI (in a face-centered cubic structure). The nanoscale AgI product showed different polymorphic forms to the bulk AgI, which presents preferentially in α-AgI form at temperatures below $147\ ^{\circ}C$.[104] The particle size of the α-AgI in the crystal channels was estimated ~7 Å, consistent with the pore apertures in mordenite. It was proposed that α-AgI formed inside the channels support affording stabilization of the phase at lower temperatures.

2.3. Adsorption of H_2O in Mordenites

The adsorption of H_2O on mordenites has been extensively studied.[63-64, 105-113] Chibani et al.[64] investigated the adsorption of H_2O and iodine (I_2/CH_3I) in different cation-exchanged mordenites including H^+, Na^+, Cu^+ and Ag^+ via density functional theory (DFT) studies. They found that, for Ag and Cu mordenites (AgZ and CuZ), H_2O was adsorbed preferentially in the small channels (5Å) or the side pockets of mordenite crystals while iodine preferred the large (main) channels (7Å). Note that the AgZ studied was unreduced, which had Ag^+ in the mordenite structure. In contrast, for H modenite (HZ), H_2O is always much more strongly adsorbed than ICH_3 and I_2 in both main and small channels, as well as side pockets. That means H_2O is preferentially adsorbed into HZ over the iodine species. Chibani and co-workers[105] recently extended the DFT study to divalent cation (Cu^{2+}, Pb^{2+}, and Hg^{2+})-exchanged mordenites for adsorption of I_2, ICH_3, H_2O, CO, $ClCH_3$, and Cl_2. The interaction energy of the adsorbates to the mordenites was evaluated and compared.

Similar results were obtained by Diaby[106] and Devautour et al.[107] through determination of the cation-surface interaction energy of NaZ for H_2O adsorption and localization of H_2O and Na^+ in NaZ by thermally stimulated current measurement. The surface energy variation during the adsorption of H_2O on NaZ was measured using dielectric relaxation by Dauillard et al.[108] Results showed that the extraction energy (in eV) deduced from the dielectric measurement decreased as the adsorbed quantity of H_2O (in mol per unit cell) increased.

Kawamura et al.[109] compared the adsorption of H_2O and hydrogen on different cation-exchanged mordenites including Mn-, Fe-, Ni-, Cu-, Pd-, and Ag mordenites for use to tritium recovery systems. AgZ showed a fairly large adsorption capacity of hydrogen

isotopes at -196 $^{\circ}$C in comparison with Ca–MOR or MS5A, and a maximum H_2O adsorption capacity of ~18 wt.% at 25 $^{\circ}$C.

2.4. Co-adsorption of H_2O and I_2

Tritium as in tritiated H_2O release in nuclear fuel processing off-gases, along with the other radioactive species, can be efficiently removed from off-gas streams using molecular sieves, specifically of the 3A type (3AMS). Studies have demonstrated the excellent capability of 3AMS for H_2O adsorption, up to a 23 wt.% maximum equilibrium capacity. The isotherms and kinetics of H_2O adsorption on MS3A were reported by Lin et al. [114-116] Breakthrough curves of H_2O on 3AMS column was obtained by Spencer et al.[77] However, in the off-gas treatment system, radioactive iodine can be co-adsorbed on the 3AMS,[117] elevating the low-level tritium waste to a high-level waste, which makes the tritium treatment process complicated. This raises a issue that iodine and H_2O co-adsorb on Ag^0Z, and the co-adsorption of H_2O may impact the iodine absorption performance of Ag^0Z.

Spencer and co-works proposed a co-adsorption system for iodine and H2O in a test-plan report.[77] AgZ columns followed by 3AMS columns were designed to remove iodine and H_2O in sequence from the synthetic off-gas stream. The proposed system included a minimum of two Ag^0Z columns such that one column is in service for iodine/ H_2O adsorption while the other column is in a desorption or replacement mode. A similar design was proposed for the 3AMS column. Unfortunately, the test results were not available to the public. The test report was cited in their later work. [62]

Nan et al.[65-66] later reported the co-adsorption I_2 and H_2O on Ag^0Z. The presence of H_2O vapor in the gas stream had a significant adverse impact on the I_2 adsorption

capacity of Ag^0Z. For instance, a ~40% I_2 adsorption capacity decrease was observed when co-adsorbed with H_2O at 150^oC in a humid gas stream of dew point -16^oC. More significant impacts were found at higher H_2O concentrations of the gas streams. The results also showed that the I_2 capacity was impacted by the strongly adsorbed H_2O, the H_2O does not desorb from Ag^0Z in dry air purging, which implied that the reduction of I_2 adsorption capacity was due to a deactivation of I_2 adsorption sites. However, the detailed deactivation mechanism was not clear.

Chapter 3. Experimental[†]

3.1. Materials

The IONEX-TYPE AgZ (Ag-900 E16, Lot# 111515-1) was purchased from Molecular Products, Inc. The AgZ pellets are cylindrical extrudates with an average diameter of 1.6 mm as indicated by the supplier. It was manufactured with a highly acid-resistant binder (aluminosilicate). The actual size of the pellets as received distributed between 10 and 16 mesh and was further narrowed down with a 12-mesh stainless steel screen to 1.8 mm (average equivalent spherical diameter). The diameter was obtained by calculating the diameter of a sphere of equivalent volume to the cylindrical AgZ pellet. The Ag^0Z was prepared by reduction in 4% H_2/96% Argon.

The physical properties and characteristics of the Ag^0Z reduced at optimal conditions are shown in **Table 3-1**. The average silver content as indicated by the supplier was 11.9 wt. %, which is 12.0 wt.% (1.10 mmol Ag/g) on a dry basis, and the result of the inductively coupled plasma optical emission spectrometer (ICP-OES) performed in this study indicated the approximate formula of $Ag_{4.09}H_{4.12}(AlO_2)_{8.21}(SiO_2)_{43.26} \cdot xH_2O$. A trace amount of Na, Ca, K and Fe were also detected by ICP-OES, which could be introduced

---

[†] Permission granted by American Chemical Society and John Wiley and Sons to use the text of published articles[63,88,122] in this chapter.

63. Nan, Y.; Lin, R.; Liu, J.; Crowl, T. B.; Ladshaw, A.; Yiacoumi, S.; Tsouris, C.; Tavlarides, L. L., Adsorption Equilibrium and Modeling of Water Vapor on Reduced and Unreduced Silver-Exchanged Mordenite. Industrial & Engineering Chemistry Research 2017, 56 (28), 8095-8102.

88. Nan, Y.; Tavlarides, L. L.; DePaoli, D. W., Adsorption of iodine on hydrogen-reduced silver-exchanged mordenite: Experiments and modeling. AIChE Journal 2017 63 (3), 1024‒1035.

122. Abney, C. W.; Nan, Y.; Tavlarides, L. L., X-ray Absorption Spectroscopy Investigation of Iodine Capture by Silver-Exchanged Mordenite. Industrial & Engineering Chemistry Research 2017, 56 (16), 4837-4846.

during the manufacturing process as impurities. In theory, if the 12.0 wt. % (1.10 mmol Ag/g) of silver was reacted with I_2 completely through the reaction $2Ag + I_2 \rightarrow 2AgI$ to form AgI, the theoretical maximum I_2 adsorption capacity of the Ag^0Z would be 14.1 wt. % (1.10 mmol I /g). It is noted that before reduction Ag is mainly in the crystalline framework of AgZ as $Ag^+_x (AlO_4)^{-1}_x (SiO_2)_{5x}$ and that after reduction in hydrogen at 673 K for 24 hours or more severe conditions, Ag was shown to be reduced to Ag^0 by XRD and XAFS analysis.[51-53] In addition, cylinder gases including compressed air, N_2, and 4% H_2 /96% Ar mixture used in this study were purchased from Airgas Inc.

Table 3-1. Physical properties of Ag^0Z.

Property/Characteristic	Value
Silver content	11.9 wt. %
Moisture in AgZ as received	1.2 wt.%
Theoretical maximum iodine capacity	14.0 wt.%
Diameter of cylindrical pellet	1.6 mm
Equivalent spherical radius, R_a	0.9 mm
Radius of microparticles, R_i	1.14 μm
Bulk density of pellet, ρ_p	1.87 g/cm^3
Real density, ρ_r	3.057 g/cm^3
Porosity of pellet, ε_p	0.384
BET surface area, S	178.9 m²/g
t-plot micropore volume, v_i	0.077 cm³/g

3.2. Experimental Setup and Procedure

3.2.1. Reduction of AgZ

The decrease of AgZ to Ag^0Z was realized with a simple experimental setup as shown in **Figure 3-1**. The AgZ pellets were loaded into the glass reduction column (I.D. = 3cm) and dried with a N_2 flow (500 ml/min) at the desired temperature. The gas stream was preheated by passing through the glass coils outside the reduction column. Then 4% H_2 /96% Argon flow was passed through the column for reduction. The reason for using 4% H_2 was that the lower explosive limit (LEL) for H_2 was 4%. When the reduction was finished, the pellets were purged with N_2 again for another 4 hours to remove the residual H_2 inside the pellets, and then were cooled down in the column with the continued N_2 purge. Wide ranges of reduction temperatures (170 – 500 °C) and reduction times (24 -336 hours) were studied to determine the optimal reduction conditions.
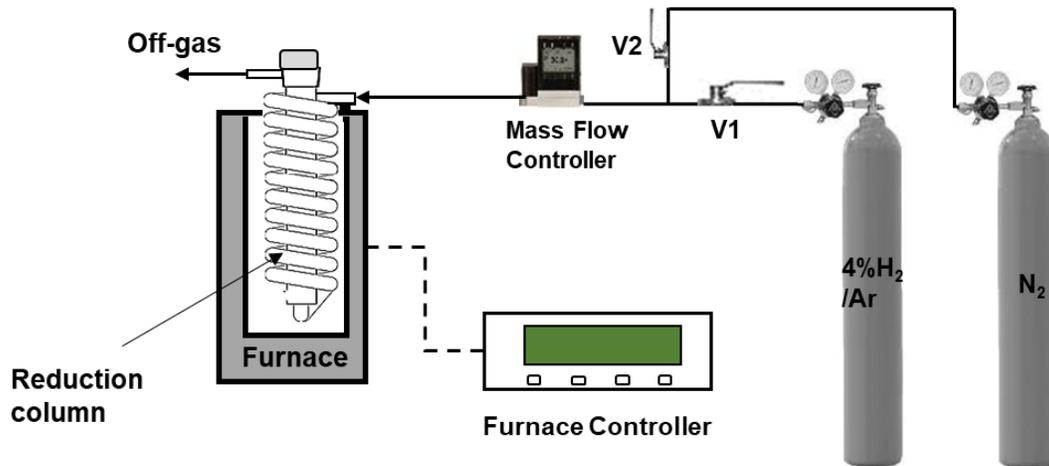
Figure 3-1. Experimental setup for reduction of AgZ.

3.2.2. Batch experiments

To determine the optimal reduction conditions, a batch experimental system was used to compare the capacity of Ag^0Z reduced at different conditions. As shown in **Figure 3-2,** two sealed glass bottles were used as the batch container. Inside each bottle, there was a container for I_2 solids and four screen trays suspended on the lid for holding Ag^0Z samples. The air in the bottles was ambient air, and the bottles were placed in the laboratory at a constant temperature of 22 °C, so the two systems had unique humidity and temperature. Bottle 1 was I_2-free, while Bottle 2 was loaded with I_2 solids. Before batch experiments, the Ag^0Z samples were degassed using an ASAP 2020 Physisorption Analyzer under vacuum at 200 °C for 8 hours to remove residual H_2O prior to the experiments. Samples were weighed initially and loaded onto the screen trays in Bottle 1 for pre-equilibration with H_2O (moisture in the air). They were weighed every 24 hours until no further weight gain was observed, and then were transferred to Bottle 2 for I_2 adsorption.
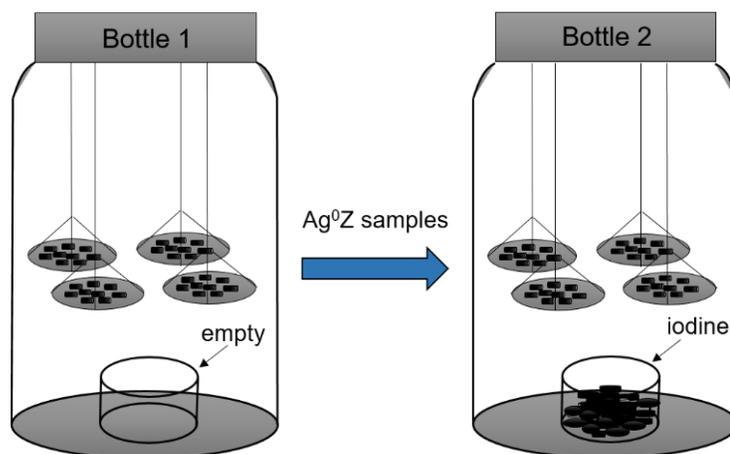
Figure 3-2. Batch experimental setup for comparing the capacities of Ag^0Z reduced at different conditions. After Ag^0Z were pre-equilibrated in Bottle 1, they were transferred to Bottle 2 for I_2 adsorption.

3.2.3. Continuous-flow adsorption experiments

3.2.3.1. I_2 adsorption

Two continuous-flow iodine adsorption systems were designed and constructed. A schematic diagram of one system is shown in **Figure 3-3**. Each of the systems was comprised of an iodine generation unit, a microbalance unit, a furnace and a data acquisition system. I_2 vapors were generated by the dynacalibrators (VICI, Model 450 and 500). By varying the temperature of the dynacalibrator and flow rates of the carrier and dilution streams, the concentrations of I_2 in the gas stream were precisely controlled. A microbalance with a sensitivity of 0.1 μg was used in each system to measure the mass change of adsorbents during the adsorption process. It was connected to a data acquisition unit, which had a designed program to record the data at desired time intervals. A stainless-steel screen tray inside a glass adsorption column was suspended from the microbalance and loaded with a single-layer of Ag^0Z pellets. The glass column (I.D.: 30mm) was wrapped with glass coils, through which the flowing gas stream was pre-heated. There were two thermocouples at both inside and outside of the column to ensure the gas was preheated to the desired adsorption temperature. A furnace with an accuracy of 0.1 ºC was used in each system for desired temperatures. Photographs of the I_2 adsorption systems and details of the adsorption column and the screen tray with Ag^0Z loaded are shown in **Figure 3-4**.
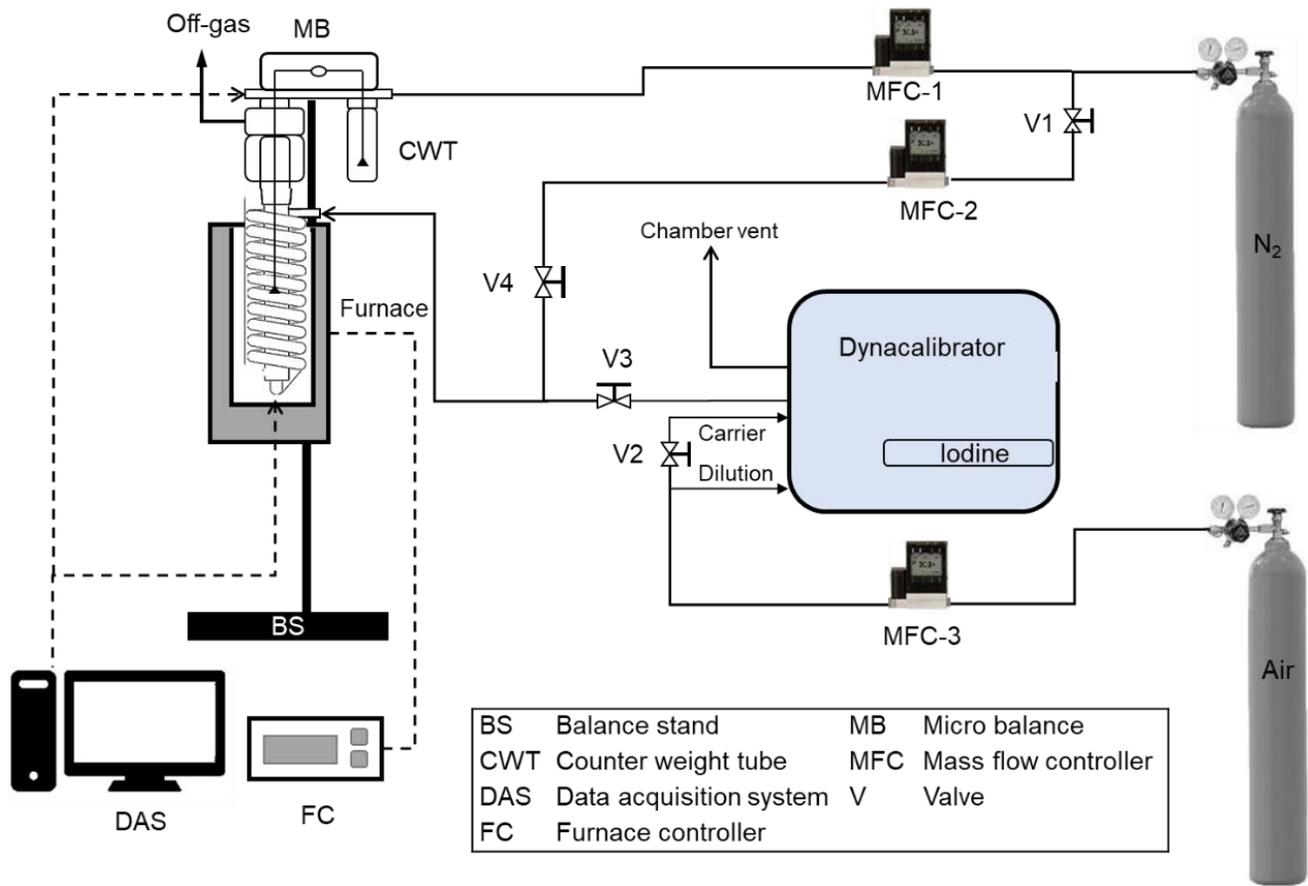
Figure 3-3. Schematic diagram of the continuous-flow I₂ adsorption system.
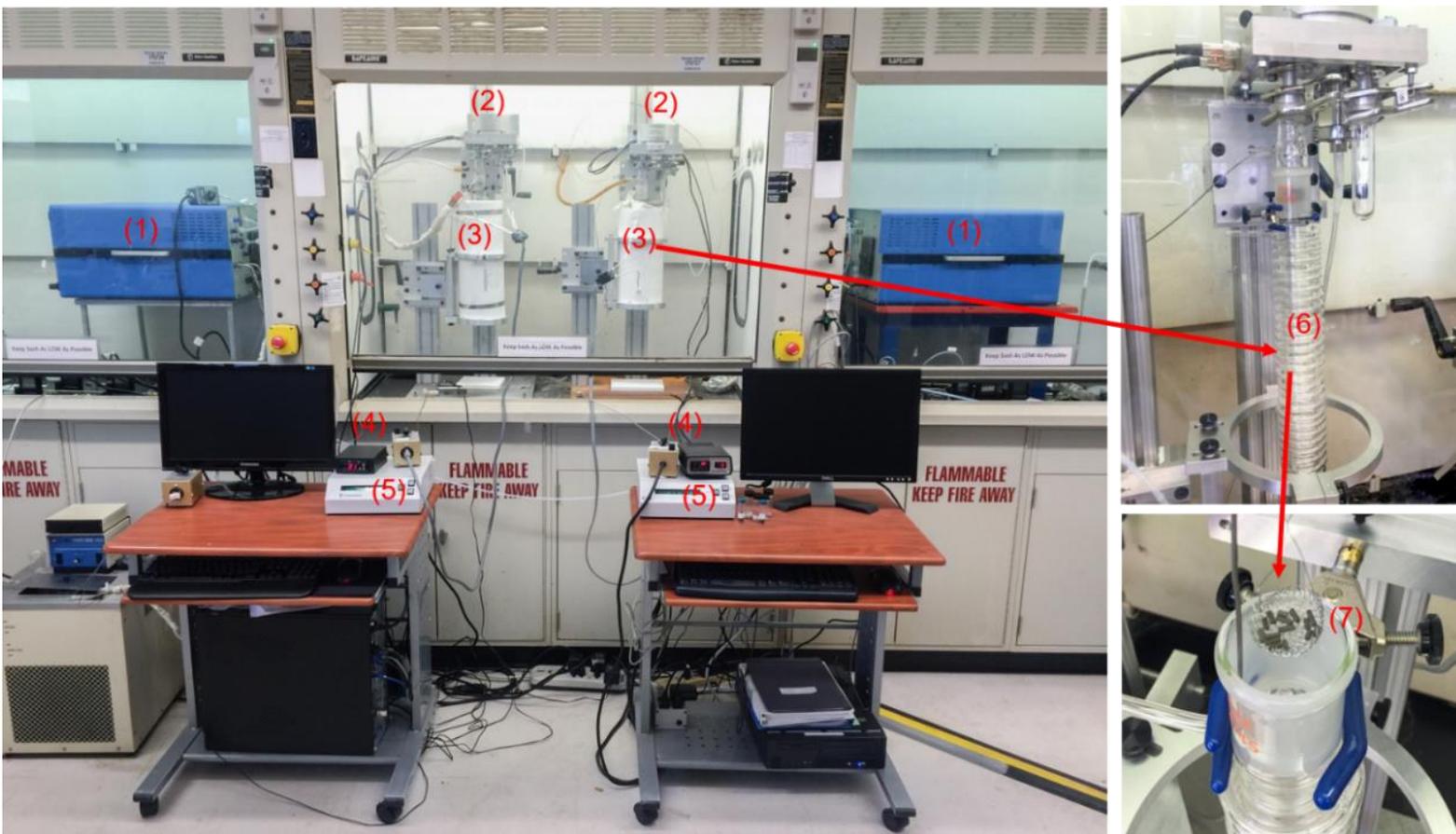
Figure 3-4. Photographs of the iodine adsorption systems. (1). Dynacalibrator; (2). Microbalance; (3). Furnace; (4). Temperature controller; (5). Data collection system; (6). Adsorption column with preheating coil inside the furnace; (7). Stainless steel screen tray with Ag^{0}Z loaded.

Continuous-flow adsorption experiments were conducted at wide ranges of conditions. The gas flow rate studied was between 0.25 to 2 L/min, and the corresponding gas velocity passed through the adsorption column was between 0.55 to 4.4 m/min. About 0.2 g Ag^0Z pellets were carefully loaded not to touch one another. Before I_2 adsorption, the pellets were pre-equilibrated in cylinder dry air (with dew point of -70 °C) at desired experiment conditions. Then I_2 vapor was introduced into the dry air stream and then the total flow rate was adjusted to maintain the same value as before. Desorption experiments subsequently followed by stopping the I_2 vapor from the gas stream. Consequently, the physisorbed I_2 was desorbed.

3.2.3.2. H₂O adsorption

The H_2O adsorption isotherms were obtained with a continuous-flow adsorption system similar to the iodine adsorption system. As shown by the diagram in **Figure 3-5**, The system included a H_2O vapor generation unit which was capable of generating humid gas streams with a dew point ranging from -70 to 20 °C, a heating unit with a working capacity of 25 to 300 °C, an analytical microbalance with a sensitivity of 0.1 μg, and a programmed data acquisition system. A screen tray, as illustrated in **Figure 3-5**, was suspended on the microbalance head and placed inside a glass column (I.D. = 3 cm). Instead of a dynacalibrator, a H_2O bath with a bubbler was used for generating H_2O vapor. The desired H_2O vapor concentration was controlled by manipulating the flow rates of gases and the temperature of the H_2O bath. In addition, the dew point of the carrier gas was monitored by an onsite dew-point meter to ensure constant concentrations of H_2O vapor in the gas flow throughout the experiments. The rest part of the system was the same to the iodine systems.
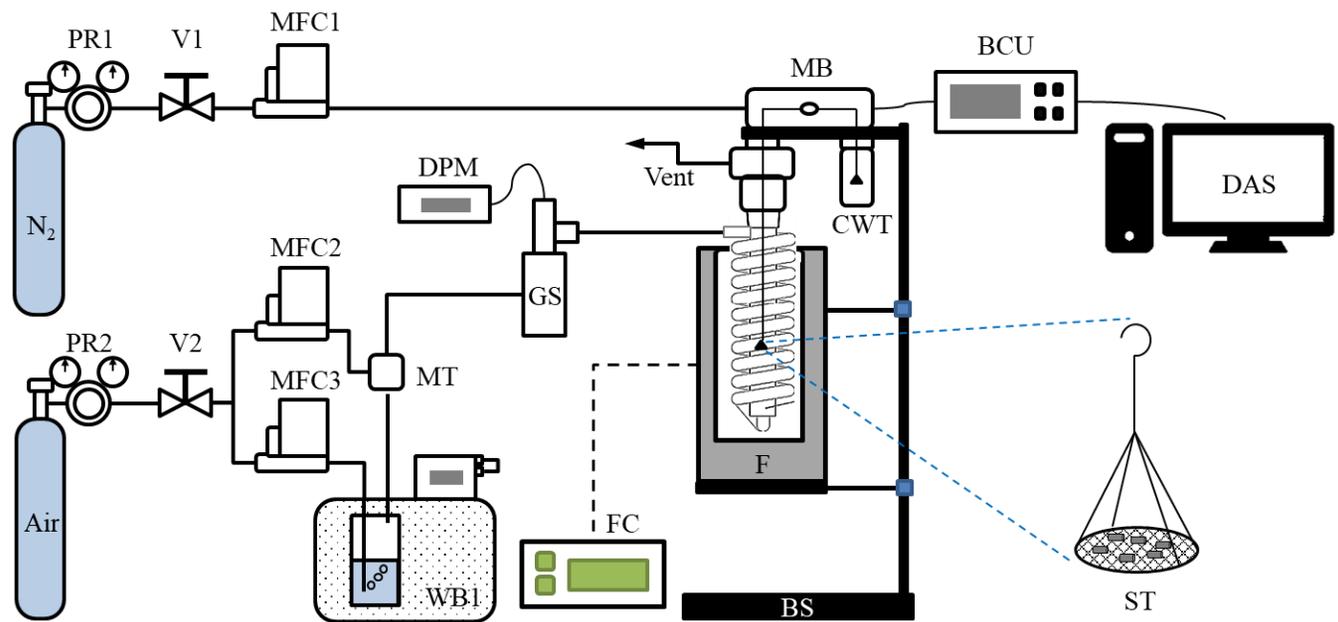
BCU	Balance control unit	GS	Gas sampler	MT	Mixing tube
BS	Balance stand	F	Furnace	PR	Pressure regulator
CWT	Counter weight tube	FC	Furnace controller	ST	Screen tray
DAS	Data acquisition system	MB	Micro balance	V	Valve
DPM	Dew point meter	MFC	Mass flow controller	WB	Water bath

Figure 3-5. Schematic diagram of the continuous flow water adsorption system.

H$_2$O adsorption experiments were performed with a single-layer of Ag^{0}Z (also AgZ) pellets at a wide range of conditions. Before adsorption, about 0.2 g pellets were degased using the ASAP 2020 Physisorption Analyzer under vacuum at 250 $^\circ$C for eight hr to remove the residual moisture in the pellets. When the desired adsorption conditions were established, the dried pellets were carefully loaded onto the screen tray suspended inside the adsorption column.

The adsorption experiments were conducted at 25, 40, 60, 100, 150, and 200 $^\circ$C over dew points from -59 $^\circ$C to 20 $^\circ$C. Kinetic data of H$_2$O adsorption on Ag^{0}Z were obtained with a gas flow rate of 1000 ml/min, while, for equilibrium data, the gas flow rate was set at 500 ml/min.

3.2.3.3. I$_2$ / H$_2$O co-adsorption

I$_2$ - H$_2$O co-adsorption experiments were performed the iodine adsorption system by adding a H$_2$O vapor streamline into the system as shown in **Figure 3-6**. The experimental procedures were similar to those for I$_2$ and H$_2$O adsorption.
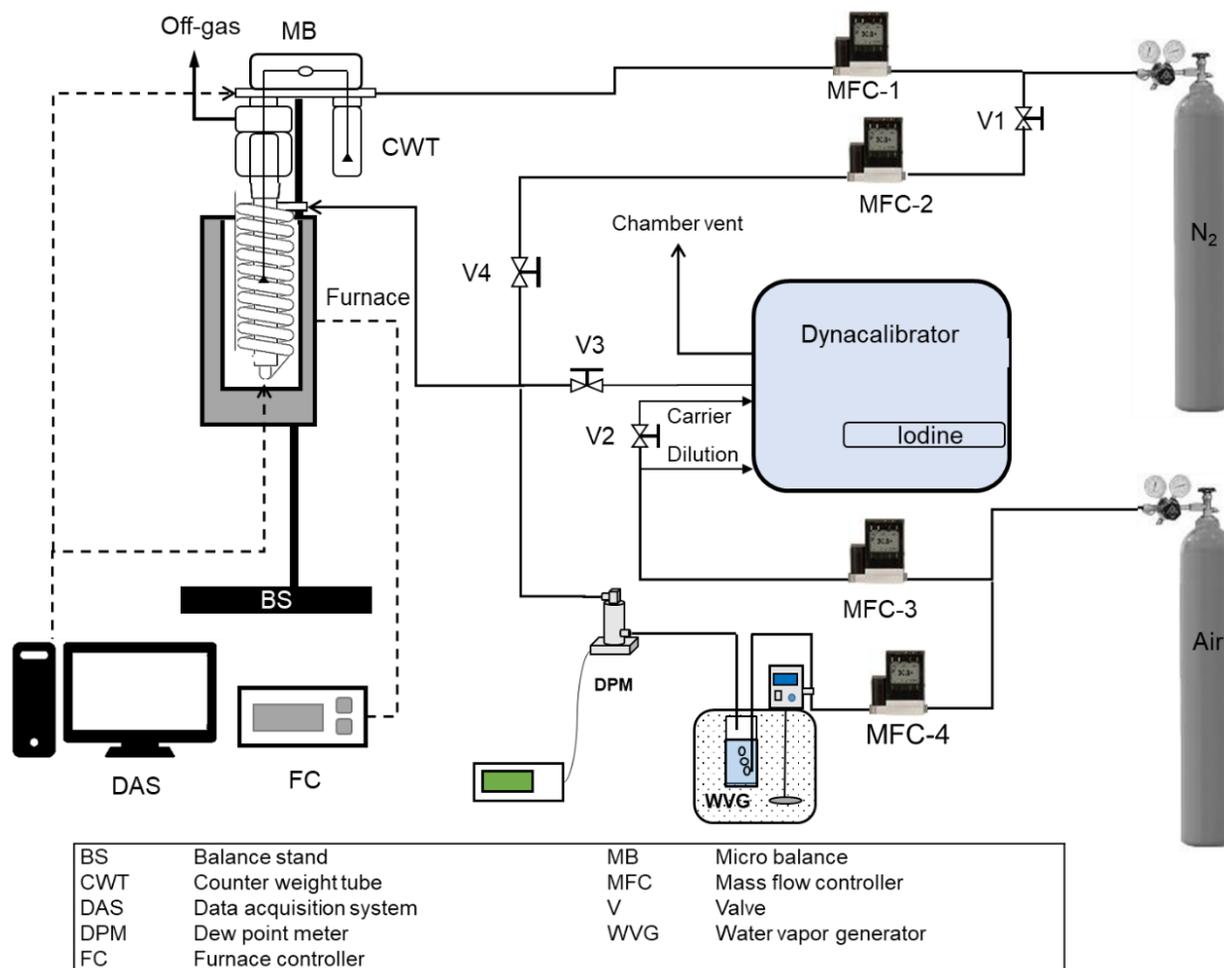
Figure 3-6. The modified adsorption system for I_2 - H_2O co-adsorption.

3.3. Analytical Techniques

ICP-OES

The Ag^0Z samples were analyzed using a Thermo iCAP 650 inductively coupled plasma optical emission spectrometer (ICP-OES) at the ultra-trace preparation laboratory of Research Triangle Institute, NC. The content of silver (Ag), sodium (Na), silicon (Si), aluminum (Al), iron (Fe), calcium (Ca), and potassium (K) were determined. The testing procedures as indicated by the researcher was stated as follows.

The sample preparation was conducted using two methods:

The first preparation method involved the grinding of samples into powder form using a mortar and pestle, a nominal 200mg aliquot of each sample was weighed into an acid-leached extraction tube. Nitric and Unisolve (70% HCl, 30% HF v/v) acids, 0.50 mL and 3.00 Ml, respectively, were added and the samples were placed in a graphite block digestion unit at $1100\,^0C$ for 480 minutes. The samples were then cooled, brought to a final volume of 50mL, capped, and vortex mixed. This method was designed to allow for the analysis of Na, Si, Al, Fe, Ca, and K.

A second preparation method utilized a nominal 50 mg aliquot of each sample in its ground powdered form, which was weighed into an acid-leached extraction tube. A 1.00 mL aliquot of nitric acid was added to each tube and samples were placed in a graphite block digestion unit at $900\,^oC$ for 240 minutes. The samples were then cooled, brought to a final volume of 10mL, capped, and vortex mixed. This method was designed to allow for the analysis of Ag.

Mercury Porosimetry

The porosity and density were determined by mercury porosimetry analysis at Porous Materials, Inc. Ithaca, NY. The test was conducted using 1.62 g of Ag^0Z at pressures ranged from 20.26 PSIA to 60044.21 PSIA, with mercury contact angle of 140 Degree and mercury surface tension of 480 Dynes/cm.

N_2 physisorption

The specific surface areas and pore volumes of Ag^0Z samples were determined by N_2 physisorption measurements with a Micrometrics ASAP 2020 Analyzer. The Brunauer-Emmett-Teller (BET) surface area was determined using the five-point BET method.[118] The micropore surface area, external surface area, and micropore volume were estimated by using the Harkins-Jura (HJ) t-plot model,[119] and the mesopore and macropore volumes were determined by the Barrett-Joyner-Halenda (BJH) desorption curves.[120]

SEM-EDX

Scanning electron microscopy (SEM) (JEOL 5600, JEOL, Dearborn, MA) was performed to observe the changes in the morphology of AgZ crystals upon hydrogen reduction. Images of AgZ and Ag^0Z using secondary electron imaging (SEI) were obtained at high magnifications, and backscattered electron images were captured to identify the silver particles formed on the mordenite crystal surfaces after reduction. In addition, energy dispersive X-ray spectroscopy (EDX) analysis was also performed to obtain qualitative information of elemental compositions of AgZ and Ag^0Z as well as element mapping.

XRD

Powder X-ray diffraction (XRD) patterns of AgZ and Ag^0Z were obtained with a Bruker D8 Powder Diffractometer equipped with Cu Kα radiation (λ =1.54056 Å) at 40 kV and 25 mA. The patterns were recorded with the 2θ range from 15° to 60°.

Raman Spectroscopy

Raman spectra of the mordenite samples were obtained with a confocal Raman microscope (Renishaw, InVia) using a 785 nm continuous wave (CW) diode laser. The system combined the Raman spectrometer and a Leica DM2700P microscope. Spectra were acquired between 1000 and 3500 cm^{-1}.

XAFS

X-ray absorption fine structure (XAFS) investigations were performed at beamline 10ID-B of the Advanced Photon Source at Argonne National Laboratory.[121] Ag^0Z samples were sent to ANL, and the tests and analyses were done by Dr. Carter Abney. The results were published in an article co-authoring with Yue Nan and Dr. Lawrence Tavlarides.[122] The following procedures for the XAFS analyses were cited from the published article.

XAFS is an element-specific technique and is capable of directly investigating both oxidation state and coordination environment of the absorbing element, including identification of adjacent atoms from differences in backscattering amplitude as a function of atomic number.[123]

Spectra were collected at the silver K-edge (25514 eV) in transmission mode with a silver foil collected simultaneously and used as the reference for energy calibration as well as for data analysis. The x-ray white beam was monochromatized by a Si(111) monochromator with higher-order harmonics removed through the use of a Pt harmonic

rejection mirror, suitable for energies above 18 keV. The incident beam intensity (I_0), transmitted beam intensity (I_t) and reference (I_{ref}) were all measured by 20 cm ionization chambers with gas compositions of 95% Ar and 5% N_2. All spectra were collected at room temperature. Samples were centered on the beam and adjusted to find the most homogeneous location for data collection. Due to the high flux and configuration of the beamline, the x-ray energy was varied at a constant rate across the absorption edge; neither step size nor dwell time changed as a function of energy. Ten scans were collected for each sample.

Data were processed and analyzed using the Athena and Artemis programs of the IFEFFIT package based on FEFF 6.[124-125] Upon importing, data were rebinned with grids of 10 eV, 0.5 eV, and 0.05 Å^{-1} for the pre-edge region, XANES region, and EXAFS region, respectively. Reference foil data were aligned to the first zero-crossing of the second derivative of the normalized $\mu(E)$ data, which was subsequently calibrated to the literature E_0 for the silver K-edge. Spectra were averaged in $\mu(E)$ prior to normalization. The background was removed and the data were assigned an Rbkg value of 1.0 before normalizing to obtain a unit edge step.

All data were initially fit with k-weighting of 1, 2, and 3, then finalized with k^3-weighting in R-space. A fit of the Ag^0 foil standard was used to determine S_0^2 for reduced and regenerated AgZ, while a fit of an Ag_2O standard afforded the same parameter for I_2-contacted and recycled AgZ. Structure models used to fit these data sets were obtained from crystal structures of Ag^0 foil,[126] Ag_2O,[127] γ/β-AgI,[128-129] and α-AgI.[130] Structural parameters that were determined by the fits include the degeneracy of the scattering path (N_{degen}), the change in R_{eff} (ΔR_i), the relative mean square displacement of the scattering

element (σ^2_i), and the energy shift of the photoelectron, (ΔE_0). For each fit, the number of independent points was not permitted to exceed 2/3 the number of variables, in keeping with the Nyquist criterion.[131]

3.4. Modeling

3.4.1. Kinetic models

3.4.1.1.   Shrinking core model

The Shrinking Core (SC) model has been widely used to describe gas-solid adsorption systems.[132-133] In a previous study,[115] the SC model described adsorption of H_2O on molecular sieves 3A by diffusion through the external gas film and the saturated adsorbent shell. Also, Jubin[70] used this model for predicting the adsorption of methyl iodide on Ag^0Z which involved both mass transfer and reaction processes.

The adsorption process described by the SC model includes: a) diffusion through the external gas film, b) diffusion through the reacted shell, and c) reaction on the surface of the unreacted core. As adsorption proceeds, demonstrated by **Figure 3-7**, the diameter of the unreacted core shrinks. In addition, this model assumes the reaction rate is relatively fast so that there was no significant sorbate concentration gradient near the reacting surface.
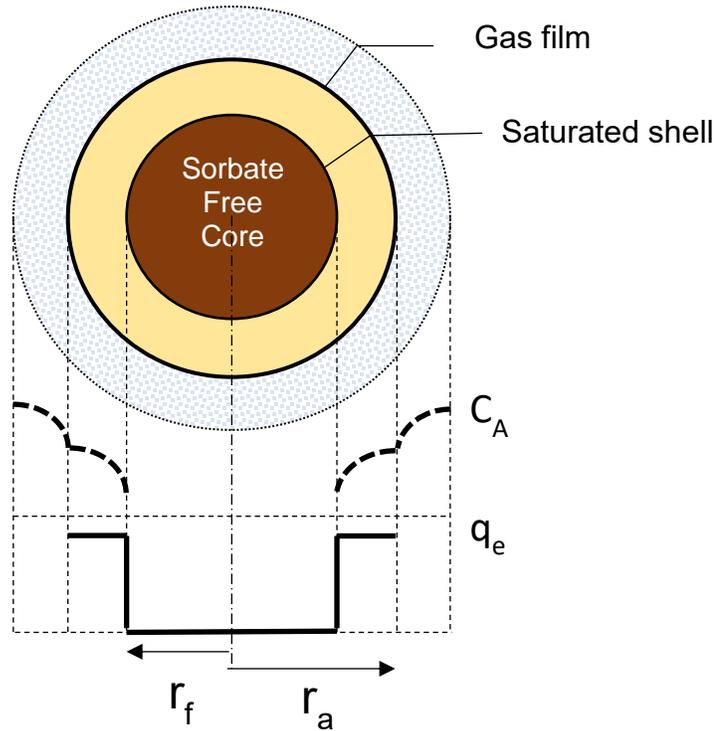
Figure 3-7. Shrinking core process during adsorption on a solid particle.

The general form of SC model can be expressed in terms of adsorption time, t, by the following Eq. (1):

$$t = \frac{q}{q_e}\tau_1 + \left(1 + 2\left(1 - \frac{q}{q_e}\right) - 3\left(1 - \frac{q}{q_e}\right)^{\frac{2}{3}}\right)\tau_2 + \left(1 - \left(1 - \frac{q}{q_e}\right)^{\frac{1}{3}}\right)\tau_3 \quad (1)$$

where q_e and q are the equilibrium and average transient sorbate concentration (g/g) in the adsorbent, respectively, and τ_1, τ_2 and τ_3 are the time required to reach equilibrium if the adsorption is controlled by the external gas film mass transfer, pore diffusion and gas-solid reaction, respectively, given by:

$$\tau_1 = \frac{R_a q_e \rho_p}{3 b k_f C_b} \quad (2)$$

$$\tau_2 = \frac{R_a^2 q_e \rho_p}{6 b D_p C_b} \quad (3)$$

$$\tau_3 = \frac{R_a q_e \rho_p}{b k_s C_b} \quad (4)$$

where r_a and ρ_p denote radius (cm) and density (g/cm^3) of the pellets, respectively, C_b is the bulk gas-phase concentration (g/cm^3), k_g is the gas film mass transfer coefficient, D_p is the pore diffusivity which in fact represent a lumped diffusivity for the overall diffusion process, k_s is the reaction rate constant assuming the reaction is a simple first-order reaction, and b is stoichiometric coefficient of solid reactant in the gas-solid reaction:

$$aA(g) + bB(s) \rightarrow cC(s) + dD(g) \quad (5)$$

To determine the dominating rate controlling mechanisms, the obtained kinetic data were fitted by the SC model with different combinations of controlling terms: mass transfer (external mass transfer and diffusion) controlling using Eq. (6), reaction controlling using Eq. (7), and all three controlling terms using Eq. (1).

$$t = \frac{q}{q_e}\tau_1 + \left(1 + 2\left(1 - \frac{q}{q_e}\right) - 3\left(1 - \frac{q}{q_e}\right)^{2/3}\right)\tau_2 \quad (6)$$

$$t = \left(1 - \left(1 - \frac{q}{q_e}\right)^{1/3}\right)\tau_3 \quad (7)$$

3.4.1.2. Pore diffusion models

The bidisperse model developed by Ruckenstein et al.[134] describes the adsorption process on a spherical microporous particle consisting of small spherical microporous particles, where both macropore and micropore resistances are significant. It assumes that the adsorption occurs on both macropore walls and inside the micropore after the adsorbate diffuses into the macropore and micropore. The model was solved based on the assumption that the isotherm of the adsorption in the pores is linear. Equations describing the diffusion of gas into the macropore and micropore are expressed as Eq. (8) and (9): [134]

$$\frac{D_a \varepsilon_a}{r_a^2} \frac{\partial}{\partial r_a} [r_a^2 \frac{\partial C_a}{\partial r_a}] = \varepsilon_a \frac{\partial C_a}{\partial t} + S_a \frac{\partial C_{sa}}{\partial t} + 4\pi n R_i^2 \varepsilon_i D_i (\frac{\partial C_i}{\partial r_i})_{r_i = R_i} \quad (8)$$

$$\frac{D_i \varepsilon_i}{r_i^2} \frac{\partial}{\partial r_i} [r_i^2 \frac{\partial C_i}{\partial r_i}] = \varepsilon_i \frac{\partial C_i}{\partial t} + S_i \frac{\partial C_{si}}{\partial t} \quad (9)$$

where the subscript a and i represent macropore and micropore, respectively, the subscript s means the adsorbed adsorbate, C is the fluid phase sorbate concentration, r is the distance from the sphere center, R is the radius of the sphere (macrosphere or microspheres), S is the surface area, ε is the porosity, D is the diffusivity, n is the number of microspheres per unit macrosphere volume.

The initial conditions, boundary conditions, and the solution to Eqs. (8) and (9) were reported by Ruckenstein et al., and a simplified solution was also provided as [134]

$$\frac{q}{q_e} = \frac{[1 - \frac{6}{\pi^2} \sum_{n=1}^{\infty} \frac{1}{n^2} \exp(-\frac{n^2 \pi^2 D_a ' t}{R_a^2})] + \frac{\beta}{3\alpha} [1 - \frac{6}{\pi^2} \sum_{n=1}^{\infty} \frac{1}{n^2} \exp(-\frac{n^2 \pi^2 D_i ' t}{R_i^2})]}{1 + \frac{\beta}{3\alpha}} \quad (10)$$

33

where q and q_e are the transient and equilibrium uptake of adsorbate in the adsorbent, respectively, and other parameters are given as

$$D_a' = \frac{D_a}{1 + \frac{H_a S_a}{\varepsilon_a}} \qquad (11)$$

$$D_i' = \frac{D_i}{1 + \frac{H_i S_i}{\varepsilon_i}} \qquad (12)$$

$$\alpha = \frac{D_i' R_a^2}{D_a' R_i^2} \qquad (13)$$

$$\beta = \frac{3(1 - \varepsilon_a)\varepsilon_i D_i' R_a^2}{\varepsilon_a D_a' R_i^2} \qquad (14)$$

The first term of the numerator on the right-hand side of Eq. (10) represents the macropore diffusion process and the second term describes the micropore diffusion. According to Karger and Ruthven,[135] when the adsorbate diffuses into the micropore much more rapidly than into the macropore, the Eq. (10) can be simplified to a macropore diffusion model,

$$\frac{q}{q_e} = 1 - \frac{6}{\pi^2} \sum_{n=1}^{\infty} \frac{1}{n^2} \exp\left(-\frac{n^2 \pi^2 D_a t}{R_a^2 (1 + K(1 - \varepsilon_p)/\varepsilon_p)}\right) \qquad (15)$$

where $K = q_e \rho_p / C_b$ for linear equilibrium isotherm, ε_p is the porosity of pellet, ρ_p is the density of pellet, and C_b is the adsorbate bulk concentration. Conversely, when the micropore diffusion is controlling process the fractional uptake can be expressed as: [135]

$$\frac{q}{q_e} = 1 - \frac{6}{\pi^2} \sum_{n=1}^{\infty} \frac{1}{n^2} \exp(-\frac{n^2 \pi^2 D_i t}{R_i^2}) \quad (16)$$

3.4.1.3.   Linear driving force model

The linear driving force (LDF) model proposed by Gleuckauf and Coates[136] has been frequently and successfully used for analysis of gas adsorption kinetics because of its simplicity and physical consistency. The model defines the average sorbate uptake rate as the product of the amount required to reach equilibrium and the mass transfer coefficient, as given by Eq. (17):

$$\frac{dq}{dt} = k_{LDF} \left(q_e - q \right) \qquad (17)$$

where k_{LDF} is the LDF mass transfer coefficient. The value of k_{LDF} can be estimated from the plot of $ln((q_e\text{-}q)/q_e)$ vs t when integrating Eq. (17) to Eq. (18),

$$\ln\left(\frac{q_e - q}{q_e} \right) = -k_{LDF} t \qquad (18)$$

For isothermal adsorption, k_{LDF} can be expressed by the following equation:[132]

$$\frac{1}{k_{LDF}} = \frac{R_a}{3k_f} \frac{q_e \rho_p}{C_b} + \frac{R_a^2}{15\varepsilon_p D_a} \frac{q_e \rho_p}{C_b} + \frac{R_i^2}{15 D_i} \qquad (19)$$

where R_a is the radius of pellet, and R_i is the radius of microcrystals, k_f is the gas film mass transfer coefficient, D_i and D_a are the micropore and macropore diffusivity, respectively. The three terms, from left to right, on the right-hand side of Eq. (19) represent external gas film resistance, macropore diffusion resistance, and micropore diffusion resistance, respectively.

3.4.2. Equilibrium models

It is commonly known that gas adsorption on zeolites including mordenites is a complicated process due to the surface heterogeneity of the materials, which leads to a variation of adsorption thermodynamics on different adsorption sites. The sites of higher energy are bonded first with the adsorbate, then sites of lower energy are progressively bonded as the gas pressure is increased. Therefore, in this study, equilibrium models including parameters to account for surface heterogeneity were employed to describe the adsorption of H_2O on Ag^0Z and AgZ. The commonly used models such as Sips,[137] Toth,[138] and Unilan[139-140] have a parameter believed to reflect the heterogeneity of the adsorbent system. However, they fail to provide an exact physical description of the heterogeneous property. This property can be obtained by using the Heterogeneous Langmuir model and the GSTA model as they have a parameter regarded as the number of energetically distinguished adsorption sites.

3.4.2.1. Heterogeneous Langmuir model

The Heterogeneous Langmuir adsorption model is an extension of the Langmuir equation. It is assumed that the heterogeneous surface of the sorbent is comprised of a number of discrete homogeneous adsorption sites, and each type of homogeneous site has its own equilibrium constant and adsorption capacity that can be described by the Langmuir equation.[141-143] It can also be interpreted that the adsorption on the heterogeneous surface is a multiple adsorption process with heterogeneous energetic interactions of the adsorbate with the adsorption sites, and the adsorption on each individual energetic site is a Langmuir adsorption process. Using the Heterogeneous Langmuir model, the energy of adsorption

associated to each of the energetic interactions can be obtained. This model can be expressed by Eq. (20):

$$q = \sum_{n=1}^{m} \frac{q_{\text{max}n} K_n p}{1 + K_n p} \qquad (20)$$

where q is the adsorbed phase concentration, $q_{\text{max},n}$ is the maximum adsorption capacity of the nth adsorption site, m is the number of different types of adsorption sites, p is gas phase partial pressure, and K_n is the equilibrium constant associated with the adsorption on the nth type of adsorption site.

3.4.2.2. GSTA Model

The GSTA model proposed by Liano-Restrepo and Masquera[144] can be regarded as a special case of the Heterogeneous Langmuir model[48]. Similar to the Heterogeneous Langmuir model, it is assumed that there are different adsorption sites on the adsorbent surface and the uptake on each adsorption site is a Langmuir adsorption process. However, the GSTA model assumes that all adsorption sites have the same capacity (q_{max}/m). The benefit of this assumption is that it reduces the number of parameters to be determined, and consequently simplifies correlating the model with the experimental data, especially for systems of high heterogeneity (a large value of m). Ladshaw et al.[145] and Lin et al.[114] have demonstrated the capabilities of the GSTA model in describing different gas-solid adsorption systems such as CO, H_2S and C_3H_8 on H-mordenite, CH_4, CO, CO_2 and H_2 on activated carbon, and H_2O vapor on molecular sieve 3A. The GSTA model is expressed by Eq. (21):

$$q = \frac{q_{\max}}{m} \frac{\sum\limits_{n=1}^{m} nK_n^o \left(p/P^o\right)^n}{1 + \sum\limits_{n=1}^{m} K_n^o \left(p/P^o\right)^n} \tag{21}$$

where K_n^o is the unitless GSTA equilibrium constant associated with the nth site, P^o is the standard state pressure of 100 kPa, and the other symbols in the equation represent same parameters as described above in the Heterogeneous Langmuir model. Note that in the GSTA isotherm, $q_{\max}$ would be equal to the sum of the $q_{\max,n}$ parameters of the Heterogeneous Langmuir model.

The thermodynamic parameters, enthalpies (ΔH_n) and entropies (ΔS_n), associated with the adsorption isotherms were determined by the Van't Hoff equation (Eq. 22) after the equilibrium constants (K_n or K_n^o) for each adsorption site at various temperatures were obtained. In theory, different ΔH_n and ΔS_n should be obtained for each different adsorption site to represent its distinct energy characteristics:

$$\ln K_n = -\frac{\Delta H_n}{RT} + \frac{\Delta S_n}{R} \tag{22}$$

The analysis of the data with the models discussed above was performed with a code developed in MATLAB (R2015a), which included optimization processes to obtain the optimal equilibrium parameters. The non-linear least-squares method was used to minimize the errors between the model and experimental data. To determine the number of adsorption sites (m) needed to describe the system, the objective function described by Ladshaw et al was used.[145] This function minimizes the value of m, preventing over-description of the system.

Chapter 4. I$_2$ Adsorption on Ag^{0}Z[‡]

4.1. Introduction

In this chapter, results of I$_2$ adsorption on Ag^{0}Z were analyzed and discussed. The optimal reduction conditions for Ag^{0}Z was first determined. Through different chemical/physical analyses of the AgZ and Ag^{0}Z, mechanism of the Ag reduction process was determined and was in agreement with previous studies. The Ag particles formed on the mordenite crystal surface could be clearly observed by SEM imaging. The I$_2$ adsorption mechanism was also determined through chemical analyses of the I$_2$ loaded Ag^{0}Z. The adsorption of I$_2$ mainly accorded through the reaction with Ag forming AgI. In addition, adsorption of I$_2$ on Ag^{0}Z pellets was a shrinking core process.

The adsorption kinetics was studied through experiments on single-layer Ag^{0}Z pellets in continuous-flow adsorption systems of high precision at temperatures of $100 - 250$ ^{o}C and I$_2$ concentrations of $9 - 52$ ppmv. Equilibrium and kinetic data of adsorption were obtained for capacity evaluation and kinetic modeling. Desorption data were collected to distinguish the contribution of physisorption and chemisorption. The impact of temperature on the equilibrium I$_2$ loading was discussed. Kinetic data were analyzed by the Shrinking Core model and the model parameters associated with the mass transfer and reaction process

---

[‡] Permission granted by American Chemical Society and John Wiley and Sons to use the text of published articles[88,122] in this chapter.

88. Nan, Y.; Tavlarides, L. L.; DePaoli, D. W., Adsorption of iodine on hydrogen-reduced silver-exchanged mordenite: Experiments and modeling. AIChE Journal 2017 63 (3), 1024–1035.

122. Abney, C. W.; Nan, Y.; Tavlarides, L. L., X-ray Absorption Spectroscopy Investigation of Iodine Capture by Silver-Exchanged Mordenite. Industrial & Engineering Chemistry Research 2017, 56 (16), 4837-4846.

were determined. In addition, the primary controlling mechanisms were determined based on the modeling results.

4.2. Optimal Reduction Conditions and Properties of Ag^0Z

The I_2 and H_2O loading capacity of Ag^0Z reduced at different conditions were determined by batch experiments for comparison. **Figure 4-1** shows the H_2O and I_2 uptake of one experiment as an example. Ag^0Z samples reduced at 170, 230, 300 and 400 °C for 24 hours were first loaded with about 4 wt. % H_2O, and subsequently loaded with I_2. The samples achieved similar weight gain due to the adsorption of H_2O, but the sample reduced at 400 °C had the highest I_2 loading capacity among the four samples. Similar experiments were performed to determine and compare the capacities of all samples. It was found that all the Ag^0Z samples reduced at different conditions had identical H_2O adsorption capacity.
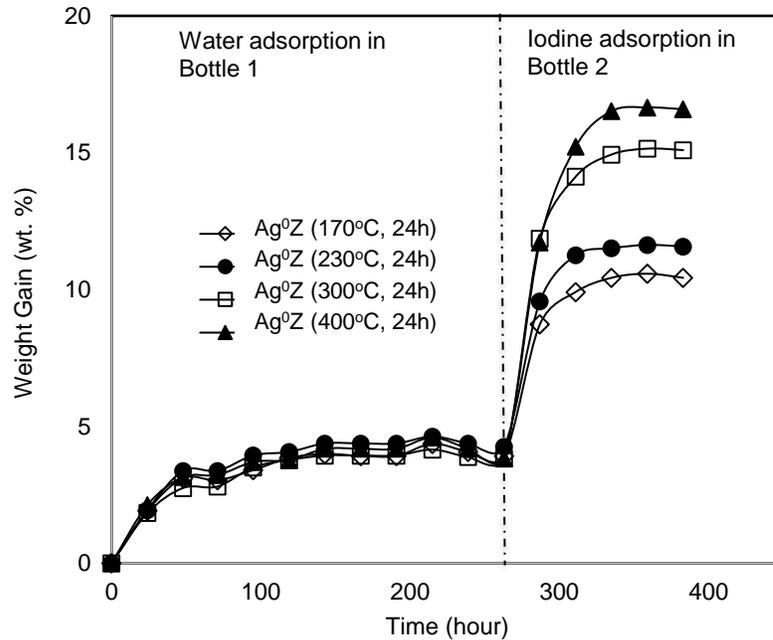
Figure 4-1. Adsorption of H_2O and I_2 on Ag^0Z reduced at 170, 230, 300 and 400 °C for 24 hours.

The effects of reduction temperature and time on the I_2 adsorption capacity are shown in **Figure 4-2**. As shown in the plots, given the reduction time of 24 hours, the I_2 loading capacity of Ag^0Z increased as reduction temperature increased from 170 to 400 °C, which indicated that high temperature favors the conversion of Ag^+ to Ag^0 in hydrogen. Further raising the temperature to 500 °C did not increase the capacity. The same tendencies were observed at reduction times of 120 and 336 hours that the increase of I_2 loading capacity also leveled off at 400 °C. It is also noted that a longer reduction time is needed at low reduction temperatures to achieve the maximum I_2 capacity, which is due to the low transformation rate of Ag^+ to Ag^0 rate at low temperatures. The curves indicate that there is no further increase in I_2 loading capacity beyond the reduction conditions of 400 °C and 24 hours, which indicated that, at these optimal conditions, the AgZ was fully reduced. Therefore, this set of conditions is the optimal reduction conditions for Ag^0Z used in this study and is supported by similar studies in the literature.[103, 146]

Previous studies[147-148] also reported that high temperatures up to 900 °C were required to reduce the Ag in AgZ crystals. The AgZ used in these studies was prepared by ion exchange of commercial NaZ (Si/Al: 6.5:1) in $AgNO_3$ solution, which had different properties to the commercial AgZ pellets (Si/Al: 5:1) used in this study. It is noted that the physisorbed I_2 on the samples in the batch experiments at room temperature and saturated I_2 vapor pressure, should be more than that in the later continuous-flow experiments at 100 – 250 °C and 9 – 52 ppmv under which conditions chemisorption occurs mostly. Therefore, the equilibrium I_2 loading of the batch experiments is not comparable with that of the continuous-flow experiments.
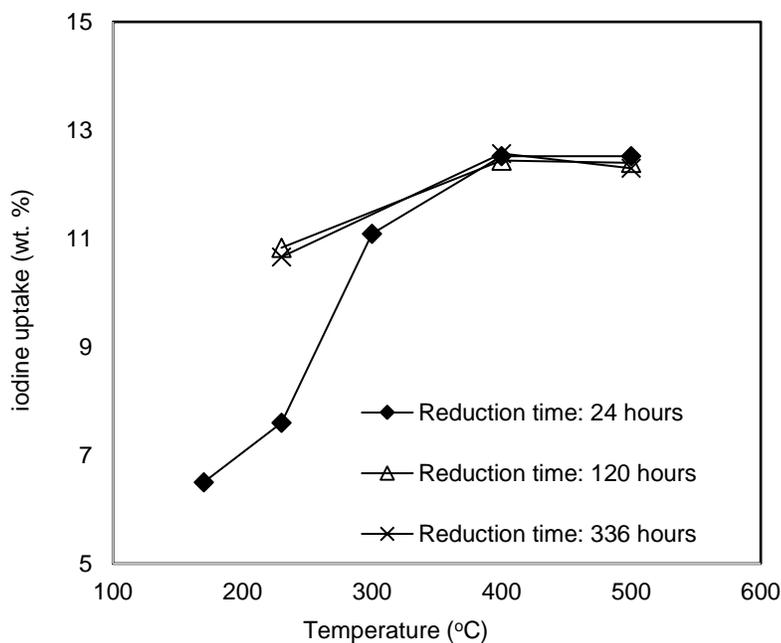
Figure 4-2. Effect of reduction conditions on the I_2 adsorption capacity of Ag^0Z.

The backscattered electron images shown in **Figure 4-3** demonstrate the differences between the unreduced AgZ and Ag^0Z reduced at the optimal reduction conditions. The unreduced AgZ crystals show a uniformed elemental distribution, while small particles (in white color) were observed on the surface of Ag^0Z crystals. The particles distributed all over the surface of the Ag^0Z crystals and their size ranged from 0.1 to 1.17 μm. The element mapping of the Ag^0Z shown in **Figure 4-4** indicated that these particles are reduced Ag particles. As highlighted in the secondary electron and Ag mapping images, upon reduction Ag aggregated into large particles on the surface of the mordenite crystals. Due to the low resolution of the element mapping images, only large Ag particles (~1 μm) can be observed. The other elements namely, Si, Al, and O were distributed evenly in Ag^0Z.
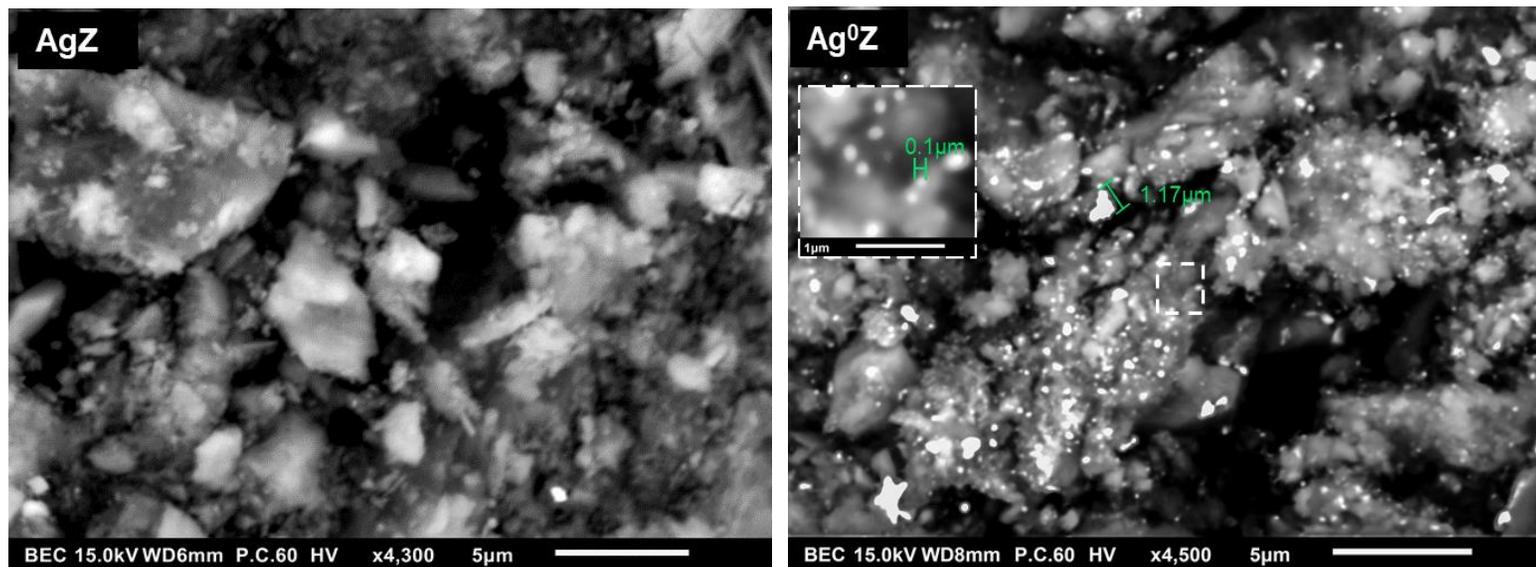
Figure 4-3. SEM (backscattered election composition) images of AgZ and Ag^{0}Z
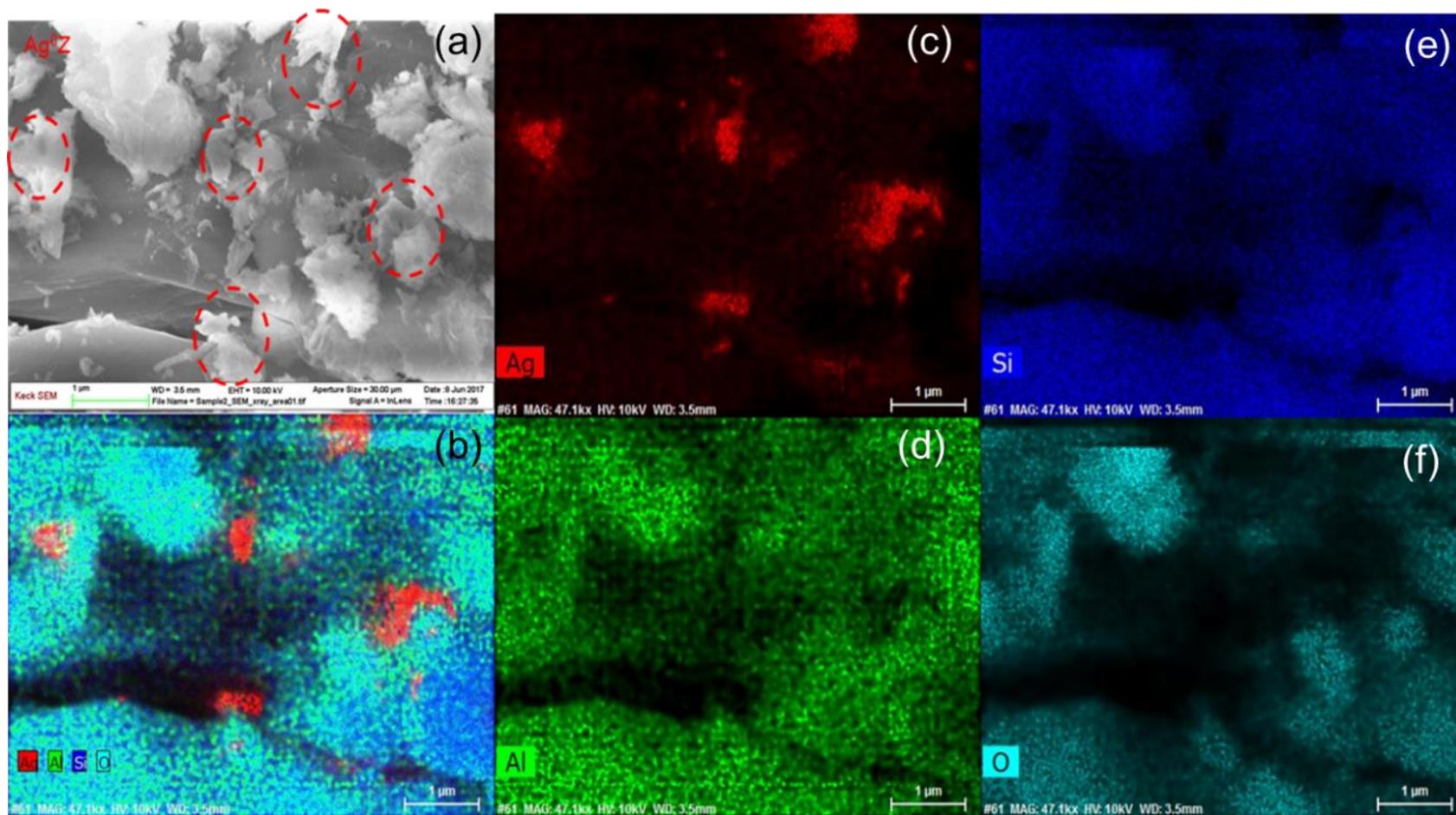
Figure 4-4. Element mapping of Ag⁰Z. a) Secondary electron imaging, b) overlapped mapping of Ag, Al, Si and O, c) mapping of Ag, d) mapping of Al, e) mapping of Si, f) mapping of O.

The formation of the Ag particles is also supported by the XRD patterns shown in **Figure 4-5**. The pattern of the Ag^0Z showed strong peaks for metallic Ag crystals after reduction, while no Ag crystal peaks were observed in the AgZ pattern. This agreed with the fact that the Ag in AgZ was inside the mordenite structure in the form of Ag^+. The peaks for mordenite crystals remained at the same position indicating that there were no changes to the crystal structures of the mordenite when treating in H_2 at 400 °C. As reported previously,[103] silver nanoparticles greater than 3 nm were formed at a reduction temperature of 400 – 500 K (127-227 °C) and the size of the nanoparticles increases with reduction temperature. Since a higher reduction temperature (400 °C) was used in this study, the silver nanoparticles formed on the crystal surface should be larger than that reported in the previous study.

The analyses of the samples with XAFS further confirms the conclusions above. XAFS spectra are artificially separated into two regions for the sake of discussion and analysis. The x-ray absorption near edge spectrum (XANES) includes the region of the XAFS spectrum starting before absorption edge and continuing to 50-100 eV beyond; it displays sensitivity to metal oxidation state and the geometry of coordinating atoms due to selection rules dictating the probability of x-ray absorption. Inspection of the XANES region is particularly enlightening due to the distinctly different oxidation states expected as the AgZ proceeds from the initial form (Ag^{+1}) to reduced Ag^0.
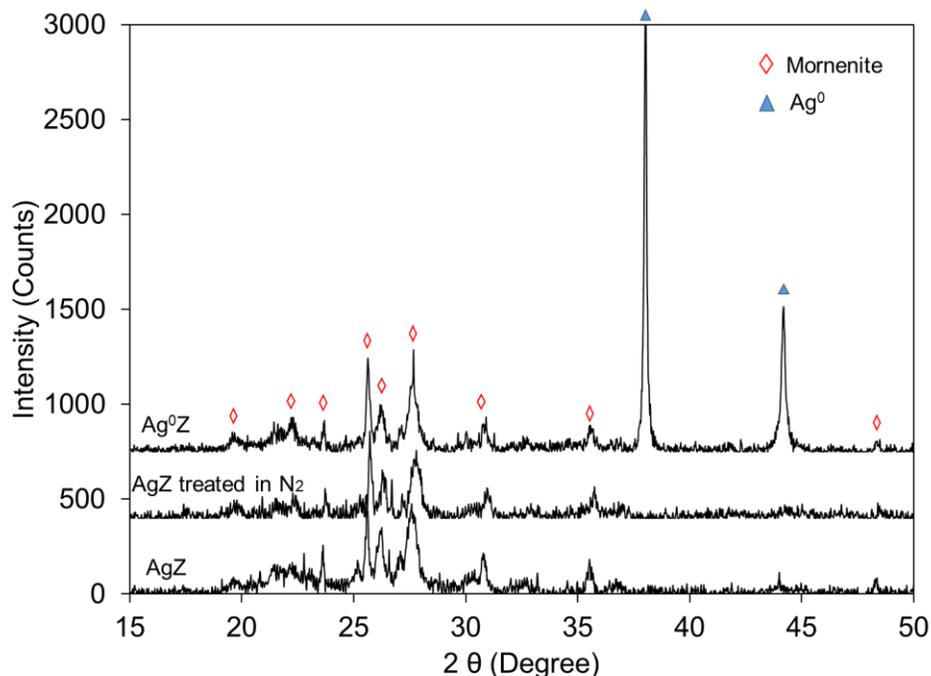
Figure 4-5. XRD patterns of AgZ and Ag^{0}Z

As should in **Figure 4-6**, samples with a +1 oxidation state are the Ag$_2$O, unreduced AgZ and I$_2$-loaded Ag^{0}Z (I$_2$-loaded sample will be discussed in the next section). Samples where silver possesses an oxidation state of 0 include Ag^0 foil and Ag^{0}Z, as well as the. The XANES spectra for Ag^0 foil and Ag^{0}Z possess numerous common features, such as an absorption edge at 25518 eV, a white line at 25530 eV, and local maxima/minima occurring at 25530, 25542, 25554, 25565, 25589, 25602, and 25630 eV. A greater intensity of the features in the bulk Ag^0 foil can be observed compared with Ag^{0}Z, which should attribute to the small Ag^0 particle size in Ag^{0}Z.

The spectra are in good agreement with the collective body of literature regarding the capture of I$_2$ by AgZ. As-synthesized AgZ is fully reduced to an Ag^0 state upon contact with H$_2$ at 400 °C for 24 hrs. A conservative estimate of the sensitivity of the XANES

region to differing oxidation states is approximately 5%, suggesting that at least 95% of the Ag was reduced to Ag^0 upon regeneration.
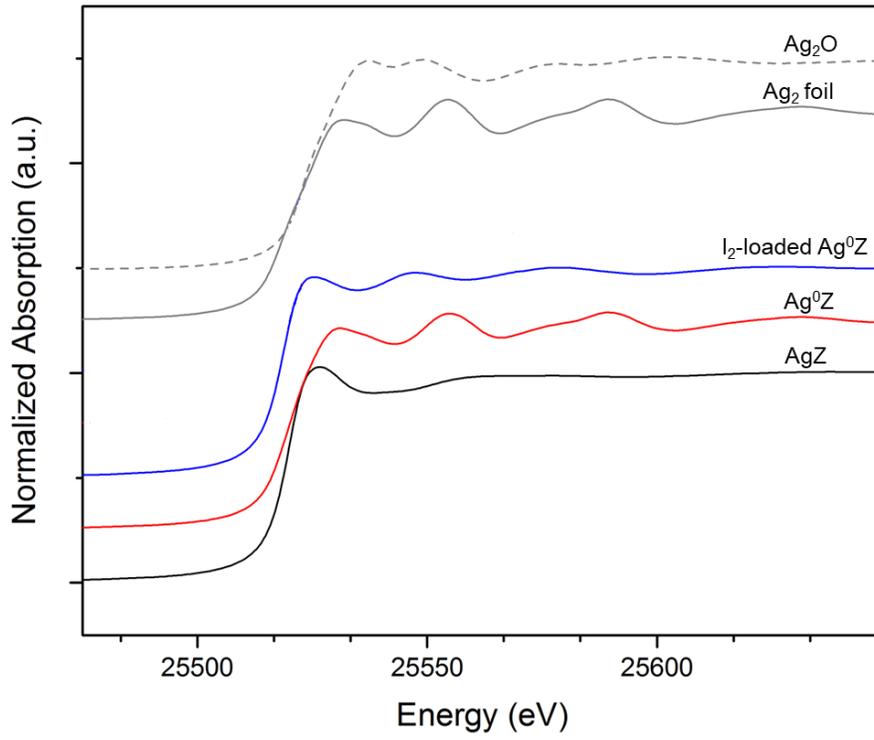
Figure 4-6. XANES data for AgZ samples.

4.3. Mechanism of I_2 Adsorption on Ag^0Z Pellets

Chapman and co-workers[149] have reported the adsorption of I_2 on Ag^0Z through nanoscale AgI formation. The study showed that I_2 was adsorbed by chemical reaction with reduced Ag nanoparticles. To determine the mechanism of I_2 adsorption on the Ag^0Z used in this study and confirm conclusions in the Chapman et al. study, chemical analyses were performed.

An entirely different XANE spectrum of Ag was observed when Ag^0Z was fully loaded with I_2 as shown in **Figure 4-6**. The spectra shift indicated that the oxidation state of Ag changed from 0 to +1, which implied that the Ag was in the form of AgI. XRD pattern was obtained for the I_2 loaded Ag^0Z. As shown in **Figure 4-7**, sharp peaks for AgI crystals were presented in the pattern of I_2-loaded samples. The disappearance of the Ag^0 peaks indicated that Ag particles were converted entirely to AgI. Therefore, the adsorption of I_2 on Ag^0Z is a chemical reaction process of I_2 with Ag forming AgI.
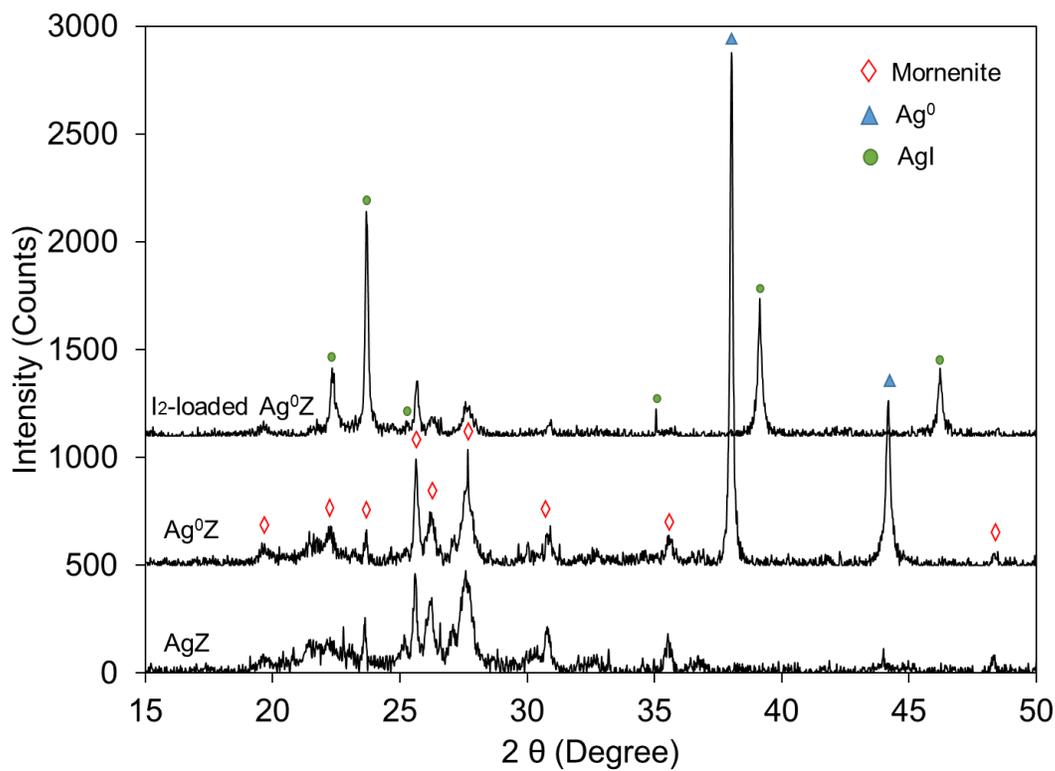
Figure 4-7.XRD patterns of AgZ, Ag^0Z and I_2-loaded Ag^0Z.

One other question worth to address for a better understanding of the adsorption process is how I_2 adsorption proceeds in Ag^0Z pellets, in other words, adsorption kinetics. Since the adsorption of I_2 is a chemical reaction process of I_2 with Ag particles, the process could be controlled by the reaction rate of I_2 with the Ag particles. The overall rate can be controlled by the surface reaction rate of I_2 with Ag, as well as diffusion rate of I_2 into the Ag particles-I_2 must diffuse through the reacted AgI layer to reach Ag inside the particle. Also, since the Ag particles locate at the intro-crystalline spaces of Ag^0Z pellets, the adsorption process also involves mass transfer and diffusion of the I_2 into the Ag^0Z pellet.

To understand the adsorption process, adsorption experiments were conducted and results are shown in **Figure 4-8** below. The two experiments were conducted at 150 $^{\circ}$C in dry air with an I_2 concentration of 10 ppmv. The completed loading experiment reached an equilibrium loading of 12.5 wt% in about 380 hours, followed by 50 hours of desorption to the remove physisorbed I_2. The partly loading experiment was done in the same manner and reached an I_2 loading of 5.5 wt.%. After a 50 hours desorption, the pellets were collected. It was noticed that there was no desorption of I_2 for the partly loading experiment, which indicated that at the initial part of the uptake, chemical adsorption took place preferentially. In addition, the overlapping of the uptake curves indicated the excellent reproducibility of the experimental system.

The Ag^0Z pellet fully loaded with I_2 and that partly loaded with I_2 were cut open to observe the inside pattern. As shown in the inset of **Figure 4-8**, the fully loaded pellet has a uniform pattern throughout the cross-section, while the partly loaded pellet shows a reacted shell and an unreacted core. The reacted shell has the same color as the fully loaded pellet and the unreacted core in the same brown color as the fresh reduced Ag^0Z. This observation suggested that, the adsorption process of I_2 on AgZ pellets was a shrinking core process. Furthermore, the partly loaded pellet has a clear interface between the reacted shown and the unreacted core, and no concentration gradient is observed. This suggests that the reaction of I_2 with the Ag particles is fast and the adsorption process is controlled by diffusion of I_2 in the pellets.
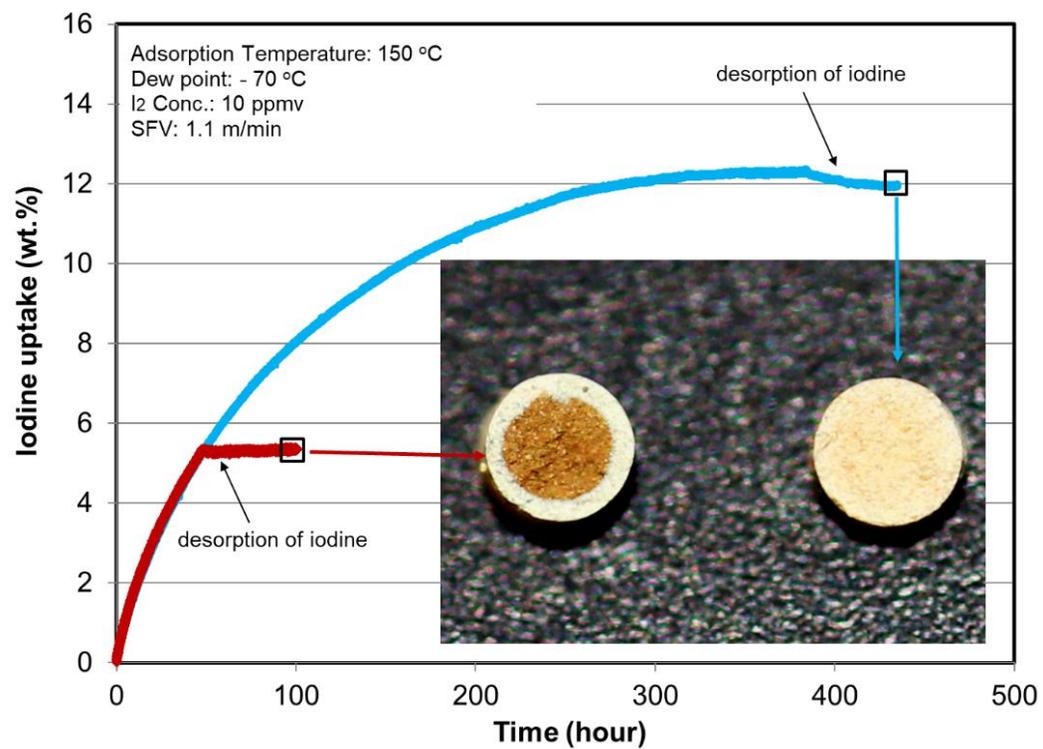
Figure 4-8. A comparison of the cross-section of Ag^{0}Z fully loaded with I$_2$ and that partly loaded with I$_2$. The clear interface observed in the Ag^{0}Z partly loaded with I$_2$ suggests that the adsorption process is a shrinking core process.

4.4. The Effect of Superficial Gas Velocity

The superficial gas velocity affects the adsorption kinetics through influencing the external gas film mass transfer resistance. To evaluate the effect of gas velocity, experiments with a single layer of Ag^0Z were conducted at 150 ^oC at varying gas velocities ranged from 0.55 to 4.4 m/min. The uptake curves plotted in **Figure 4-9** show that there is no significant difference in uptake rate when the gas velocity is in the range of 1.1 – 4.4 m/min. The uptake of I_2 with ~25 ppmv I_2 over gas velocities of 1.1 and 2.2 m/min, and with ~9 ppmv I_2 over gas velocities of 1.1 and 4.4 m/min are very close. However, the I_2 uptake with 50.9 ppmv I_2 over gas velocity of 0.55 m/min is significantly slower compared to that with 51.2 ppmv over gas velocity of 1.1 m/min. Despite the minor difference of I_2 concentration in the comparisons, these results suggest that the effect of external mass transfer resistance at gas velocities of 1.1 – 4.4 m/min on the adsorption process is not significant, while at low gas velocity such as 0.55 m/min the impact of the external mass transfer resistance cannot be ignored. **Figure 4-10** compares the uptake rates of the curves in **Figure 4-9**, which also indicates that there is no significant impact by gas velocity until it is decreased to 0.55 m/min. Accordingly, the single-layer adsorption experiments were conducted with the gas velocities of 1.1 m/min.
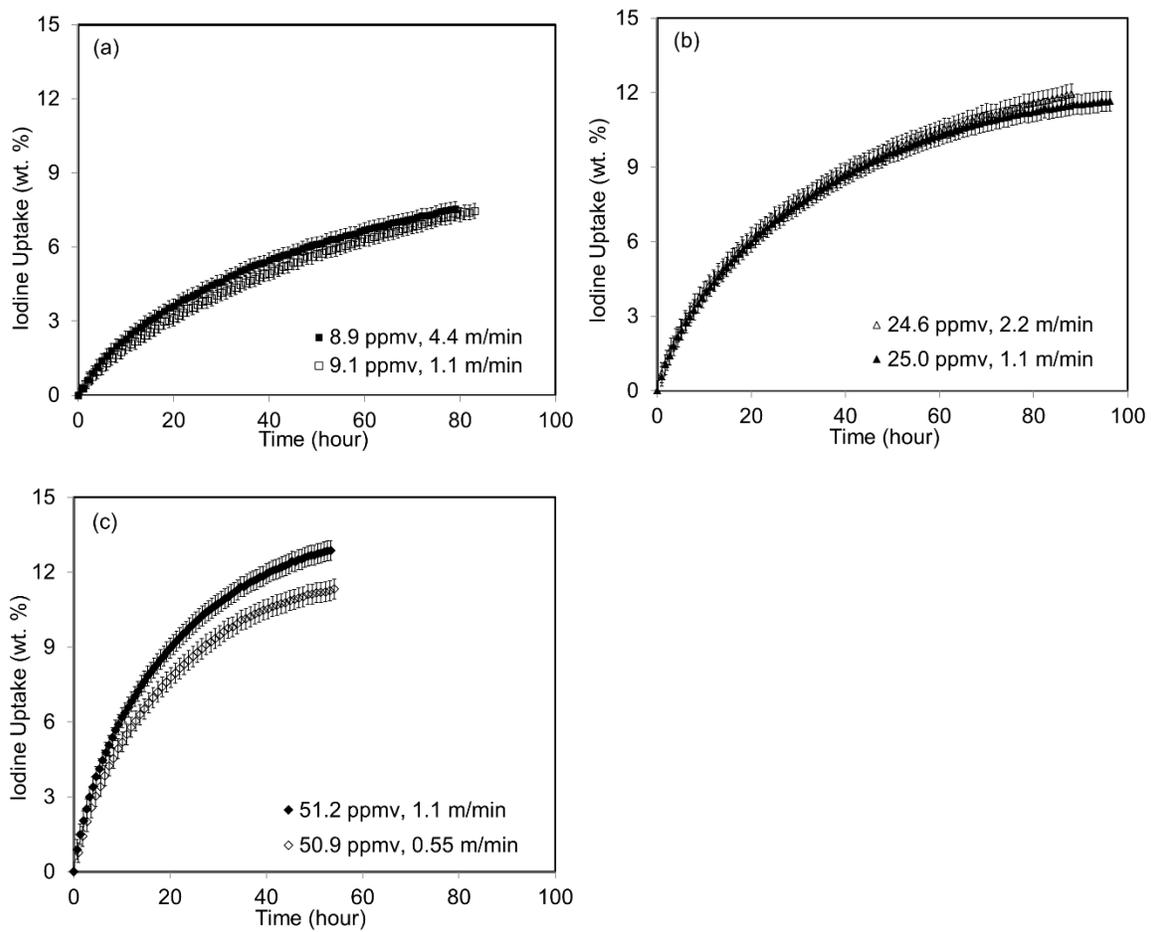
Figure 4-9. Effect of gas velocity on the uptake rate of I_2 on Ag^0Z at 150 $^{\circ}$C with different I_2 concentrations in the gas stream.
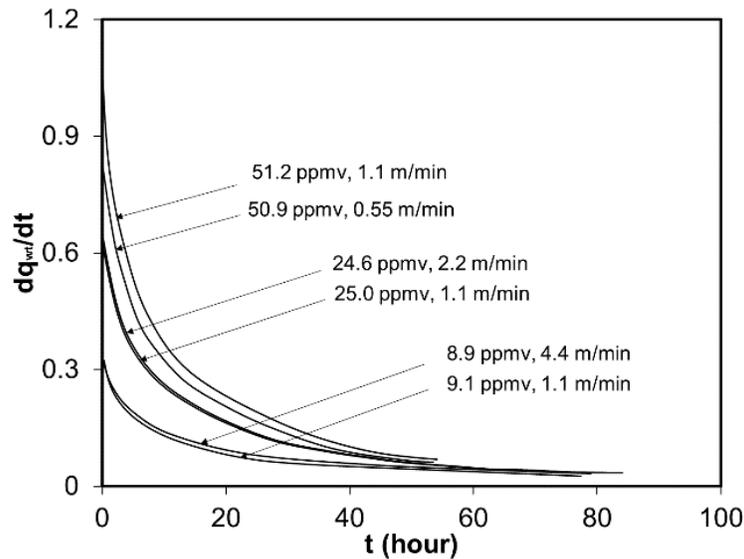
Figure 4-10. Comparison of the uptake rates of uptake curves in Figure 4-9. q_{wt} (wt. %) is the concentration of I_2 in Ag^0Z.

4.5. I_2 Adsorption Uptake Curves and Isotherms

The I_2 uptake curves obtained with the continuous-flow adsorption systems at 100, 150, 175 and 200 ^oC are plotted in **Figure 4-11**, which take up to 500 hours to reach equilibrium. The I_2 uptake rate increased as the I_2 concentration increased, but the equilibrium I_2 loading did not vary significantly. For instance, at 100 ^oC, the adsorption at 39.9 ppmv took about 130 hours to reach equilibrium while it took approximately 400 hours at 10 ppmv. However, both adsorptions achieved about 11 wt. % I_2 loading at equilibrium, which indicated the adsorption was mostly chemisorption. The color of the pellets changed from gray to yellow which also meant that I_2 was chemisorbed. At 150 ^oC and with similar I_2 concentrations, the I_2 loadings were more than 12 wt. %, which

suggested that the capacity of the Ag^0Z was mainly impacted by temperature. It is noted that at 150 °C there are differences in equilibrium I_2 loading at similar I_2 concentrations. The deviations could be due to the heterogeneity of the sorbents in pellet size and possible differences in physical/chemical structure between single extrudated pellets. Even through multiple pellets were used in the experiments to minimize this impact, minor variations may still exist.
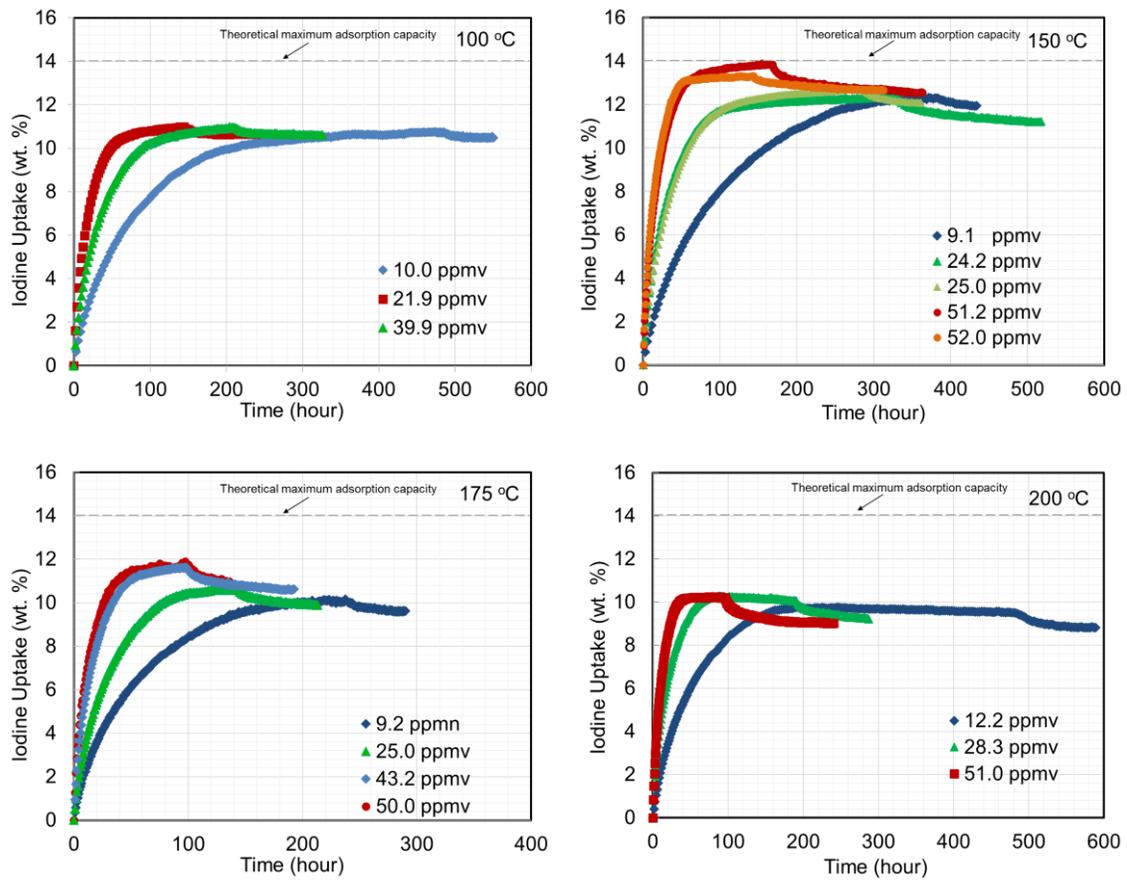
Figure 4-11. Uptake curves of I_2 adsorption on Ag0Z at 100, 150, 175, and 200 ^oC, over I_2 concentration between 9 - 52 ppmv.

The amount of physisorbed I_2 was estimated by desorption experiments assuming that the physisorbed I_2 was not strongly bonded with silver and thus was desorbed in clean dry air. The fraction of physisorbed I_2 to the total adsorbed I_2 was found to range from 3% to 9%, which indicated that the adsorption of I_2 on Ag^0Z was mostly chemisorption. As expected, the amount of physisorbed I_2 increased with I_2 concentration.

The equilibrium data of I_2 adsorption on Ag^0Z are plotted in **Figure 4-12**. **Figure 4-12a** displays the isotherms of total adsorption of I_2 with contributions by both physisorption and chemisorption. An average maximum I_2 loading of 13.5 wt. % was achieved at the optimal temperature of 150 ºC. This optimal adsorption temperature agreed with previous studies. [31-35, 39-47] The linear isotherms show a slight slope, which mostly due to the increase of physisorbed I_2 as the I_2 concentration in the gas stream increased. The isotherms of chemisorption shown in **Figure 4-12b** are almost constant lines that only affected by the adsorption temperature rather than I_2 concentration. The average chemisorption at 150 ºC is 12.3 wt. %, corresponding to an 88% silver utilization efficiency. The incomplete Ag utilization could be due to the unavailability of the silver in the channels and pores of the crystals that were closed or blocked, so that the silver could not move to the surface of mordenite during the reduction. In addition, the reaction may have reached an equilibrium at 150 ºC, so the forward Ag-I reaction is not 100% complete.
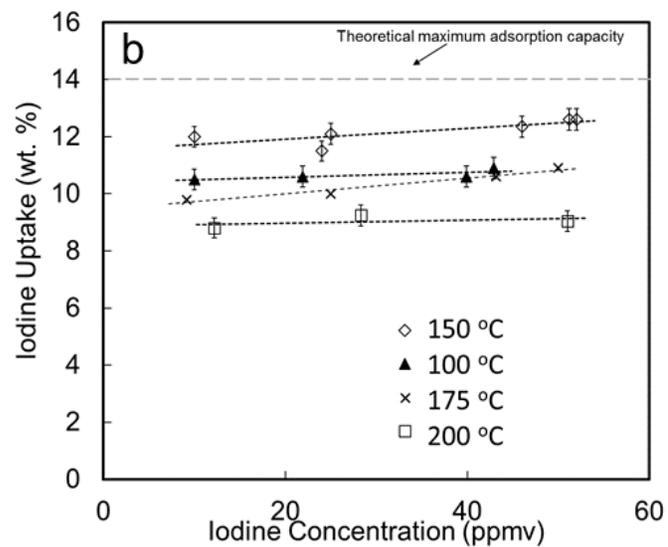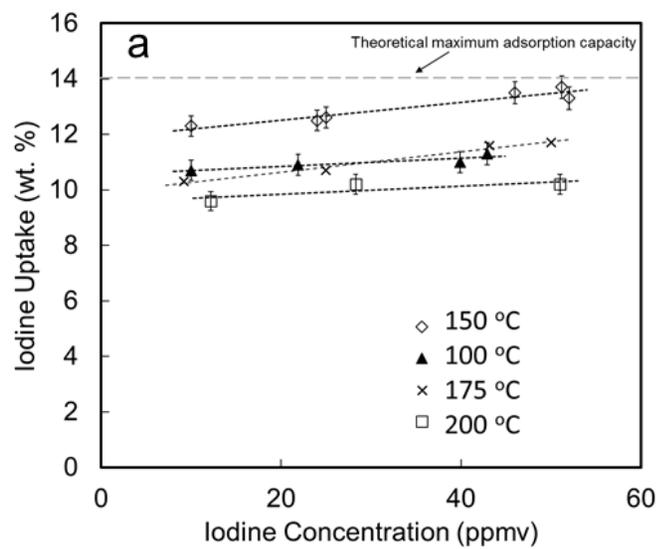
Figure 4-12. Isotherms of I_2 adsorption on Ag^0Z. a) Total adsorption; b) Chemisorption.

4.6. Effect of Temperature

It is found that temperature affects the I_2 loading capacity of Ag^0Z through the impact on chemisorption (Ag-I reaction). However, the effect of temperature on the I_2 loading capacity is not linear. The equilibrium I_2 adsorption capacity of Ag^0Z increased as the temperature increased from 100 to 150 ºC, but decreased when further raised the temperature to 200 ºC. Theoretically, the equilibrium adsorption capacity is expected to decrease with increasing temperature. The opposite change of I_2 loading capacity from 100 to 150 ºC could be due to the impact of the H_2O existing in the mordenite structure. Previous studies of I_2 adsorption with Ag^0Z[22-23, 31, 57, 150] have shown that H_2O adsorbed in Ag^0Z has an adverse effect on the I_2 capacity of Ag^0Z. They reported that at higher temperatures such as 150 ºC, there is less adverse effect of H_2O in the off-gas streams compared to low temperatures (room temperature), because the relative vapor pressure of H_2O is lower. Consequently, there is less H_2O present to react with Ag and AgI forming Ag_2O or AgOH. Also, H_2O content in the zeolite will be lower permitting I_2 to enter pores or pass between crystals. Accordingly, the adverse effect of H_2O at 423K should be smaller than that at 100 ºC. In the single-layer adsorption experiments of this study, the Ag^0Z was pre-equilibrated at desired adsorption conditions in the gas stream without I_2 to remove the moisture in the pellets before starting I_2 adsorption. In other words, for experiments at 100 ºC, the Ag^0Z was pre-equilibrated at 100 ºC, and for experiments at 150 ºC, the Ag^0Z was pre-equilibrated at 150 ºC. Therefore, the pre-equilibration at 100 ºC gave more moisture remaining in Ag^0Z than that at 150 ºC, and consequently a stronger effect by the H_2O. **Figure 4-13** shows the desorption (removal) of H_2O when Ag^0Z was equilibrated in the

gas stream without I_2 at 100, 150 and 200 ^oC, sequentially. As the temperature was increased, more H_2O was desorbed, resulted in less effect of the H_2O. Therefore, the I_2 capacity at 150 ^oC was higher than 100 ^oC.
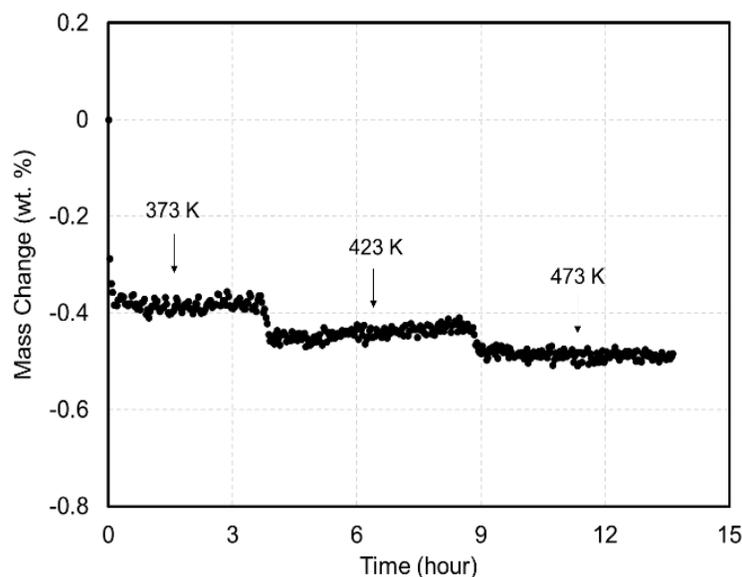
Figure 4-13. Desorption of H_2O when Ag0Z is equilibrated in dry air stream (dew point: -70^oC) at 100 (373 K), 150 (423 K), and 200 ^oC (473 K), sequentially.

However, the less adverse effect of H_2O at a lower temperature cannot explain the decrease of I_2 capacity when increasing temperature from 150 to 200 ^oC. Extended experiments were conducted at 250 ^oC, and a different behavior (**Figure 4-14**) to those at 100 – 200 ^oC was observed. As anticipated, the I_2 capacity at 250 ^oC further decreased, but the uptake curve started to drop at the 35-hour point without stopping the I_2 in the gas stream. The weight loss was a slow process that took about 200 hours to fall from 7.5 wt. % to 6.5 wt. %. Similar results were obtained from a replicate experiment. Since there were no changes in dew point and I_2 concentration in the gas stream during the experiments, desorption of H_2O or I_2 should not occur. Therefore, the weight loss should be due to the decomposition of AgI formed on Ag^0Z to release I_2 and silver. And this silver may be in

60

some chemical form that could not react with I_2 to form AgI again. As more AgI was formed, the rate of decomposition became faster than formation, resulting in the weight loss of adsorbents. After about 200 hours, the formation and decomposition of AgI reached equilibrium. The decomposition also explains the decrease in I_2 capacity of Ag^0Z when the temperature was increased from 150 to 200 °C. The decrease in I_2 capacity due to the decomposition of AgI overcame the increase due to the effect of less H_2O in the Ag^0Z pellets.
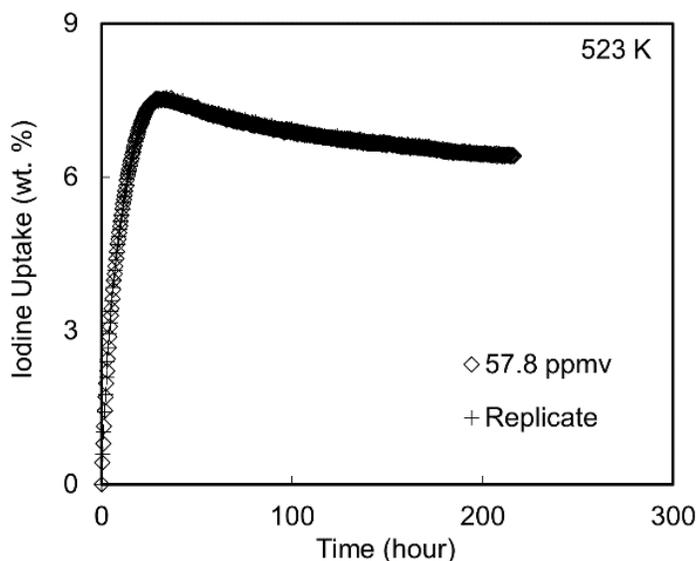
Figure 4-14. Uptake curves of I_2 adsorption on Ag^0Z at 250 °C (523K). A decrease in mass is observed from 35 hours without stopping I_2 in the gas stream which is due to possible decomposition of AgI.

However, this observation of decomposition at 250 °C varies from those reported in previous studies that bulk AgI and AgI inside zeolite crystals decomposed at temperatures above 400 °C.[63-65] In addition, by thermodynamic calculations, equilibrium vapor pressures

of I_2 over bulk AgI for the Ag-I reaction at 200 and 250 °C in terms of concentration are 0.049 and 0.245 ppm, respectively, which means that AgI decomposition should not occur at the experimental conditions performed where the I_2 concentrations were 9- 52 ppmv. The reason could be that the AgI nanoparticles formed on the mordenite crystal surface by I_2 reacting with silver nanoparticles are more susceptible to decomposition than bulk AgI and AgI formed inside zeolite crystals. However, future work including chemical analyses is needed to confirm the AgI decomposition in Ag^0Z.

4.7. Kinetics

The kinetic data were fitted by the SC model with different combinations of controlling terms as shown in Eq. (1), (6) and (7) and model parameters were evaluated. Since the external gas film mass transfer resistance did not have significant impact on the uptake kinetics under the conditions studied, the gas film mass transfer coefficient (k_f) in τ_I was estimated by the Ranz and Marshall correlation:[151]

$$Sh = 2 + 0.6 Sc^{1/3} \, Re^{0.5} \quad (23)$$

where Sh, Sc and Re are the dimensionless Sherwood number, Schmidt number and Reynolds number. The effect of the pellet-supporting screen on k_f is assumed negligible.

The I_2 molecular diffusivity was estimated by the Fuller et al.[152] correlation,

$$D_{AB} = \frac{0.00143 T^{1.75}}{P M_{AB}^{1/2} \left[\left(\sum v \right)_A^{1/3} + \left(\sum v \right)_B^{1/3} \right]^2} \quad (24)$$

where the subscripts A and B denote I_2 and air, respectively, P is the pressure in bar, M_{AB} is the average molecular weight defined by $M_{AB} = \dfrac{2}{1/M_A + 1/M_B}$, and v is the atomic

diffusion volume. For the I_2-air system, $P = 1$ bar, $M_{AB} = 52.0 \, \text{g/mol}$, $\left(\sum v\right)_A = 59.6$ and $\left(\sum v\right)_B = 19.7$.[153] The kinematic viscosity of air needed for estimating the gas film mass transfer coefficient were estimated by REFPROP.[154]

Average values of the pore diffusivity (D_p) and reaction constant (k_s) were estimated by least-square fitting of the uptake curves and were substituted into Eq. (1), (6) and (7) to predict the I_2 adsorption on Ag^0Z. **Figure 4-15** shows the comparison of the predictions by the three equations at 200 °C. The SC model with all controlling terms showed an excellent capability to fit the experimental data, while the model with only mass transfer or reaction controlling terms could not describe the I_2 adsorption process well. This result suggests that both mass transfer and reaction control the adsorption process of I_2 on Ag^0Z.
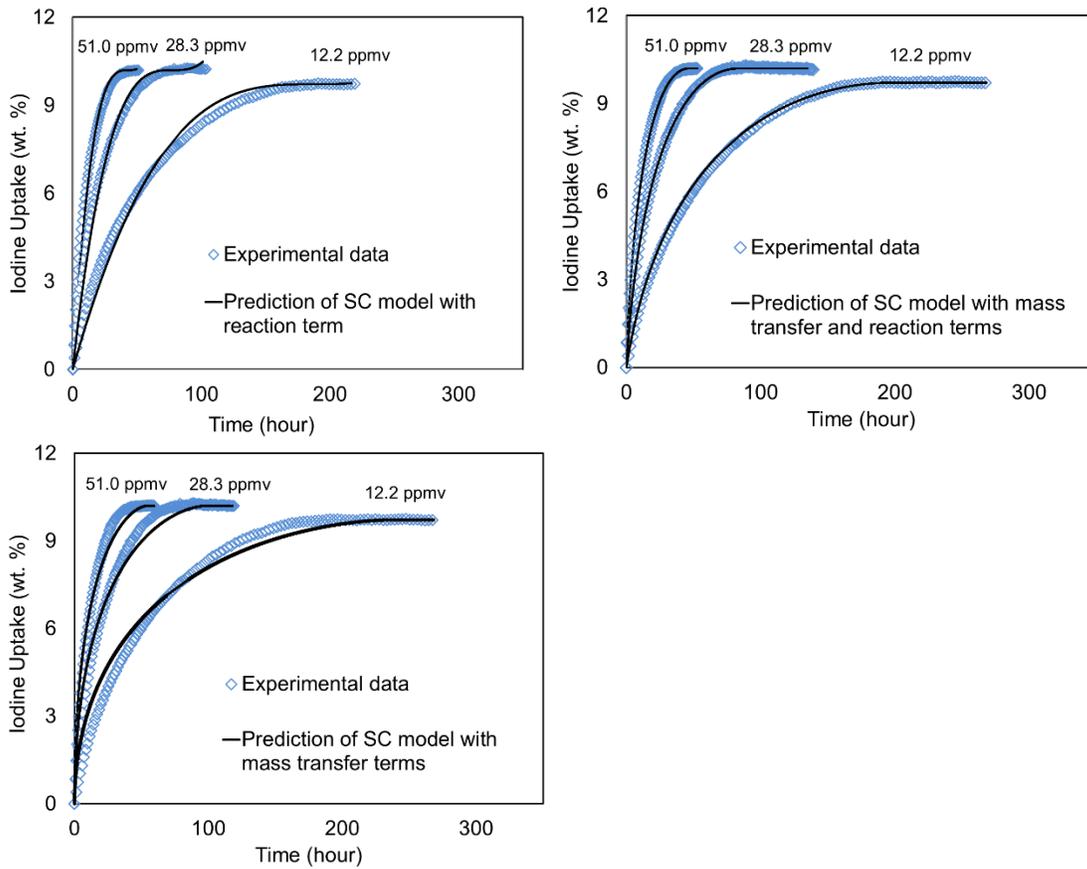
Figure 4-15. Comparison of the prediction of the SC model with different combinations of rate controlling terms.

The curve-fitting error was estimated by the average absolute relative deviation (AARD) expressed as following Eq. (25).

$$AARD(\%) = \sum_{i=1}^{n} \left| \frac{y_i^{exp} - y_i^{mol}}{n y_i^{exp}} \right| \times 100 \qquad (25)$$

where the subscript i indicates the ith data point of the total n data points, and superscripts *exp* and *mol* represent the experimental data and model prediction, respectively. The comparison of fitting results using the AARD and calculated parameters for the different models is shown in **Table 4-1**. The average AARD of 1.57% indicates that the SC model with all rate controlling terms can describe the I_2 adsorption better than the models with only mass transfer or reaction controlling terms, which have average AARDs beyond the acceptable range. The coefficients and the reaction constant increase with temperature, which implies that high temperature favors the rate of mass transfer and Ag-I reaction.

Table 4-1. Variables and model parameters for the SC Model

T	v [24]	D_{AB}	SC model with mass transfer terms			SC model with reaction term		SC model with mass transfer and reaction terms			
			k_f	D_p	AARD	k_s	AARD	k_f	D_p	k_s	AARD
(°C)	(cm²/s)	(cm²/s)	(cm/s)	(cm²/s)	(%)	(cm/s)	(%)	(cm/s)	(cm²/s)	(cm/s)	(%)
100	0.232	0.144	6.49	2.41×10^{-3}	6.47	6.08×10^{-2}	7.06	6.49	4.91×10^{-3}	0.132	1.42
150	0.284	0.179	7.45	2.85×10^{-3}	5.23	7.60×10^{-2}	7.22	7.45	5.58×10^{-3}	0.164	2.02
200	0.348	0.218	8.42	3.79×10^{-3}	8.38	9.72×10^{-2}	6.47	8.42	8.07×10^{-3}	0.196	1.26
Ave.					6.69		6.92				1.57

The model parameters of all sets of conditions obtained for the SC model with mass transfer and reaction terms of Eq. (1) are listed in **Table 4-2**. The good agreement of D_p and k_s values at each temperature and the very small AARD at all sets of conditions confirm the good capability of the model to predict the I_2 uptake process. As mentioned above, the

silver nanoparticles in Ag^0Z locate on the surface of the mordenite crystals. Therefore, the obtained pore diffusion (D_p) mainly describes the diffusion of I_2 molecules through the macropores between the modenite crystals rather than the micropores in the mordenite crystals. As expected, the values of D_p and k_s increased with temperature as the rates of diffusion and reaction would be faster at a higher temperature. The values of τ_2 and τ_3 are of the same order, and both are about two orders of magnitude greater than τ_1, indicating the effects of pore diffusion resistance and reaction resistance on the I_2 uptake rate are much more significant than that of external gas film mass transfer resistance. Therefore, the major mechanisms of I_2 adsorption on Ag^0Z under the studied conditions are pore diffusion through the adsorbent and Ag-I reaction.

Table 4-2. Experimental results and model parameters for the SC Model with mass transfer and reaction controlling terms.

[I_2] (ppmv)	I_2 loading (kg/100kg)	τ_1 (h)	τ_2 (h)	τ_3 (h)	k_f (cm/s)	D_p (cm^2/s)	k_s (cm/s)	AARD%
				SC				
				100 ^{o}C				
10.0	10.62	2.70	1.71×10^2	1.38×10^2	6.49	4.96×10^{-3}	1.27×10^{-1}	1.29
21.9	10.85	1.26	7.85×10^1	6.42×10^1	6.49	5.04×10^{-3}	1.27×10^{-1}	1.21
39.9	11	7.00×10^{-1}	4.65×10^1	3.19×10^1	6.49	4.73×10^{-3}	1.42×10^{-1}	1.76
Avg					6.49	4.91×10^{-3}	1.32×10^{-1}	1.42
				150 ^{o}C				
9.1	12.3	3.43	2.13×10^2	1.73×10^2	7.45	5.81×10^{-3}	1.48×10^{-1}	1.43
24.2	12.3	1.29	7.93×10^1	5.37×10^1	7.45	5.85×10^{-3}	1.78×10^{-1}	1.80
25.0	12.5	1.26	8.13×10^1	5.71×10^1	7.45	5.52×10^{-3}	1.35×10^{-1}	2.83
51.2	13.7	6.74×10^{-1}	4.36×10^1	3.06×10^1	7.45	4.85×10^{-3}	1.68×10^{-1}	1.84
52.0	13.25	6.39×10^{-1}	3.94×10^1	2.50×10^1	7.45	5.86×10^{-3}	1.91×10^{-1}	2.20
Avg					7.45	5.84×10^{-3}	1.72×10^{-1}	2.02
				200 ^{o}C				
12.2	9.72	1.98	1.12×10^2	9.90×10^1	8.42	7.83×10^{-3}	1.83×10^{-1}	2.05
28.3	10.2	0.496	2.48×10^1	2.09×10^1	8.42	8.15×10^{-3}	2.00×10^{-1}	1.14
51.1	10.2	8.95×10^{-1}	4.44×10^1	3.68×10^1	8.42	8.22×10^{-3}	2.05×10^{-1}	0.58
Avg					8.42	8.07×10^{-3}	1.96×10^{-1}	1.26

4.8. Regeneration

Practically, the study of Ag^0Z regeneration may not be necessary due to that the adsorbents will be consolidated for long-term storage after saturated with radioactive I_2. However, for a better understanding the chemistry of the material and in consideration of its potential application in other industrial chemical processes, regeneration of Ag^0Z was investigated in this study through I_2 adsorption experiments and XAFS analyses.

The regenerated Ag^0Z pellets were prepared by treating the I_2 -loaded Ag^0Z in a 4% H_2/96% Argon stream at 500 ^{o}C for 24 hours. The procedure is the same as that stated in Section 3.2.1. Then I_2 adsorption on the regenerated Ag^0Z pellets was performed in a dry air stream containing I_2 of 50 ppmv and at the temperature of 150 ^{o}C. The uptake curves of I_2 adsorption on Ag^0Z and regenerated Ag^0Z were compared in **Figure 4-16**. It was observed that Ag^0Z mentioned the same capacity after one regeneration at 500 ^{o}C for 24 hours, which indicate that the AgI can be reduced entirely to Ag^0 in H_2 stream.
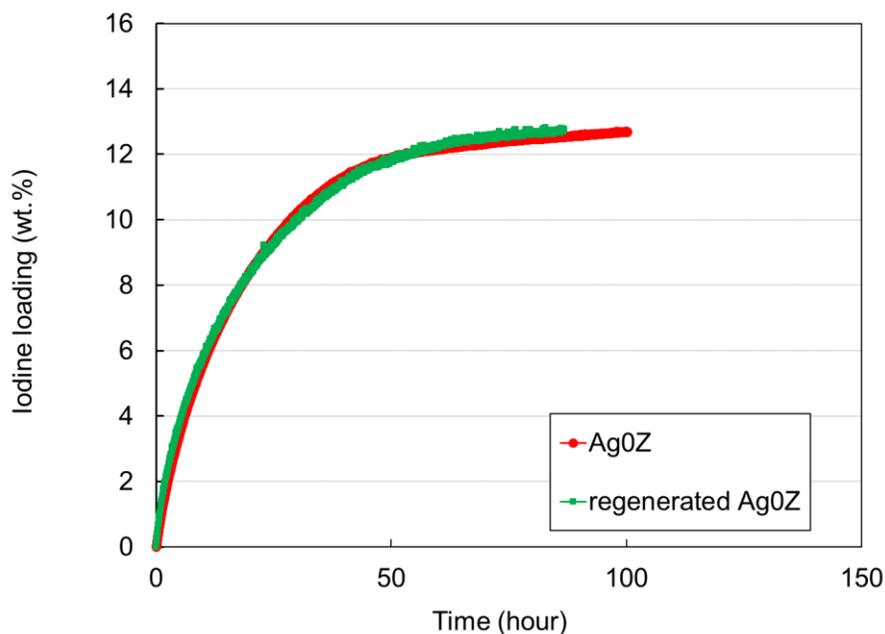
Figure 4-16. I_2 adsorption on Ag^0Z and regenerated Ag^0Z

The XANES spectra of Ag^0Z and regenerated Ag^0Z, as well as Ag foil, are shown in **Figure 4-17**. The results also show that AgI can be fully regenerated by contact with H_2 at 500 °C for 24 hrs, returning to the Ag^0 oxidation state with no obvious residual AgI remaining. The second contact with I_2, resulting in the recycled Ag^0Z, displays an identical spectrum as the initial I_2 -contacted AgZ while suffering no decrease in I_2 adsorption performance. While further cycles are needed for confirmation, this finding suggests the simple act of reduction, I_2 exposure, regeneration, and recycle does not directly impact the performance of the Ag^0Z for I_2 adsorption, and that deactivation is attributable to a different gaseous component not considered in this study.
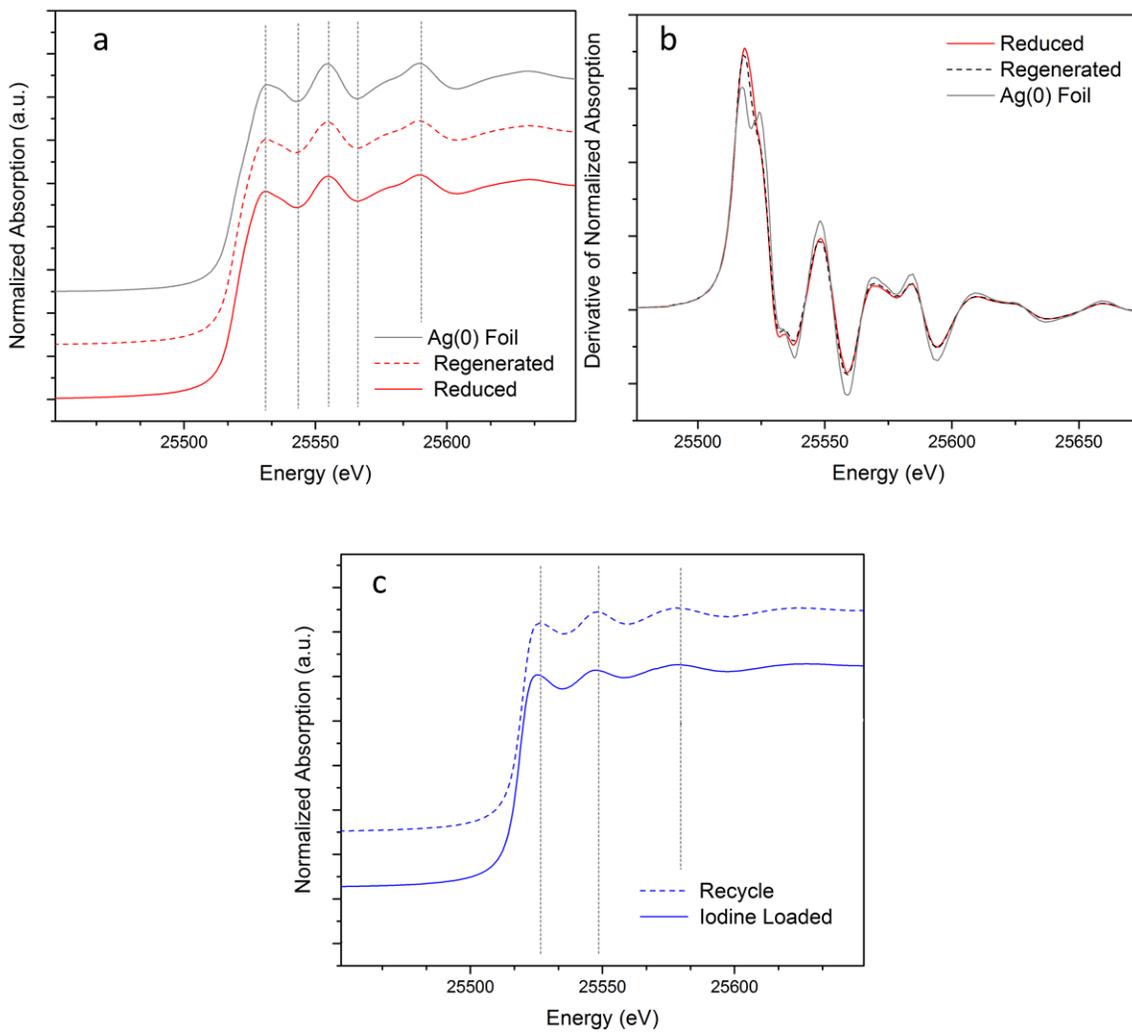
Figure 4-17. XANES spectra for Ag⁰Z samples. a) Normalized spectra of Ag^0Z, regenerated Ag^0Z and Ag foil samples. Dashed grey lines are drawn at characteristic spectral features. b) The derivative of the XANES spectra in a). c) Normalized spectra of I_2-loaded Ag^0Z and I_2-loaded regenerated Ag^0Z (Recycle).

4.9. Conclusions

To better understand I_2 adsorption pathway in Ag^0Z, analyses of XRD, SEM-SES, XAFS, and XANES were conducted to corroborate generation of surface Ag^0 particles upon reduction and formation of AgI upon exposure to I_2. The adsorption was found to be shrinking core process according to the partly I_2 loading experiments and modeling results.

The optimal reduction conditions of Ag^0Z (12.0 wt.% Ag) used in this study were found to be at 400 ^{o}C and for 24 hours. Based on the equilibrium data from single-layer pellet adsorption experiments, the adsorption of molecular I_2 on Ag^0Z is mostly chemisorption through the Ag-I reaction. The optimal adsorption temperature was found to be 150 ^{o}C, which confirmed the conclusions in previous studies. An average maximum I_2 loading of 12.3 wt. % by chemisorption (13.5 wt. % by both chemisorption and physisorption) was achieved at 150 ^{o}C, and the corresponding Ag utilization efficiency is 88%. The lower I_2 capacity at temperatures lower than 150 ^{o}C can be explained by the stronger adverse effect of H_2O in the adsorbents. Future work is needed to study details of H_2O effects. The decrease in I_2 capacity at temperatures beyond 150 ^{o}C could be due to the decomposition of AgI nanoparticles at temperatures above 150 ^{o}C, according to the experimental observations. More investigations in future studies are needed to confirm this explanation.

Furthermore, the Shrinking Core model with mass transfer and reaction controlling terms is capable of describing the kinetics of I_2 adsorption on Ag^0Z with an average AARD of 1.57%. The primary controlling mechanisms were found to be diffusion through macropores of the adsorbent and the Ag-I reaction. The effect of gas film mass transfer resistance on the adsorption process is not significant at the experimental conditions

studied. The parameters indicate that high temperature favors the adsorption rate by increasing the rate of gas film mass transfer, pore diffusion, and reaction.

Finally, investigation of the Ag^0Z regeneration indicated the Ag could be entirely reduced for subsequent I_2 adsorption, resulting in the same I_2 loading capacity as before. The results provide valuable information for future studies of Ag^0Z deactivation and methods for capacity recovery.

Chapter 5. H_2O Adsorption on Ag^0Z [§]

5.1. Introduction

Reduced silver-exchanged mordenite (Ag^0Z) has been recognized as the state-of-art adsorbent for I_2 retention in the nuclear fuel reprocessing off-gas treatment. It has also been shown to have a considerable adsorption capacity for H_2O vapor, which is also a major component in the off-gases of spent nuclear fuel reprocessing facilities. Therefore, understanding H_2O vapor adsorption on Ag^0Z is necessary for a better design of off-gas treatment systems.

The kinetics was studied through adsorption experiments of H_2O vapor on Ag^0Z pellets and analyses of the kinetic data with adsorption models that describe processes of mass transfer and inter/intra-crystalline diffusion. Uptake curves of H_2O vapor on Ag^0Z pellets were obtained with a continuous-flow adsorption system at temperatures of 25, 40, 60, 100, 150, and 200 °C and dew points from -53.6 to 12.1 °C. The diffusion controlling factors were determined experimentally and analytically. It was found that the diffusion process of H_2O vapor in Ag^0Z pellets was controlled by macropore diffusion. Gas film mass transfer resistance also contributed to the adsorption process of the 0.9 mm Ag^0Z pellets, but it could be minimized with a high gas velocity and small pellet radius. Kinetic models including macropore diffusion (MD), linear driving force (LDF) and shrinking core (SC) were used to fit the uptake curves. The macropore diffusivity for H_2O vapor

---

[§] Permission granted by American Chemical Society to use the text of published article[63] in this chapter.

63. Nan, Y.; Lin, R.; Liu, J.; Crowl, T. B.; Ladshaw, A.; Yiacoumi, S.; Tsouris, C.; Tavlarides, L. L., Adsorption Equilibrium and Modeling of Water Vapor on Reduced and Unreduced Silver-Exchanged Mordenite. Industrial & Engineering Chemistry Research 2017, 56 (28), 8095-8102.

adsorption on Ag^0Z pellets was determined using the three models. It was found that the LDF and SC models could well describe the kinetic process, while the fitting with the MD model was not quite as good due to the existence of external mass transfer resistance for the 0.9 mm Ag^0Z pellets.

The isotherms of H_2O (nonradioactive H_2O) on Ag^0Z were obtained at temperatures of 25, 40, 60, 100, 150, and 200 ^oC with a continuous-flow adsorption system. The data were analyzed using the Heterogeneous Langmuir and Generalized Statistical Thermodynamic Adsorption (GSTA) models, and thermodynamic parameters of the isotherms were obtained from both models. Both models were found capable of describing the isotherms. Isotherms of H_2O on the unreduced silver mordenite (AgZ) were also collected at 25, 40, and 60 ^oC and parameterized by the GSTA model. Through the comparison of the isotherms of Ag^0Z and AgZ, it was found that Ag^0Z had a higher H_2O adsorption capacity than AgZ. The comparison of their thermodynamic parameters suggested that the interaction of H_2O molecules with the H^+ in Ag^0Z was stronger than that with the Ag^+ in AgZ.

5.2. Kinetics

5.2.1. Determination of diffusion control factors and micropore diffusivity

To better understand the adsorption process of H_2O vapor on Ag^0Z pellets, experiments were performed to investigate the rate controlling factors of the adsorption kinetics. Zeolite (including mordenite) pellets are made of zeolite crystals and binder materials, and they are bi-porous materials containing both intra-crystalline micropores and inter-crystalline macropores. The physisorption process of a zeolite pellet is often

controlled by micropore diffusion, or macropore diffusion, or both. If micropore diffusion controls the adsorption process, the fractional adsorption rate should be independent of the size of pellets; while in the case of macropore diffusion control or both, the fractional adsorption rate will depend on the pellet size. Furthermore, when macropore diffusion is controlling the adsorption process, the initial fractional adsorption rate will be inversely proportional to the pellet radius.[143, 155-156] Based on this theory, H_2O adsorption experiments were performed with Ag^0Z pellets of different radii to determine the rate controlling process. The Ag^0Z pellets (radius = 0.9 mm) were ground and sieved to average radii of 0.4 mm, 0.18 mm and 0.09 mm, and then loaded with H_2O vapor at 40 ^oC in the gas stream of dew point -40 ^oC. Replicates of experiments were conducted to determine experimental uncertainties.

In addition, efforts were made to experimentally determine the micropore diffusivity by adsorption of H_2O on Ag^0Z powder which passed through a 120-mesh sieve. The average particle radius of the powder was measured as 50 μm. The micropore diffusivity was determined by fitting the uptake curves with the LDF model assuming the radius of the powder was small enough so that the gas film mass transfer and macropore resistances under the adsorption conditions were insignificant and therefore the total mass transfer coefficient k_{LDF} was only associated with the micropore resistance.

5.2.2. Diffusion control factors and micropore diffusivity

The uptake curves of the H_2O adsorption on Ag^0Z pellets of 0.09, 0.18, 0.4 and 0.9 mm radius at 40^oC in gas streams of dew point of - 40 ^oC are shown in **Figure 5-1**. The triplicate experiments had very close kinetics and reached the same maximum equilibrium loading (4.3 wt. %), which indicated the high accuracy and reliability of the experimental

data. The uptake curves also showed that the H_2O adsorption rate increased with the decrease of pellet radius, which suggested that macropore diffusion played a significant role in the adsorption kinetics.
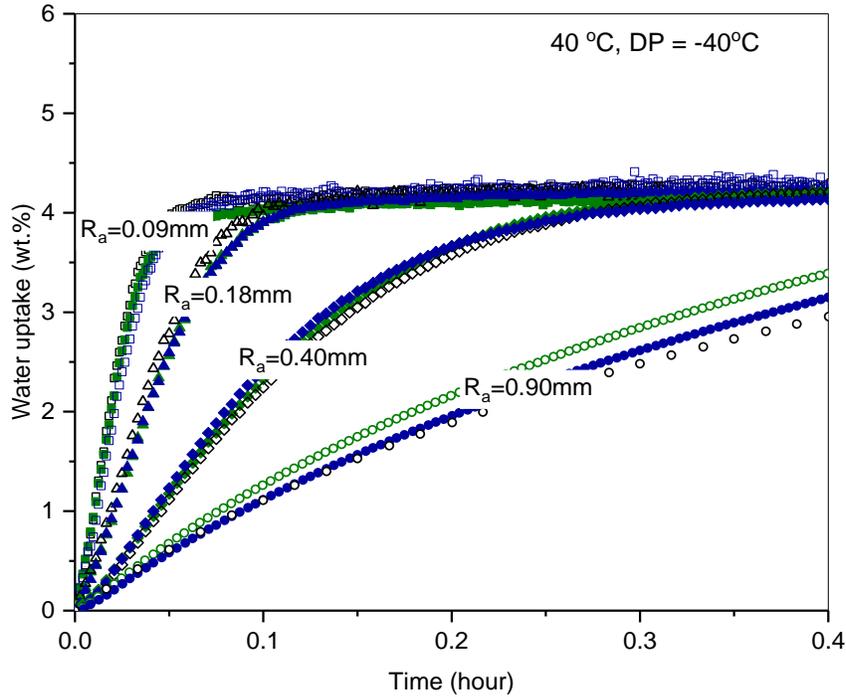
Figure 5-1. Uptake curves of H_2O adsorption on Ag^0Z of different particle radii at the temperature of 40 °C and dew point of -40 °C.

To further investigate the rate controlling diffusion process, the relationship between the initial fractional uptake rate and the pellet radius was studied. The results are plotted in **Figure 5-2** and summarized in **Table 5-1**. Assuming the gas film mass transfer resistance of the small particles was insignificant, it was found that the products of the pellet radius (R_a) and the slope of the initial fraction of the uptake curves (U_i) were generally around 2.1 (**Table 5-1**), meaning that the initial fractional adsorption rate was inversely proportional to the pellet radius. This result indicated that the adsorption of H_2O

76

vapor on Ag^0Z pellets was controlled by the macropore diffusion process. The smaller $R_a{\times}U_i$ value (1.80) for the 0.9 mm pellets could be due to a more significant gas film mass transfer resistance with larger pellets, which led to a slower initial fractional uptake rate. The gas film mass transfer resistance can be minimized with a sufficiently high gas flow velocity or small adsorbent radius.
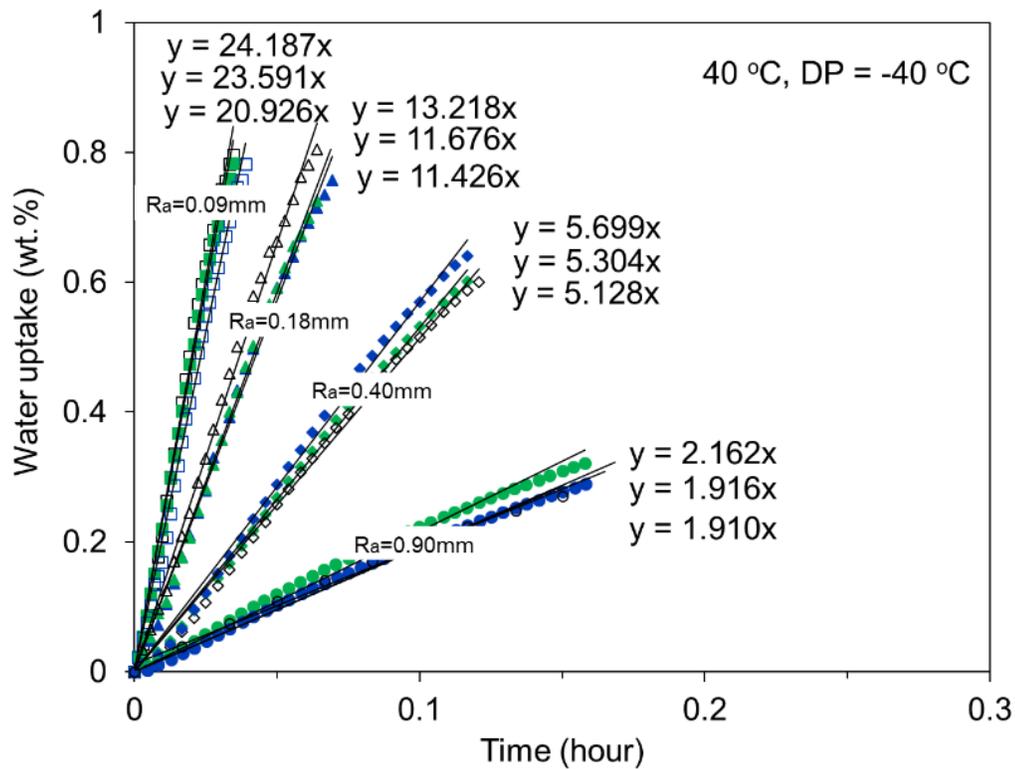
Figure 5-2. The initial fractional uptake rate of H_2O vapor on Ag^0Z was inversely proportional to the radius of the Ag^0Z particles, which indicated that the adsorption process was controlled by macropore diffusion.

Table 5-1. Change of initial factional uptake rate with pellet radius as shown in Figure 5-2.

Pellet Radius R_a (mm)	Initial Factional uptake rate U_i (hr^{-1})	$R_a \times U_i$
0.09	22.90	2.06
0.18	12.11	2.18
0.40	5.38	2.15
0.90	2.00	1.80

The micropore diffusivity of H_2O into the Ag^0Z crystals was estimated from the uptake curves of H_2O vapor on Ag^0Z powder using the LDF model. The uptake curves of H_2O vapor adsorption on Ag^0Z powder are shown in **Figure 5-3**. Adsorption reached equilibrium in about 4 minutes, which was more rapid compared to the adsorption on larger pellets as shown in **Figure 5-1**. Assuming the radius of the Ag^0Z powder was small enough so that the external gas film mass transfer and macropore diffusion resistances are negligible, the k_{LDF} can be expressed as:

$$\frac{1}{k_{LDF}} = \frac{R_i^2}{15D_i} \qquad (26)$$

Then the adsorption rate can be expressed as:

$$\frac{dq}{dt} = \frac{15D_i}{R_i^2}(q_e - q) \qquad (27)$$

By fitting the uptake curves with Eq. (27), an average D_i value of 1.59×10^{-12} cm^2/s was determined. It should be noted that the actual D_i value of H_2O on Ag^0Z crystals would be greater than this calculated value since the external mass transfer and macropore

diffusion resistance still existed during the adsorption on Ag^0Z powder. However, this fact does not influence the conclusions drawn from pore diffusion modeling results in Section 5.2.4 below.
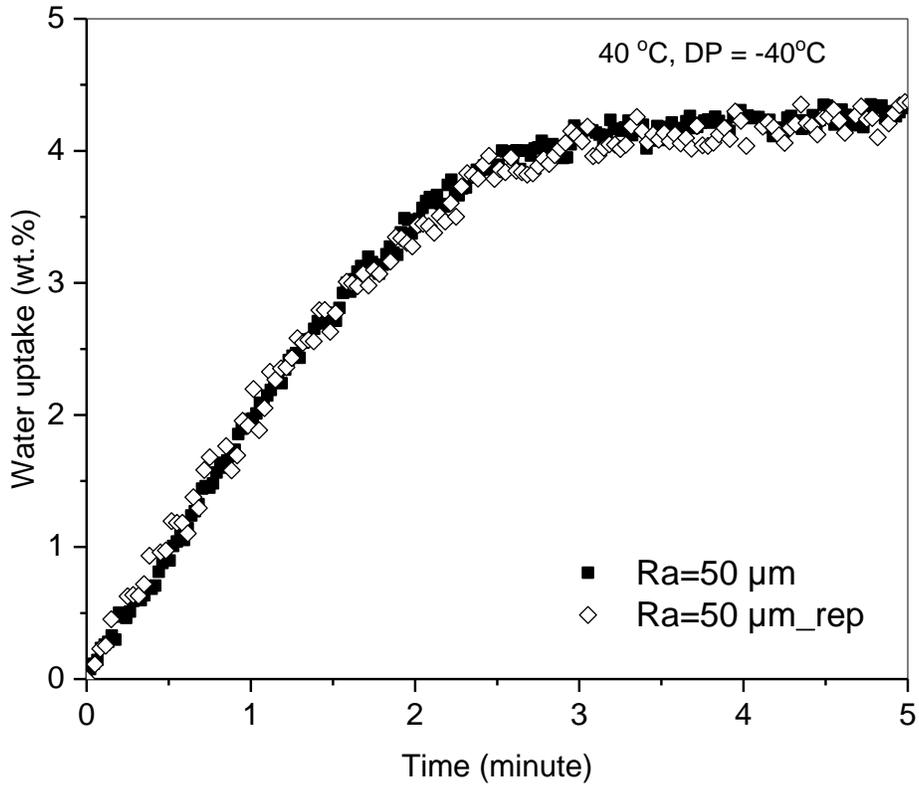
Figure 5-3. Adsorption of H_2O vapor on Ag^0Z powder ($R_a = 50$ μm) at the temperature of 40 ℃ and dew point of -40 ℃.

5.2.3. Uptake curves of H_2O on Ag^0Z

Uptake curves of H_2O vapor adsorption on 0.9mm Ag^0Z pellets were obtained at temperatures of 25, 40, 60, 100, 150 and 200 ^oC in gas streams of dew points between -53.6 to 12.1 ^oC. As shown in **Figure 5-4**, it took up to 50 hours for the Ag^0Z pellets to reach equilibrium at low adsorption temperatures and H_2O vapor concentrations (e.g. at 25 ^oC over dew point of -53.6 ^oC). While at high H_2O vapor concentration and high-temperature conditions, it took less than an hour to reach equilibrium. It was also observed that the uptake rate generally increased with adsorption temperature and the dew point of the gas stream. This was consistent with the fact that a higher adsorbate concentration and adsorption temperature results in faster diffusion kinetics. In addition, under the studied conditions, a maximum H_2O adsorption capacity of 8.5 wt.% was observed at 25 ^oC over a dew point of -1.8 ^oC, and a minimum capacity of 0.3 wt.% was observed at 200 ^oC over a dew point of -49.8 ^oC.
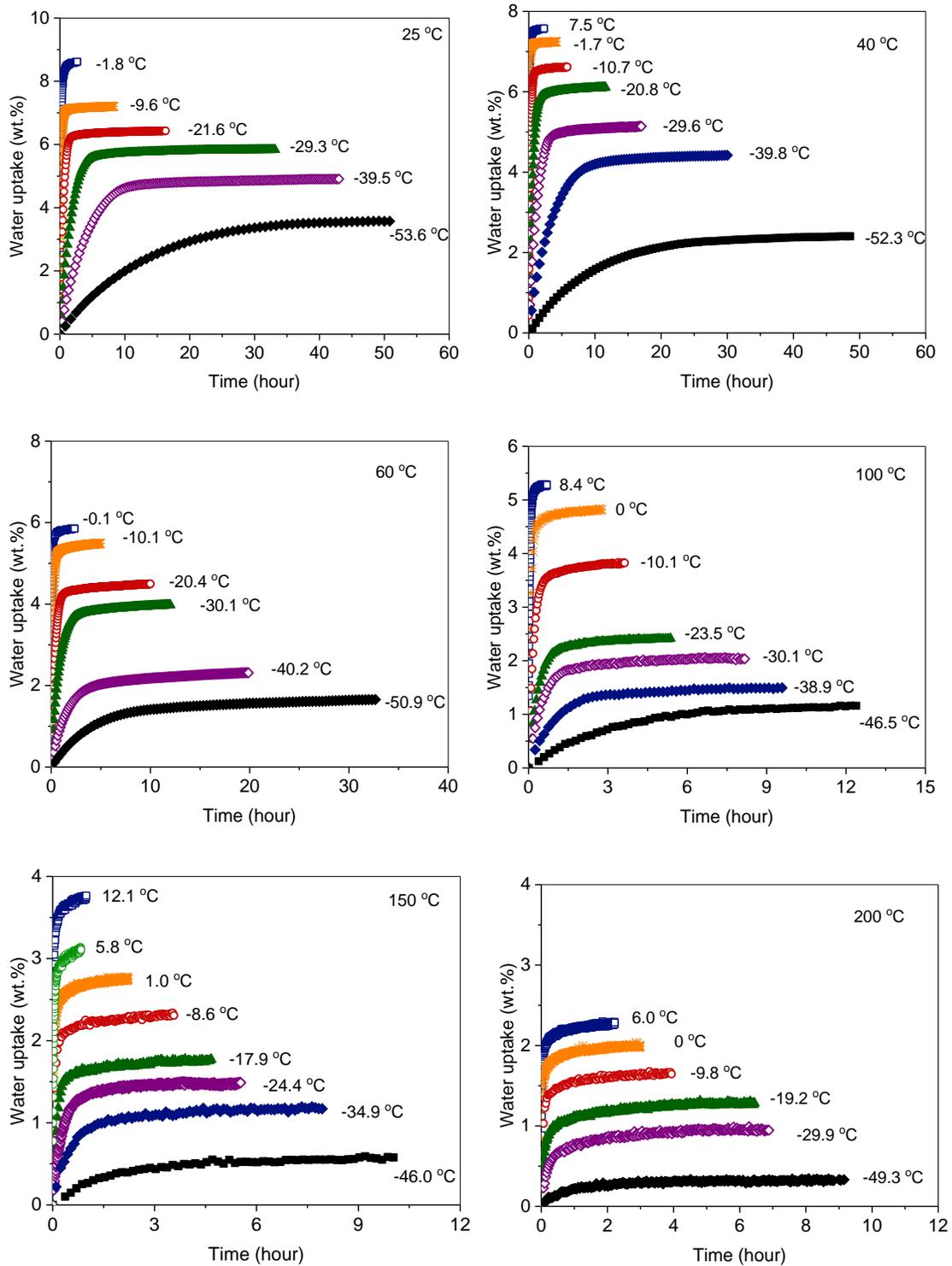
Figure 5-4. Uptake curves of H_2O vapor on 0.9 mm Ag^0Z in gas streams at temperatures from 25 to 200 °C and dew points from -53.6 - 12.1 °C.

5.2.4. Modeling

5.2.4.1. The pore diffusion models

The modeling with the pore diffusion models was realized by least-square fitting of the experimental data to determine the model parameters. Experimental results in above Section 4.1 have shown that the macropore diffusion is the rate controlling factor for the adsorption process of H_2O vapor on Ag^0Z. To further confirm this conclusion, curve-fitting by the bidisperse model (Eq. 10) and the macropore diffusion (MD) model (Eq. 15) were compared. It was found that the MD model had the same capability as the bidisperse model to fit the uptake curves as demonstrated by an example shown in **Figure 5-5**. As shown in the figure, with the D_i value of 1.59×10^{-12} cm^2/s applied to the bidisperse model, the difference between the macropore diffusivities (D_a) obtained from the two models was only 0.0084%. In addition, the prediction curves of the two models overlapped in the plot, which indicated that the micropore diffusion term in the bidisperse model had an insignificant contribution to the model prediction. This result further supported the conclusion from the experimental results that the H_2O adsorption process is dominated by macropore diffusion. Accordingly, the MD model was used to analyze the kinetic data in preference to the bidisperse model due to its less complexity.
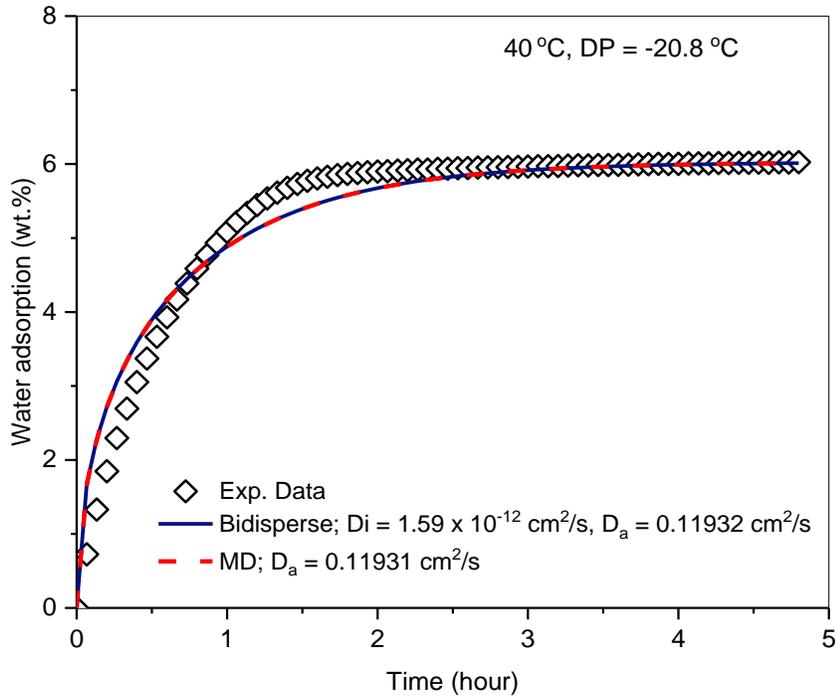
Figure 5-5. Comparison of the bidisperse and macropore diffusion models to fit the uptake curve of H_2O on Ag^0Z pellets (0.9 mm) at 40°C over the dew point of -20.8 °C. The prediction curves of the two models overlapped in the plot.

Results from the MD model for all uptake curves are showing in **Table 5-2**. The macropore diffusivity (D_a) was estimated for each experiment. It was observed that the value of D_a did not change significantly with the experimental conditions, and the average D_a slightly increased as the adsorption temperature increased. The curve-fitting error was estimated by Eq. (25) in Section 4.7. Note that the AARD shown in **Table 5-2** is the curve-fitting error of the model to the data with the average D_a value at each temperature. The average AARD for the MD model was found ranged from 3.65 – 8.27 % and the value decreased as the adsorption temperature increased, which indicated that the model fits the uptake curves better at high temperatures. The high AARD values also implied the

83

existence of gas film mass transfer resistance with the 0.9 mm pellets. Since the MD model does not account for the gas film resistance, the accuracy of curve fitting reduces as the temperature reduces and thus the gas film resistance increases.

Table 5-2. Experimental results and parameters obtained from the MD, LDF and SC models.

	DP (°C)	q_e (g/g)	C_b g/cm³	MD model D_a (cm²/s)	AARD (%)	LDF model k_{LDF} hr⁻¹	D_a (cm²/s)	AARD (%)	SC model τ_1	τ_2	D_a (cm²/s)	AARD (%)
25°C	-53.6	3.57E-02	1.25E-08	0.118	15.49	0.082	0.151	2.30	7.221	34.510	0.103	3.78
	-39.5	4.90E-02	9.96E-08	0.089	13.00	0.250	0.109	3.50	1.830	13.323	0.068	4.49
	-29.3	5.82E-02	2.99E-07	0.082	7.11	0.592	0.101	4.26	0.723	5.815	0.061	3.87
	-21.5	6.42E-02	6.54E-07	0.135	3.08	1.915	0.188	3.73	0.365	1.360	0.132	1.34
	-9.6	7.20E-02	1.97E-06	0.121	3.73	4.612	0.162	1.59	0.153	0.630	0.106	0.72
	-1.8	8.60E-02	3.85E-06	0.095	2.10	6.019	0.121	1.35	0.094	0.523	0.078	1.74
	Avg			*0.107*	*7.42*		*0.139*	*2.79*			*0.091*	*2.66*
40°C	-52.3	2.43E-02	2.06E-08	0.084	15.95	0.100	0.105	6.66	4.250	33.021	0.067	8.72
	-39.8	4.41E-02	9.17E-08	0.101	8.72	0.303	0.133	5.50	1.695	11.106	0.079	2.88
	-29.6	5.13E-02	2.76E-07	0.108	6.43	0.877	0.152	0.84	0.654	3.801	0.089	1.84
	-20.8	6.10E-02	6.66E-07	0.112	6.72	1.854	0.161	1.19	0.323	1.770	0.094	1.42
	-10.7	6.61E-02	1.70E-06	0.113	5.06	4.030	0.145	0.68	0.154	0.760	0.093	1.09
	-1.7	7.24E-02	3.70E-06	0.130	2.94	9.262	0.176	1.81	0.069	0.320	0.112	0.70
	7.5	7.57E-02	7.22E-06	0.096	4.35	13.058	0.123	0.83	0.042	0.259	0.074	1.37
	Avg			*0.107*	*7.17*		*0.142*	*2.50*			*0.087*	*2.75*
60°C	-50.9	1.70E-02	2.31E-08	0.085	17.11	0.210	0.140	5.52	2.727	20.410	0.066	6.00
	-40.2	2.30E-02	8.24E-08	0.089	11.82	0.544	0.137	4.53	1.036	6.815	0.075	4.84
	-30.1	4.00E-02	2.47E-07	0.121	9.15	1.150	0.178	1.93	0.602	2.530	0.117	2.41
	-20.4	4.41E-02	6.51E-07	0.114	3.85	2.618	0.167	1.15	0.251	1.163	0.107	1.38
	-10.1	5.45E-02	1.69E-06	0.116	4.66	5.269	0.158	0.81	0.120	0.593	0.099	1.31
	-0.1	5.78E-02	3.97E-06	0.115	3.02	11.527	0.155	0.86	0.054	0.268	0.099	1.37
	Avg			*0.111*	*8.27*		*0.156*	*2.47*			*0.094*	*2.89*
100°C	-46.5	1.22E-02	2.62E-08	0.093	16.25	0.265	0.110	6.08	1.347	13.38	0.064	10.12
	-38.9	1.52E-02	6.71E-08	0.111	5.37	0.895	0.191	2.95	0.656	3.632	0.114	2.99
	-30.1	2.00E-02	1.74E-07	0.135	3.22	1.789	0.195	2.10	0.334	1.681	0.125	2.12
	-23.5	2.42E-02	3.39E-07	0.109	3.51	2.456	0.159	1.98	0.233	1.439	0.091	2.58
	-10.1	3.78E-02	1.19E-06	0.100	2.88	4.904	0.137	2.30	0.092	0.730	0.080	2.65
	0	4.80E-02	2.82E-06	0.131	1.21	10.820	0.169	1.13	0.049	0.281	0.111	1.24
	8.4	5.27E-02	5.08E-06	0.149	2.65	20.650	0.205	1.69	0.030	0.147	0.129	1.69
	Avg			*0.122*	*5.01*		*0.167*	*2.60*			*0.102*	*3.34*
150°C	-46.0	6.50E-03	1.82E-08	0.075	10.22	0.439	0.135	8.08	0.894	12.590	0.052	10.52
	-34.9	1.21E-02	1.04E-07	0.083	3.77	1.546	0.158	3.44	0.290	2.810	0.074	3.83
	-24.4	1.45E-02	3.10E-07	0.095	3.31	3.293	0.132	3.10	0.117	1.230	0.069	3.63
	-17.9	1.80E-02	5.82E-07	0.103	2.80	6.169	0.171	3.40	0.077	0.580	0.097	3.33
	-8.6	2.30E-02	1.36E-06	0.119	2.82	13.493	0.214	2.34	0.042	0.233	0.133	2.40
	1	2.72E-02	3.03E-06	0.105	2.40	22.271	0.181	2.13	0.022	0.172	0.095	2.18
	5.8	3.06E-02	4.25E-06	0.110	2.85	26.539	0.172	2.31	0.018	0.139	0.095	2.53
	12.1	3.73E-02	6.51E-06	0.116	2.95	36.128	0.187	2.10	0.014	0.092	0.114	2.50
	Avg			*0.101*	*3.89*		*0.169*	*3.36*			*0.092*	*3.87*
200°C	-49.3	3.20E-03	1.98E-08	0.096	4.29	1.150	0.161	4.98	0.355	3.920	0.075	7.02
	-29.9	9.40E-03	1.77E-07	0.065	3.38	3.211	0.147	6.56	0.117	2.380	0.041	4.66
	-19.2	1.26E-02	5.14E-07	0.050	4.41	6.598	0.138	5.87	0.054	1.300	0.034	4.82
	-9.8	1.64E-02	1.22E-06	0.076	3.15	12.713	0.149	3.53	0.030	0.410	0.060	3.53
	0	1.99E-02	2.82E-06	0.070	3.99	21.892	0.130	3.40	0.016	0.255	0.051	3.18
	6	2.27E-02	4.31E-06	0.080	2.88	35.089	0.160	2.72	0.012	0.185	0.052	3.30
	12.4	2.03E-02	6.64E-06	0.076	3.42	46.859	0.119	1.78	0.007	0.153	0.037	2.58
	avg			*0.074*	*3.65*		*0.143*	*4.12*			*0.051*	*4.16*

5.2.4.2.   The linear driving force model

To analyze the uptake curves with the LDF model, the k_{LDF} values were first determined from the plot of $ln((q_e-q)/q_e)$ vs t. Since the adsorption process was controlled by macropore diffusion, the contribution of the micropore resistance to the overall resistance was insignificant. Accordingly, Eq. (19) was simplified to:

$$\frac{1}{k_{LDF}} = \frac{R_a}{3k_f}\frac{q_e\rho_p}{C_b} + \frac{R_a^2}{15\varepsilon_p D_a}\frac{q_e\rho_p}{C_b} \quad (28)$$

Then the film mass transfer coefficient (k_f) was estimated by the correlation for forced convection around a solid sphere as shown by Eq. (23.) And the molecular diffusivity in the Sherwood and Schmidt number was estimated by the Fuller et al. correlation as in Eq. (24).[152] The values of atomic diffusion volume for H_2O and air, $\left(\sum v\right)_A = 13.1$ and $\left(\sum v\right)_B = 19.7$, were obtained from the literature.[23] After k_{LDF} was determined from the plot of $ln((q_e-q)/q_e)$ vs. t and k_f was calculated from Eq. (23), D_a values were then estimated using Eq. (28). It is observed in **Table 5-2** that the k_{LDF} values increased with the dew point and adsorption temperature while the D_a values did not change significantly. The average AARD at the studied adsorption temperatures ranged from 2.47% to 4.12%, which indicated the good capability of the LDF model to fit the uptake curves.

5.2.4.3.   The shrinking core model

For the SC model, the parameter τ_1 was calculated by Eq. (2) with the k_f estimated from Eq. (23), and then τ_2 was determined by fitting the experimental data using the least-square fitting method. Then D_a was calculated using Eq. (6). As shown in **Table 5-2**, the values of τ_1 and τ_2 generally decreased as the dew point and temperature increased, which

means that the time needed for mass transfer through external gas film and the macropore decreased as the dew point and temperature increased. In addition, the ratios of τ_1 to τ_2 could represent the contributions of gas film mass transfer resistance and macropore diffusion resistance to the overall resistance, which are plotted in **Figure 5-6**. It was found that macropore diffusion resistance contributed 84 – 94 % to the overall mass transfer resistance for H_2O adsorption on Ag^0Z at temperatures of 25 – 200 ^oC, and the gas film resistance contributed 6 – 16%. The decrease of gas film resistance contribution with increasing temperature could be explained by the fact that the gas film mass transfer coefficient is proportional to the 1.75^{th} power of temperature ($T^{1.75}$ as in Eq. 24) while the macropore diffusivity changes linearly with the square root of temperature ($T^{0.5}$ as in the expression of Knudsen diffusivity, which dominates the gas diffusion process in macropore when the adsorbate concentration is low[132]). The decreasing gas film resistance also explains the decrease of average AARD with increasing temperature for the MD model discussed above.
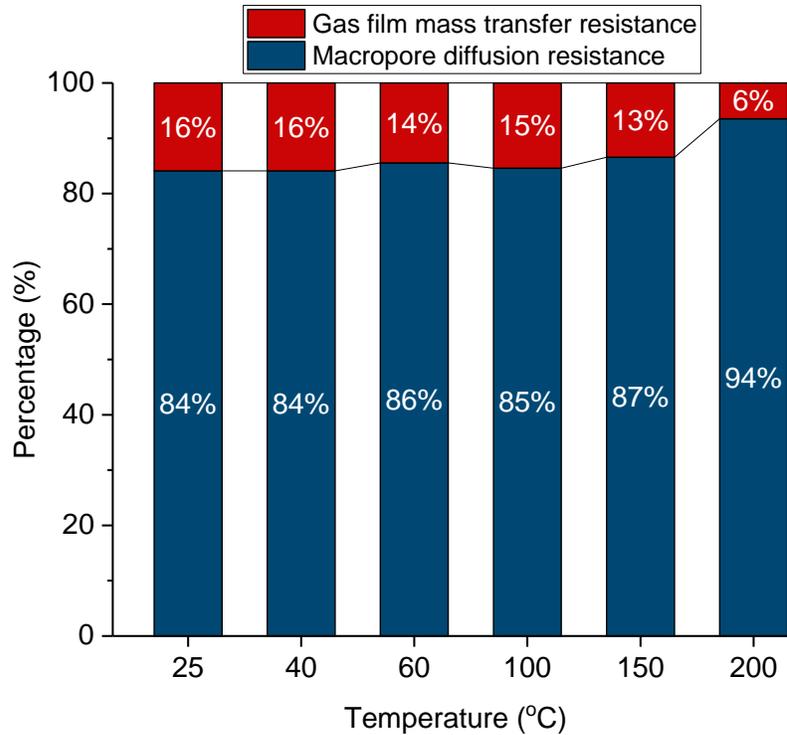
Figure 5-6. Distribution of mass transfer resistances for H_2O adsorption on 0.9 mm Ag^0Z pellets.

Table 5-3 summarizes the properties of the gas flows and parameters from the MD, LDF, and SC models at different temperatures. The data show that the calculated molecular diffusivity (D_{AB}) and the gas film mass transfer coefficient (k_f) increased as the adsorption temperature increased. The values of macropore diffusivity (D_a) obtained from the three models were in the same order of magnitude and ranged between 0.05 to 0.17 cm^2/s in the temperature range of 25 - 200°C. The overall average AARD for the MD, LDF, and SC models are 7.42%, 2.97%, and 3.27%, respectively, which indicated that the LDF and SC models could well describe the adsorption process of H_2O on Ag^0Z pellets under the studied conditions. The LDF model fits the uptake curves slightly better than the SC model. **Figure 5-7** demonstrates the goodness of three models in fitting the uptake curves of H_2O

on Ag^0Z. It can be observed that LDF and SC models fit the experimental data well under all conditions, while the MD model does not fit well at low temperatures.

Table 5-3. Properties and parameters for the MD, LDF, and SC models (P= 1 bar).

T (ºC)	Viscosity [24] (10^{-6} m²/s)	D_{AB} (cm²/s)	k_f (cm/s)	$D_{a, MD}$ (cm²/s)	AARD (%)	$D_{a, LDF}$ (cm²/s)	AARD (%)	$D_{a, SC}$ (cm²/s)	AARD (%)
25	15.62	0.253	10.91	0.107	7.42	0.139	2.79	0.091	2.66
40	17.04	0.276	11.52	0.107	7.17	0.142	2.50	0.087	2.75
60	18.94	0.308	12.34	0.111	8.27	0.156	2.47	0.094	2.89
100	23.20	0.375	14.09	0.122	5.01	0.167	2.60	0.102	3.34
150	28.40	0.468	16.22	0.101	3.89	0.169	3.36	0.092	3.87
200	34.80	0.569	18.46	0.074	3.65	0.143	4.12	0.051	4.16
avg					7.42		2.97		3.27
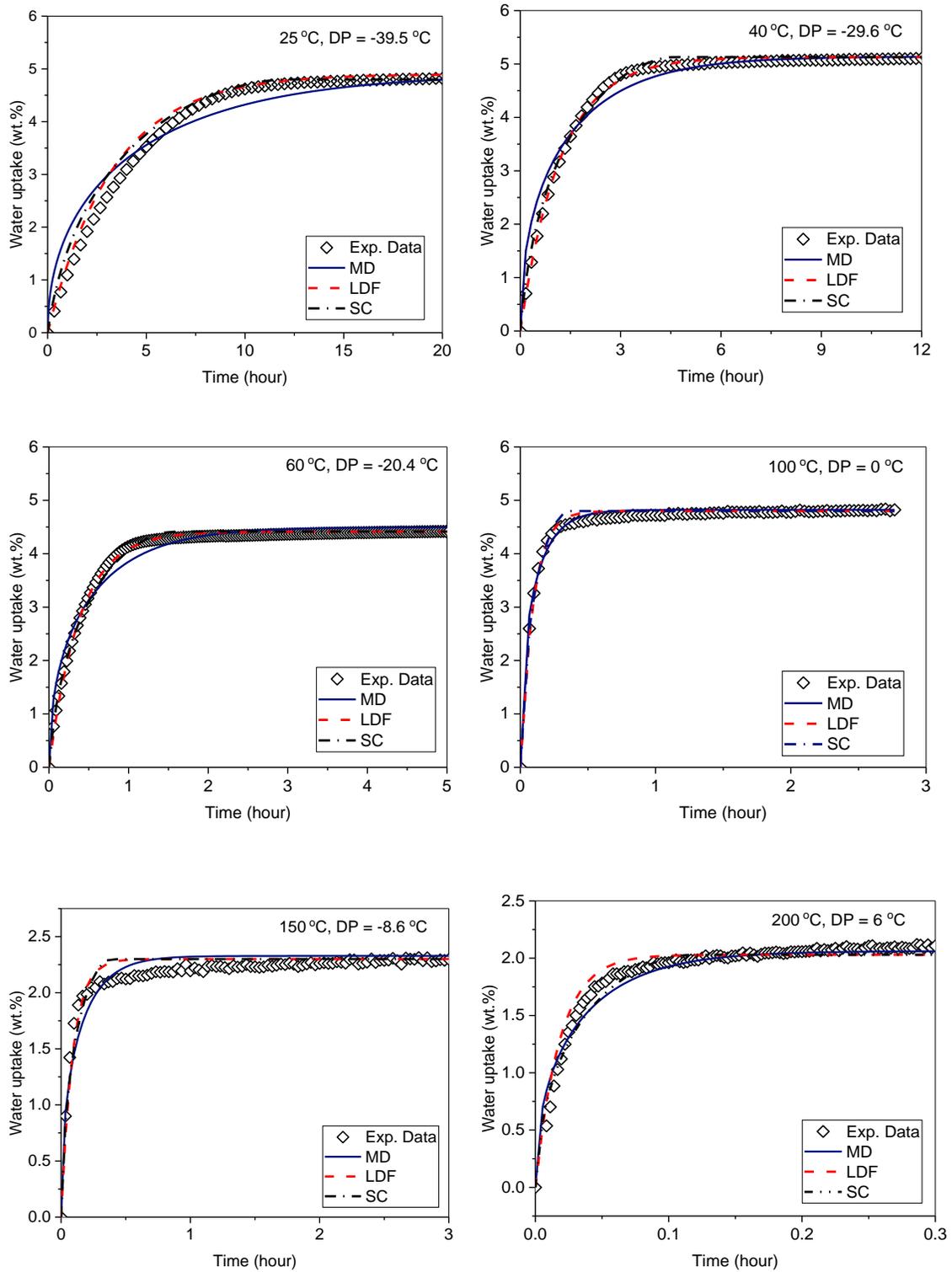
Figure 5-7. Curve-fitting of the MD, LDF and SC models to the uptake curves of H_2O on Ag⁰Z at different conditions.

The reason that the MD model has the least capability, among the three models, of fitting the uptake curves could be due to the existence of external mass transfer resistance. Since the MD model only contains a term describing the macropore diffusion, it cannot fit the initial fraction of the adsorption process well where gas film mass transfer plays a significant role. This explanation is supported by the curve fittings in **Figure 5-7** that a relatively large deviation between the MD model and experimental data is observed at the initial 20% of the uptake curves, where the model predictions are higher than the actual uptake. Also, as shown in **Figure 5-7**, the MD model tended to fit the curves better at high temperatures as the gas film mass transfer resistance became less significant.

The macropore diffusivity obtained from the MD, LDF and SC models are compared in **Figure 5-8**. Among the three models, the D_a values from the LDF model were the largest and those from the SC model were the smallest. Since the MD, LDF and SC models were derived from various physical models of adsorption, the equations of D_a in the three models were algebraically different. In addition, D_a values from the three models showed the similar change with temperature. They slightly increased as the temperature increased from 25 to 150 $^{\circ}$C and then decreased when temperature further increased to 200 $^{\circ}$C. This decrease was likely due to a physical or chemical change to the Ag^{0}Z pellets at such high temperature. However, studying the property changes to the material was not within the scope of the current paper. It would be a valuable work for the future study.
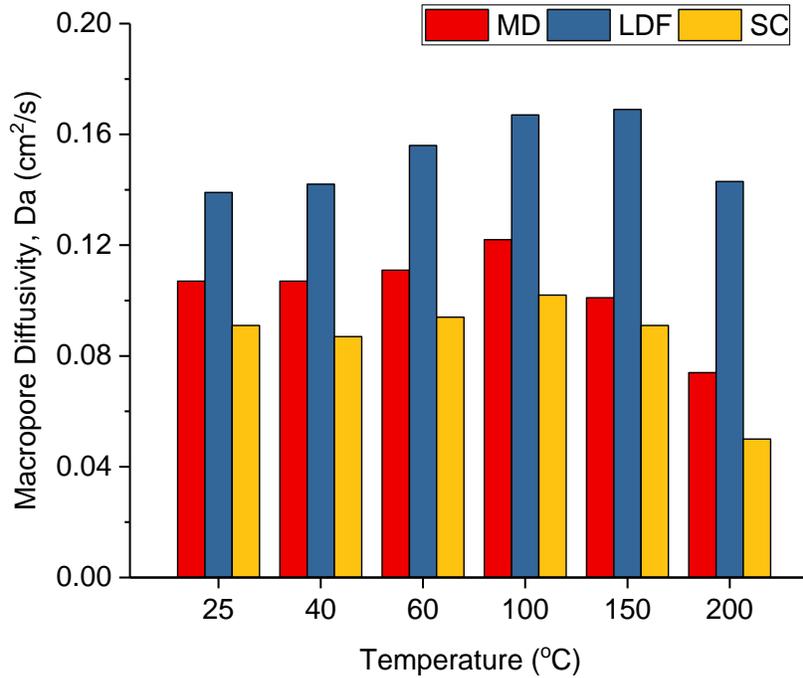
Figure 5-8. Comparison of the macropore diffusivity obtained using the MD, LDF and SC models.

5.3. Equilibrium

5.3.1. Determination of maximum monolayer capacity

Unlike the H_2O adsorption on Molecular Sieves (3A, 4A, and 5A), which is a monolayer adsorption process, H_2O adsorption on AgZ and Ag^0Z is a process including monolayer adsorption, multilayer adsorption, and pore filling according to the shape of isotherms. Multiple models are needed to describe the entire isotherm with the three different adsorption mechanisms. In this study, modeling of the isotherms was focused on the monolayer adsorption portion only. This was done because, when using Ag^0Z for capturing radioactive I_2 in off-gas streams of nuclear fuel reprocessing facilities, the

operating temperature will be maintained at about 150^oC[16, 19, 22-23, 60] (optimal temperature for I_2 adsorption) where only monolayer adsorption of H_2O will take place.

To apply models to the isotherms, the maximum monolayer adsorption capacities of the sorbents need to be determined. The Brunauer-Emmett-Teller (BET) isotherm model[118] was employed to estimate the monolayer capacities with the experimental data obtained at relative vapor pressures between 0.05 and 0.3. The linear form of the model is:

$$\frac{p}{v(p_0 - p)} = \frac{c-1}{v_m c}\left(\frac{p}{p_0}\right) + \frac{1}{v_m c} \qquad (29)$$

where p and p_0 are the equilibrium and saturation partial pressures of the adsorbate, respectively, v is the amount of gas adsorbed, v_m is the amount of gas adsorbed by monolayer adsorption and c is the BET constant.

5.3.2. H_2O adsorption isotherms and modeling

The maximum monolayer capacity of H_2O adsorption on Ag^0Z was determined using the BET isotherm model to describe data obtained at 25^oC. Experimental data, as well as the optimized BET model, are shown in **Figure 5-9**. The data indicated that the isotherm of H_2O adsorption on Ag^0Z was a type IV isotherm according to the IUPAC classification of adsorption isotherms,[157] which includes monolayer adsorption, multilayer adsorption, and pore filling processes. The maximum H_2O adsorption capacity of Ag^0Z at relative pressure over 0.7 was found to be more than 20 wt.%, which was achieved by pore filling. As shown in **Figure 5-9**, the BET model was able to fit the data at relative pressures

between 0.05-0.3. The maximum monolayer capacity was estimated to be 8.56 wt.%, which was determined by the plot of $p/[v(p_0-p)]$ vs. p/p_0 shown in **Figure 5-10**.
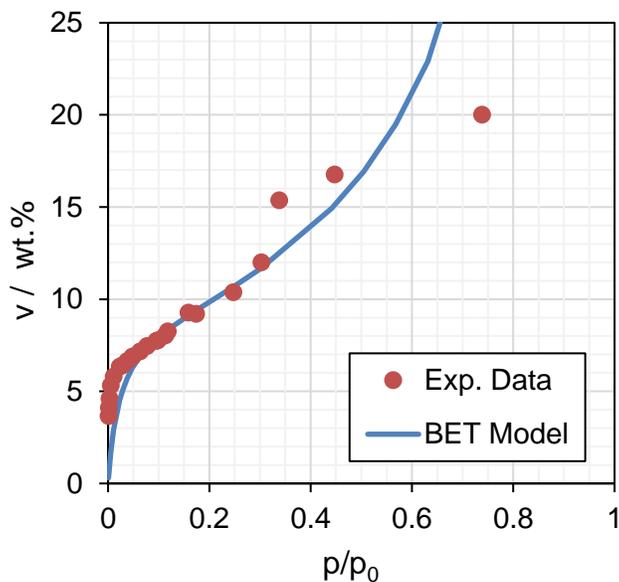
Figure 5-9. Comparison of BET model with the isotherm of H_2O adsorption on Ag^0Z obtained at 25 °C.
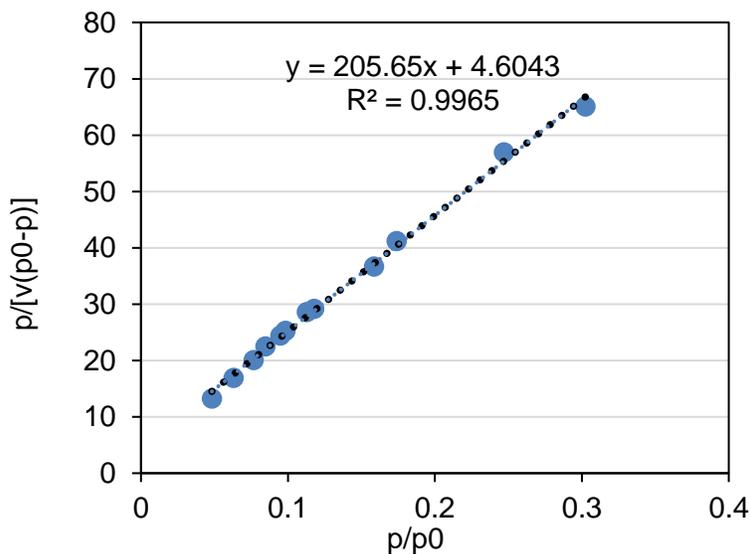
Figure 5-10. The plot of $p/[v(p_0-p)]$ vs. p/p_0 using the H_2O adsorption data on Ag^0Z obtained at 25°C and relative pressures between 0.05-0.3.

The isotherms for H_2O adsorption on Ag^0Z at 25, 40, 60, 100, 150, and 200 $^\circ$C are shown in **Figure 5-11.** Both the Heterogeneous Langmuir model and the GSTA model were used to describe the data. Each model was capable of describing the isotherms and found that the number of adsorption sites (m) is equal to 3. This suggests that there were three energetically distinguished adsorption sites in the adsorbent for adsorption of H_2O.

The adsorption capacity of each adsorption site ($q_{max,n}$) and thermodynamic parameters (ΔH_n and ΔS_n) obtained from both models are compared in **Table 5-4**. Different adsorption capacities ($q_{max,n}$) for the three adsorption sites were obtained from the Heterogeneous Langmuir model, while the capacity for the sites obtained from the GSTA model was just one-third of the overall capacity. The ΔH_n and ΔS_n for H_2O adsorption on each site were obtained by correlating the equilibrium constants (K_n) with temperature (T) using the Van't Hoff equation, and all the correlations had a correlation coefficient (R^2) above 0.99. Notice that the two models provided different sets of ΔH_n and ΔS_n values for the adsorption sites. It should be noted that the ΔH_n and ΔS_n values for the GSTA model are not associated with site-specific energies as in the Heterogeneous Langmuir model, but are instead representative of the event energies of the adsorption of n molecules in the site network of the adsorbent.[145] Therefore, the ΔH_n and ΔS_n values for the two models are not directly comparable.
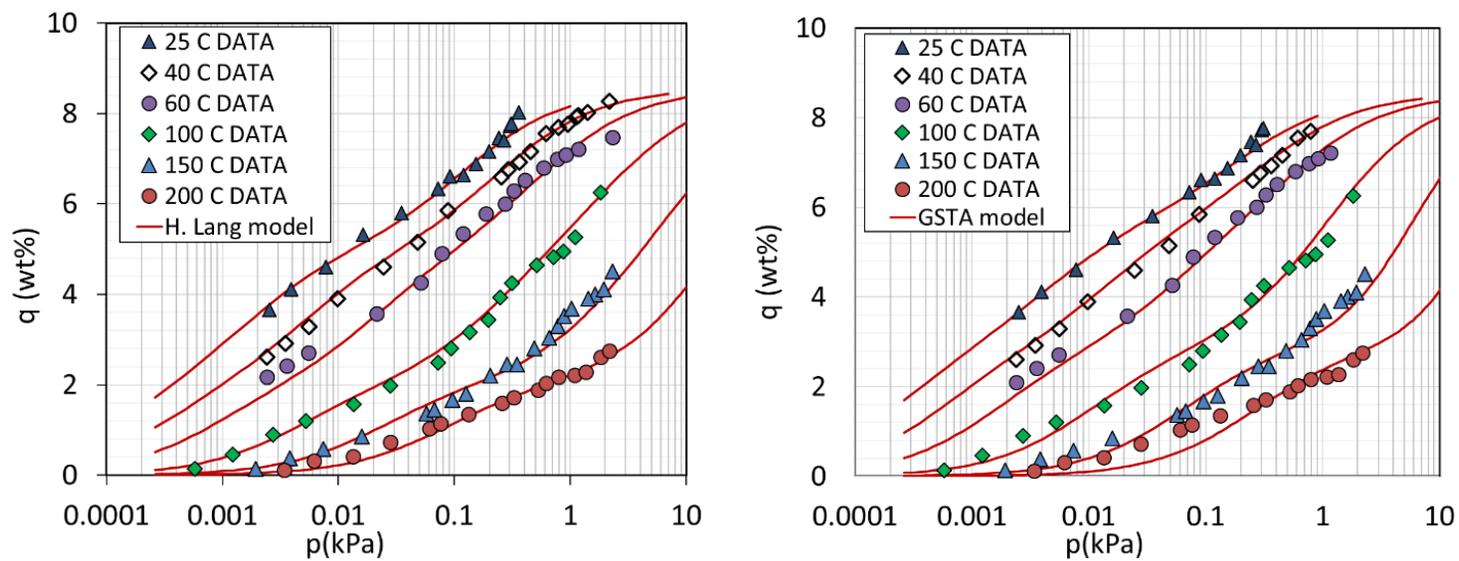
Figure 5-11. Isotherms of H_2O adsorption on Ag^0Z obtained at 25, 40, 60, 100, 150, and 200 ^{o}C and fitted by the Heterogeneous Langmuir (left) and GSTA (right) models.

Table 5-4. Parameters obtained from the Heterogeneous Langmuir model and the GSTA model

n	Heterogeneous Langmuir model				GSTA model			
	$q_{max,n}$ (wt.%)	$\Delta H_{L,n}$ kJ/mol	$\Delta S_{L,n}$ J/K/mol	R^2	$q_{max,n}$ (wt.%)	$\Delta H_{G,n}$ kJ/mol	$\Delta S_{G,n}$ J/K/mol	R^2
1	3.53	-36.91	-68.19	0.995	2.85	-47.39	-50.44	0.993
2	2.97	-60.02	-110.43	0.993	2.85	-106.39	-165.59	0.996
3	2.06	-42.66	-31.31	0.990	2.85	-135.64	-212.03	0.998

The goodness of fit of the models to the isotherms was estimated by the average absolute relative deviation (AARD) shown in Eq. (25). The estimated average values of AARD the Heterogeneous Langmuir model and GSTA model were 3.36 and 4.83, respectively, indicating that both models are capable of describing the isotherms of H_2O adsorption on Ag^0Z. It is noted that although the Heterogeneous Langmuir model fitted the isotherms slightly better than the GSTA model, the Heterogeneous Langmuir process of optimizing the model parameters was much more complicated than that of the GSTA model and the complication increases significantly if heterogeneity of adsorption systems increases. For those adsorption systems that are more complex or adsorption systems including co-adsorption of multiple components, the GSTA model may be more favorable since it can provide reliable modeling results with a relatively simpler analysis process.

5.3.3. Comparison of Ag^0Z and AgZ

It was found from the N_2 physisorption analysis that the surface area and pore volume of the AgZ changed significantly after reduction in H_2 at 400 °C for 24 hr, while

these properties did not change when treated in N_2 at the same conditions (**Table 5-5**). This result indicates that there were no thermal effects on the mordenite structure at 400 ^{o}C and the changes to properties should be due to the presence of H_2. The XRD patterns of AgZ and Ag^0Z in **Figure 4-5** also showed that the structure of mordenite did not change during the reduction. It is also noted in **Table 5-5**, that the micropore surface area and micropore volume increased significantly when treated with H_2, while the external surface area and meso/macropore volume did not change. This is expected to be a result of the migration of Ag^+ in the micropores of AgZ to the meso/macropores, forming Ag clusters on the surface of the mordenite crystals during H_2 reduction, as previously observed and reported.[88, 103, 158] This was also observed in the XRD pattern of Ag^0Z in **Figure 4-5** which had two sharp peaks of Ag^0, indicating the existing of Ag crystals (nanoparticles) on the surface of mordenite. When the AgZ was reduced to Ag^0Z, Ag^+ in the micropores of AgZ was replaced by H^+ and migrated to the meso/macropores. Therefore, the Ag^0Z was essentially $(Ag^0)HZ$. Since H^+ has a smaller atomic diameter than Ag^+, when performing N_2 physisorption analyses, N_2 molecules were able to enter the micropores of Ag^0Z, resulting in a much larger micropore surface area and volume.

Table 5-5. Physical properties of AgZ, Ag^0Z, and AgZ treated in N_2.

Properties	AgZ	Ag^0Z	AgZ Treated in N_2 (400 ^{o}C, 24 hr)
BET surface area (m^2/g)	27.75	176.60	28.15
Micropore surface area (m^2/g)	6.66	154.43	6.56
External surface area (m^2/g)	21.09	22.16	21.58
Micropore volume (μL/g)	3.05	77.03	3.06
Mesopore and macropore volume (μL/g)	95.59	94.96	97.69

The isotherms for H_2O adsorption on the unreduced AgZ were obtained at 25, 40, and 60 ^{o}C and are compared with the isotherms for Ag^0Z in **Figure 5-12.** It was found that the adsorption equilibrium capacities of AgZ at the same H_2O vapor pressure and temperature were lower than those of Ag^0Z. The maximum monolayer adsorption capacity for AgZ was estimated at 8.22 wt.% using the BET model described above, which was lower than that of Ag^0Z (8.56 wt.%). The lower H_2O adsorption capacity suggested a weaker affinity of H_2O to the Ag^+ sites than for the H^+ sites.

The isotherms of AgZ were also analyzed with the GSTA model and model parameters were compared with those for Ag^0Z. The plot in **Figure 5-13** shows an excellent agreement between the GSTA model and the isotherms of AgZ (average AARD = 3.1), indicating the capability of the model to describe a different system. The optimal number of adsorption sites (m) on the AgZ for adsorbing H_2O was also found to be 3, which was

the same as Ag^0Z. The ΔH_n and ΔS_n values obtained are compared with those for Ag^0Z in

Table 5-6, the results of which were obtained from the data shown in **Figure 5-13**. As

expected, the magnitudes of ΔH_n and ΔS_n for H_2O adsorption on these sites were smaller

than those in Ag^0Z. In general, a higher magnitude of the ΔH_n and ΔS_n indicates a stronger

interaction between the adsorbate and the adsorption sites. Therefore, the bonding of the

H_2O molecules to the H+ in Ag^0Z is stronger than the bonding to the Ag+ in AgZ.
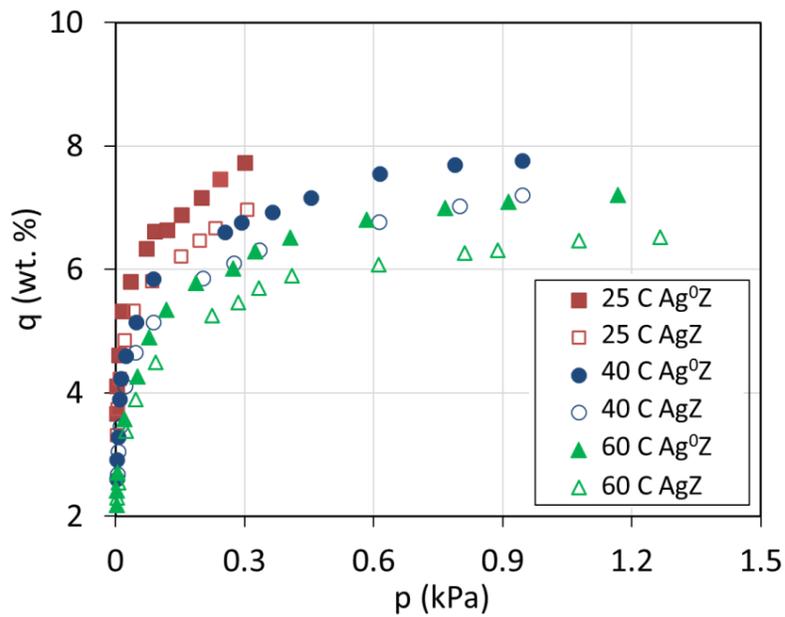
Figure 5-12. Isotherms of H_2O adsorption on AgZ and Ag^0Z.
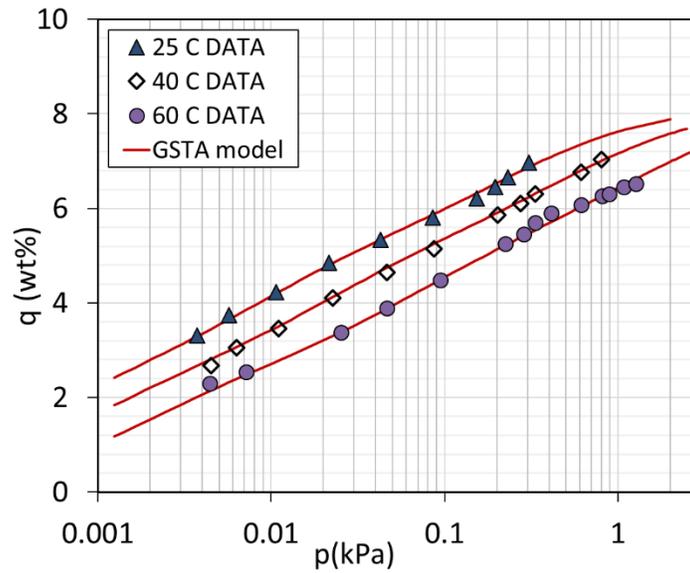
Figure 5-13. Fitting of GSTA model to the isotherms for AgZ.

Table 5-6. Parameters of Heterogeneous Langmuir model and GSTA model

n	Ag⁰Z			AgZ		
	$q_{max,n}$ (wt.%)	ΔH_n kJ/mol	ΔS_n J/K/mol	$q_{max,n}$ (wt.%)	ΔH_n kJ/mol	ΔS_n J/K/mol
1	2.85	-47.39	-50.44	2.74	-36.27	-17.79
2	2.85	-106.39	-165.59	2.74	-80.68	-89.85
3	2.85	-135.64	-212.03	2.74	-121.05	-176.16

5.4. Conclusions

Kinetic data of H_2O vapor adsorption on Ag^0Z pellets were obtained with a continuous-flow adsorption system at temperatures of 25 – 200°C and dew points from -53.6 to 12.1 °C. The data of high precision obtained at a wide range of conditions shorten the data gap in the literature for H_2O adsorption on Ag^0Z. Through adsorption experiments with Ag^0Z pellets of various radii and analysis with pore diffusion models, it was found that the diffusion process of H_2O vapor into Ag^0Z pellets was controlled by macropore diffusion, and the adsorption process on the 0.9 mm Ag^0Z pellets was controlled by both macropore diffusion and gas film mass transfer. The LDF and SC models were able to fit the kinetic data well with an average AARD of 2.97% and 3.27%, respectively. The MD model could describe the uptake curves of the H_2O adsorption on Ag^0Z reasonably well at high temperatures where the external gas film mass transfer resistance becomes insignificant.

The macropore diffusivity for H_2O adsorption on Ag^0Z was determined by the three models which ranged between 0.05 to 0.17 cm^2/s at the studied temperatures. The D_a values generally increased with increasing temperature from 25 to 150 ^{0}C followed by a decrease when temperature increased further from 150 to 200 °C. The decrease was probably due to changes to the adsorbent properties at high temperature, which will be investigated in future work. The experimental data and model parameters determined for the kinetics of H_2O vapor adsorption on Ag^0Z provide valuable information for the design-of adsorption systems for the treatment of off-gases from spent nuclear fuel reprocessing facilities.

The isotherms of H_2O adsorption on Ag^0Z and AgZ were obtained at various temperatures in this study. Data for Ag^0Z were analyzed with the Heterogeneous Langmuir

model and the GSTA model and were well described by both models. The results from both models indicate that there were three distinct energetic adsorption sites in AgZ and Ag^0Z for adsorbing H_2O vapor. Enthalpies and entropies for the adsorption site models were obtained to describe the adsorption of H_2O on Ag^0Z. The fitness of the Heterogeneous Langmuir model to the isotherms was slightly better than the GSTA model but required a more complicated optimization process. Selection between the Heterogeneous Langmuir model and the GSTA model should be made based on the complexity of the system to be described.

Significant changes to the micropore surface area and volume were found when reducing the AgZ to Ag^0Z in H_2 at 400 °C. By investigating the physical properties of Ag^0Z, AgZ, and AgZ treated in N_2 at 400 °C, it was found that the changes in micropore surface area and volume was due to the reduction of Ag^+ to Ag^0 rather than thermal effects. This is consistent with previous studies on the migration of Ag^+ to the mordenite surfaces during the reduction of AgZ.[103, 158] Furthermore, the equilibrium adsorption capacities of AgZ were found lower than those of Ag^0Z at the same conditions due to a weaker interaction of H_2O molecules with the Ag^+ sites in AgZ than with the H^+ sites in Ag^0Z. This conclusion was supported by comparison of the model parameters whereby enthalpies and entropies of H_2O adsorption on AgZ were lower than those on Ag^0Z.

The results of this study reduce the data gap in the literature and provide insights of equilibrium adsorption of H_2O on silver mordenites. The experimental observations and fundamental modeling results have important implication in system design when using silver mordenite for off-gas treatment and can support the modeling efforts by the U.S.

Department of Energy (DOE), Fuel Cycle Research and Development (FCR&D) for off-gas treatment processes.

Chapter 6. I_2 /H_2O Co-adsorption

6.1. Introduction

In this chapter, the adsorption of I_2 on Ag^0Z with the presence of H_2O vapor was discussed. As demonstrated in Chapter 5, Ag^0Z can co-adsorb significant amount of H_2O vapor from the gas streams. The presence of H_2O vapor impacts the adsorption performance of Ag^0Z for I_2 adsorption. Although methods to reduce or to prevent co-contamination of the tritiated H_2O may have to be designed, it would be valuable to understand the impact of H_2O vapor on the performance of Ag^0Z in terms of capacity changes and mechanism for the changes.

To determine the performance of Ag^0Z for co-adsorbing I_2 and H_2O, experiments were conducted at different I_2 and H_2O concentrations. Both co-adsorption kinetic and equilibrium data were obtained to discuss the performance changes. The co-adsorption results were compared with the single component adsorption data.

Mechanisms for the co-adsorption process were studied through experiments with different adsorption sequences of I_2 and H_2O, as well as chemical and physical analyses of the adsorbents before and after the adsorption. The co-adsorption was found to be a complicated process including adsorption of I_2 by the silver particles, adsorption of H_2O in the micropore of Ag^0Z, as well as deactivation of the silver for I_2 adsorption.

6.2. Co-adsorption Uptake Curves

Results of I_2 and H_2O co-adsorption on Ag^0Z are shown in **Figure 6-1**. The adsorption and desorption curves were obtained at 150°C with humid gas streams of dew point -16 °C and different I_2 concentrations. I_2 and H_2O were adsorbed simultaneously

during the uptake region and then desorbed in sequence. The total weight gain ranged from 9.4 to 11.2 wt.%. According to the H_2O adsorption data in Chapter 5, the equilibrium H_2O adsorption capacity at -16 °C is about 1.8 wt.%, which means the total I_2 uptake in **Figure 6-1** is approximately 7.6 - 9.4 wt.%. This is significantly lower than that with dry air under the same conditions. The H_2O desorption curve indicated that about 1.3 wt. % of H_2O was desorbed from the Ag^0Z pellets when H_2O vapor was removed from the gas stream. There was ~0.5 wt% remained in the adsorbent. The subsequent desorption of I_2 shows the similar trend as in dry air streams, indicating that the amount of physisorbed I_2 in the humid stream had no significant difference to that in dry air.

Additionally, from the initial fraction of uptake curves in **Figure 6-1**, it can be noted that H_2O was adsorbed more rapidly compared to I_2. The uptake curves reached a weight gain of about 2 wt.% in a very short time due to H_2O adsorption. A transient point can be observed at about 2 wt.%, where H_2O adsorption reached equilibrium and I_2 adsorption mainly took place. This observation agreed with well with the H_2O and I_2 adsorption kinetics discussed in Chapter 4 and 5.

A comparison of the I_2 adsorption isotherms (chemisorbed) in dry air and humid air is shown in **Figure 6-2**. About 40% of average equilibrium chemisorption capacity drop was observed when I2 was co-adsorbed with H_2O at DP of -16 °C. Therefore, the presence of H_2O in the gas stream had significant adverse impacts on the I_2 adsorption capacity of Ag^0Z. In addition, the two curves had the same tendency of increase as the I_2 concentration increased. The increase of I_2 concentration from 10 to 50 ppmv was insignificant, comparing to H_2O concentration (1490 ppm), to make I_2 more competitive for occupying the adsorption sites.
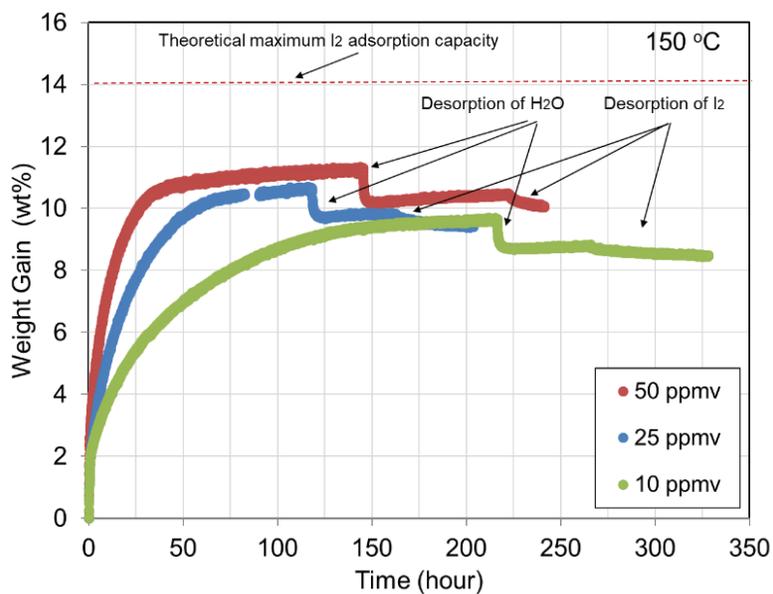
Figure 6-1. Co-adsorption of I_2 and H_2O on Ag^0Z followed by desorption of H_2O and I_2.
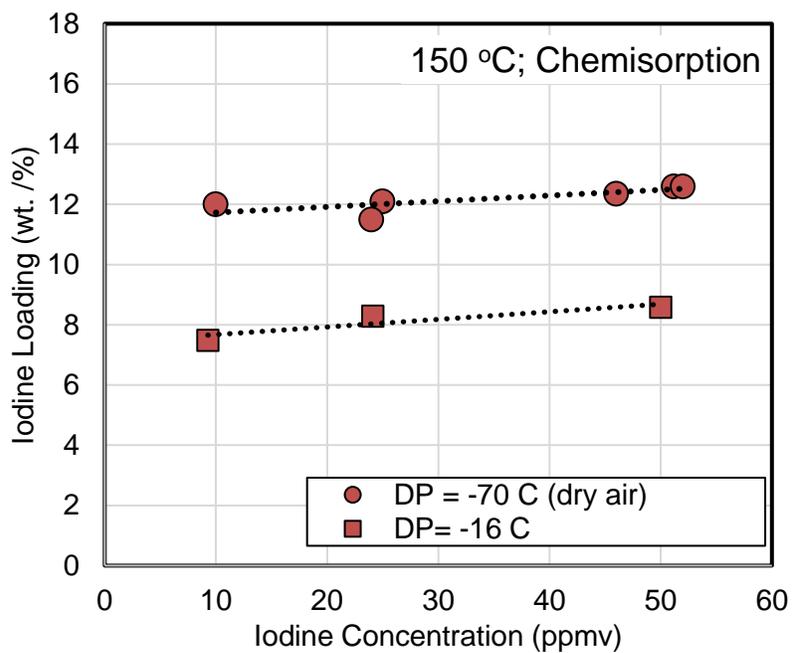
Figure 6-2. Isotherms chemisorption of I_2 on AgZ in the dry and humid air.

The effect of H_2O concentration on the adsorption capacity of AgZ was investigated with humid gas streams of various dew points: -23 and 0.6 $^{\circ}$C. **Figure 6-3** shows that the I_2 loading amount (chemisorbed) decreased with the increasing dew point of the gas streams, indicating that higher H_2O concentration resulted in a more significant loss of I_2 adsorption sites. However, the reduction of capacity does not change linearly with the H_2O vapor concentration in the gas stream, as demonstrated by the plot in **Figure 6-3b**. The I_2 loading dropped rapidly within 1500 ppmv, and decrease slowly beyond 1500 ppmv.
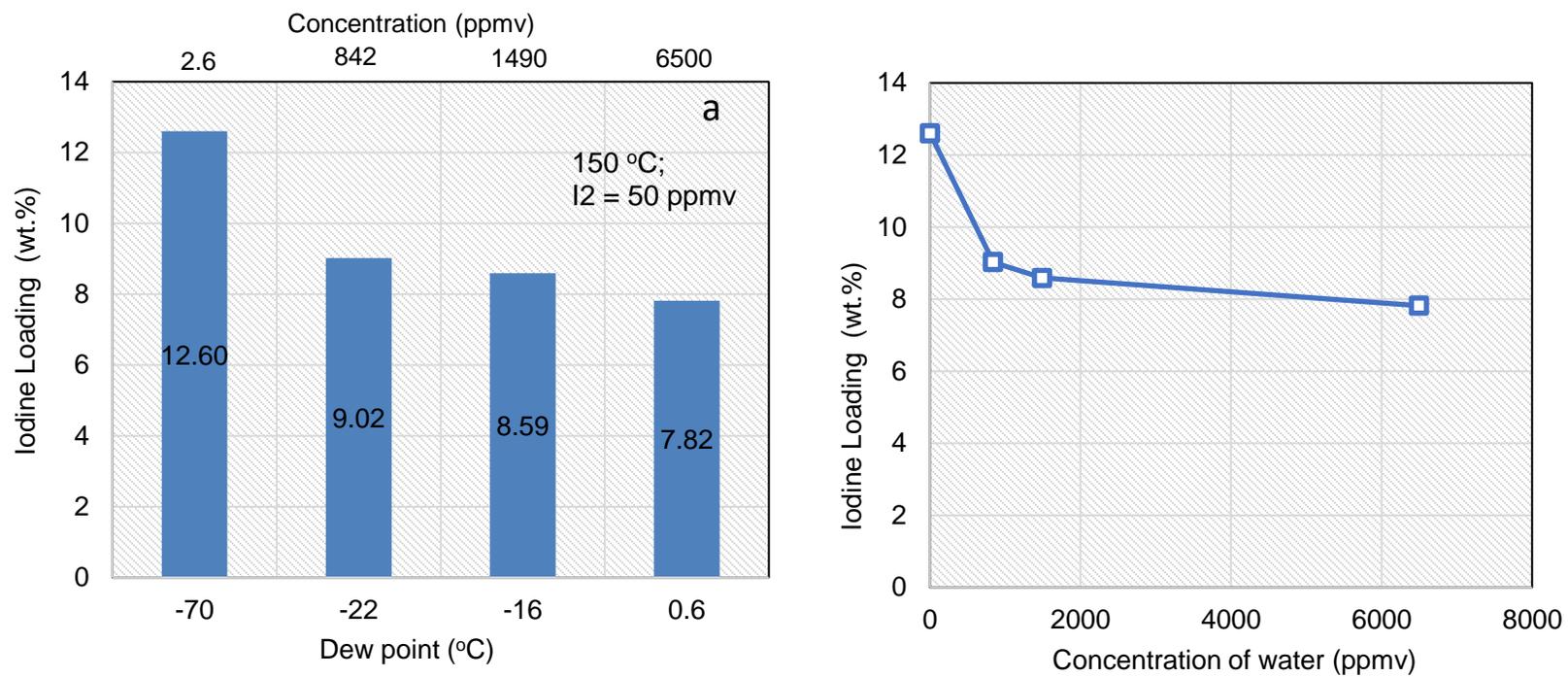
Figure 6-3. I$_2$ adsorption capacity (chemisorption) of Ag^{0}Z in humid air streams of different dew points. I$_2$ was co-adsorbed with H$_2$O.

According to the mechanism of H_2O adsorption on mordenites reported in previous studies and the results of I_2 adsorption in Chapter 4 of this report, H_2O and I_2 were adsorbed at different locations in Ag^0Z. H_2O should be adsorbed to the adsorbing sites in the micropore/channels of the mordenite crystals, while I_2 was adsorbed by reacting with Ag particles on the surface of mordenite crystals. This means the reduction of I_2 adsorption capacity in humid air stream should not be due to the pore-blocking by H_2O molecules, but the deactivation of Ag particles.

To further understand the impact of H_2O on the I_2 capacity of Ag^0Z, adsorption experiments of different I_2 and H_2O uptake sequences were performed and compared. **Figure 6-4a** and **6-4b** are the uptake curve of I_2 in dry air and co-adsorption of I_2 and H_2O in the humid air of DP -16 ^oC, respectively. **Figure 6-4c** shows the adsorption of H_2O and I_2 in sequence followed by H_2O and I_2 desorption in sequence. It was noted that when H_2O was desorbed from the Ag^0Z, the curve maintained at ~9.2 wt.% and no significant I_2 adsorption occurred. The slight increase in uptake curves should be due to the physisorption of I_2, as the similar increase was observed on other I_2 uptake curves at equilibrium. That is, when H_2O molecules were removed from the micropore/channels, no further uptake of I_2 by Ag particles occurred. This indicated that a) H_2O did not block the pores/channels, b) a portion of the Ag was deactivated with the presence of H_2O in the gas stream. This conclusion is supported by results in **Figure 6-4d.** When most of the H_2O was desorbed, the I_2 capacity was still lower than that in the dry air stream. The portion of H_2O remained in Ag^0Z may be strongly binded (physically) to the adsorption sites in the pore/channel, or chemically attached to Ag through the deactivation reaction. Accordingly,

a possible reason for the effect of H_2O on the I_2 adsorption performance of Ag^0Z is the deactivated the Ag particle by H_2O.
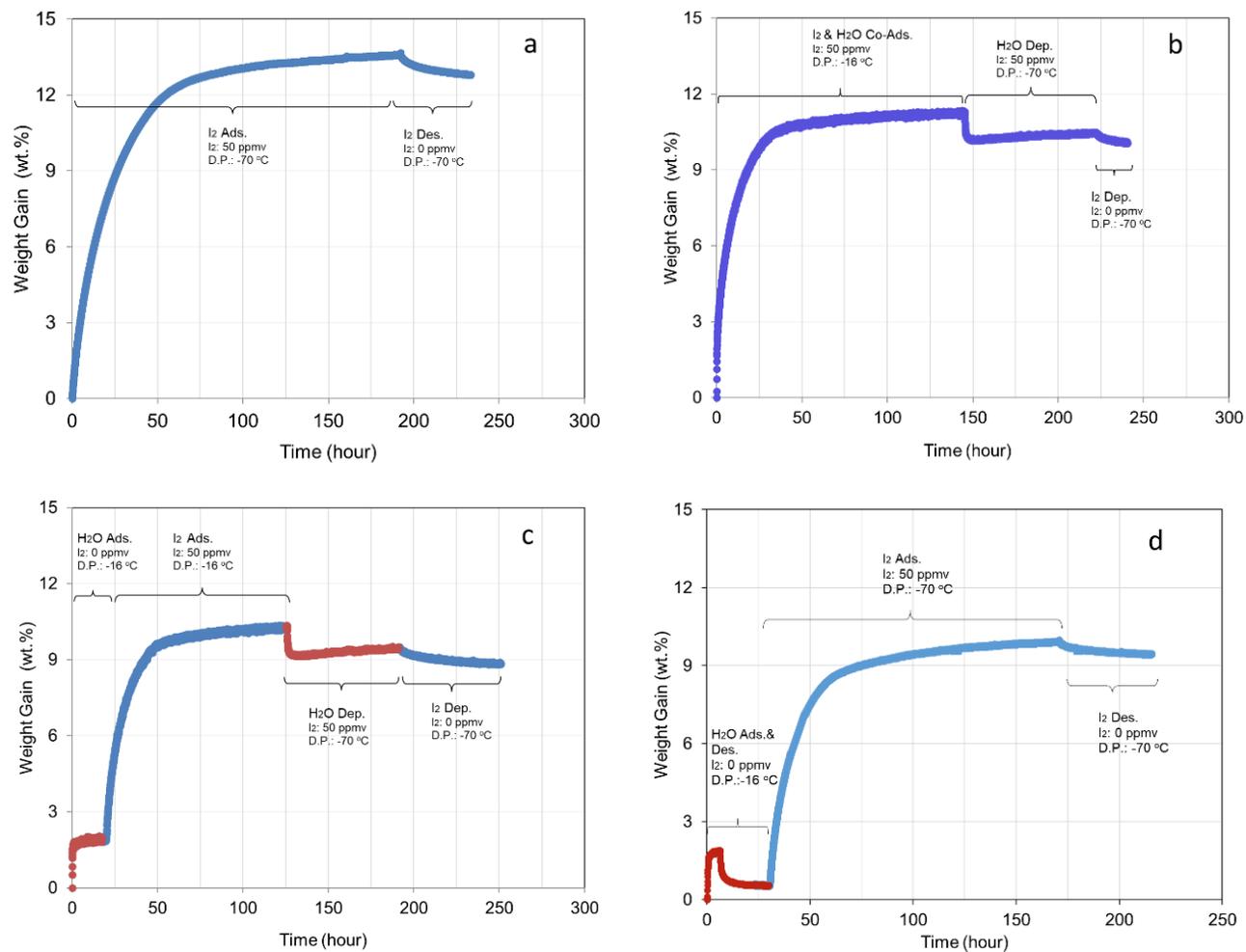
Figure 6-4. Adsorption and desorption of I_2 and/or H_2O in different sequences. a) I_2 adsorption followed by desorption. b) I_2/H_2O co-adsorption followed by H_2O desorption and then I_2 desorption. c) H_2O adsorption and then I_2 adsorption followed by H_2O desorption and then I_2 desorption. d) H_2O adsorption and then desorption followed by I_2 adsorption and then desorption.

6.3. Deactivation of Ag^0Z in Humid Air Streams

To understand the effect of water on the adsorption capacity of Ag^0Z for iodine adsorption, chemical analyses including XRD, XPS, Raman, and XAFS were conducted. Chemical changes to the Ag^0Z treated in humid air flows at different conditions were determined. The effect of water concentration (dew point: -22 to 15.3 ^oC) and treating time (6 to 72 hr) at the temperature of 150 ^oC were studied. In addition, regeneration of the humid air treated Ag^0Z was also investigated.

The Ag^0Z samples were first analyzed with XRD. The patterns in **Figure 6-5** showed a reduction of Ag^0 when the Ag^0Z were treated in humid air flows. This indicates that a portion of the Ag^0 particles was oxidized to Ag^+. However, no new characteristic peaks for Ag oxides were observed on the XRD pattern of the treated samples. This could be due to the detection limit of XRD, by which only crystals and element over 1wt% are generally detectable. In other words, the produced Ag oxides may be amorphous or not on surfaces of Ag^0Z. In addition, no significant difference in the intensity of Ag^0 peaks were observed for the Ag^0Z treated with dew point from -22 to 15.3 ^oC, indicating the oxidation reaction reached an equilibrium at a dew point lower than -22^oC.
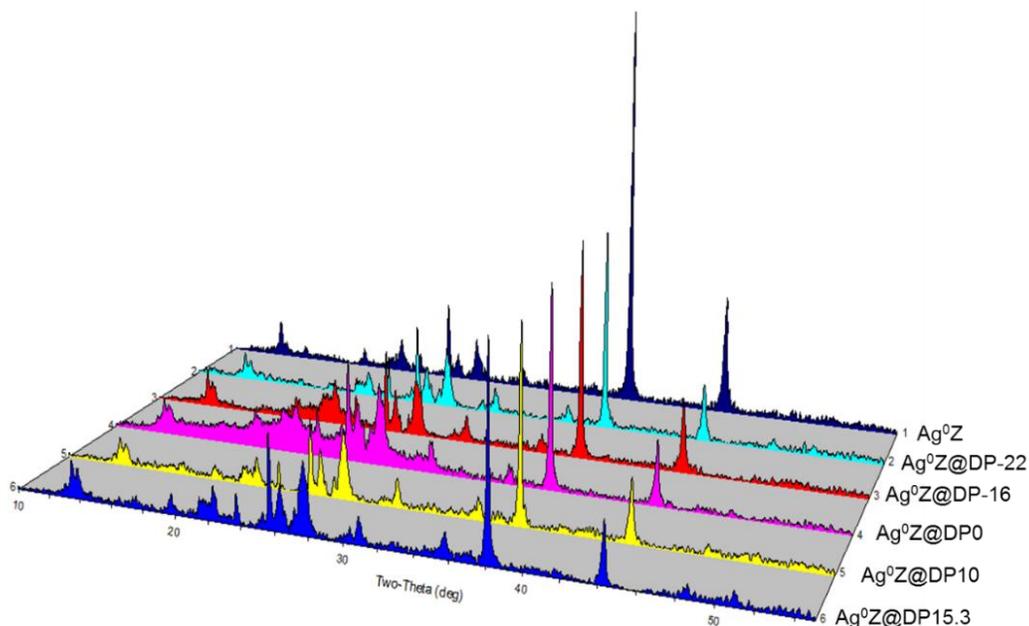
Figure 6-5. XRD patterns of Ag^0Z and Ag^0Z treated in humid air flows of different dew points for 24 hr at 150 $^{\circ}$C

The effect of treating time is shown in **Figure 6-6**, in which a decrease in Ag^0 peaks was observed when the treating time increased from 6 to 24 hr, while there was no further decrease when the treating time was extended to 72 hr. This suggests that at the studied conditions the deactivation process reached equilibrium within 24 hr. The results indicate that the deactivation process with water under real off-gas conditions is likely faster in comparison to the iodine adsorption process. The XRD patterns shown in **Figure 6-7** suggest that the deactivated (oxidized) Ag can be fully regenerated to Ag^0 particles at the same reduction conditions for Ag^0Z (4% H_2 in Argon, 400°C, 24 hr). The regenerated Ag^0Z had a similar pattern as the untreated Ag^0Z.
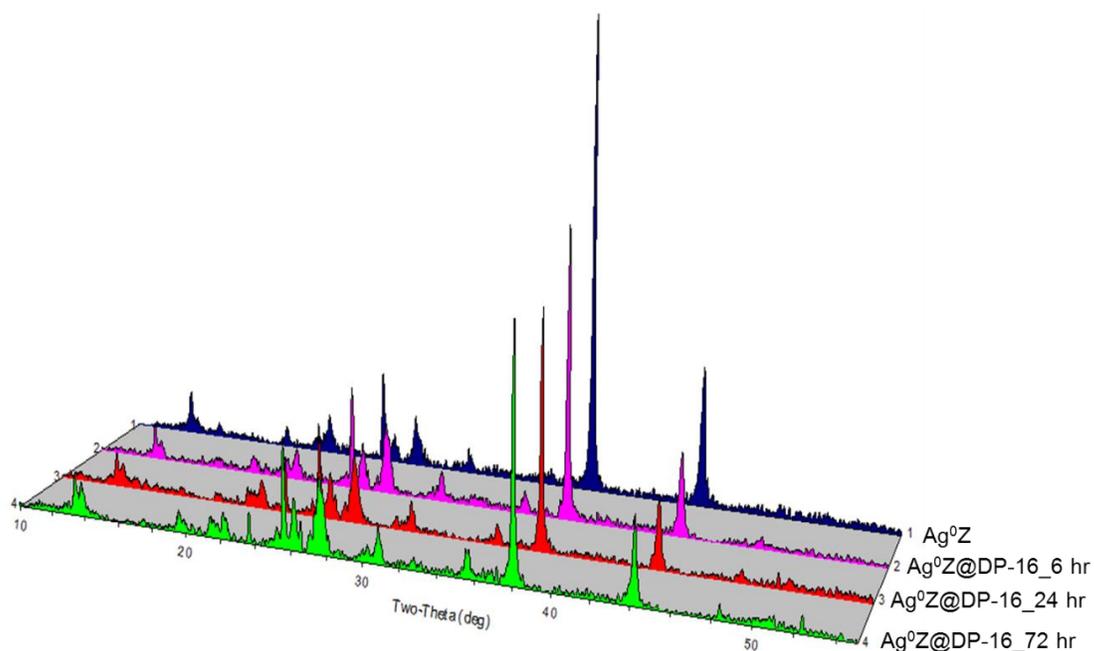
Figure 6-6. XRD patterns of Ag^0Z and Ag^0Z treated in the humid air flow of dew points - 16 °C for different periods at 150 °C.
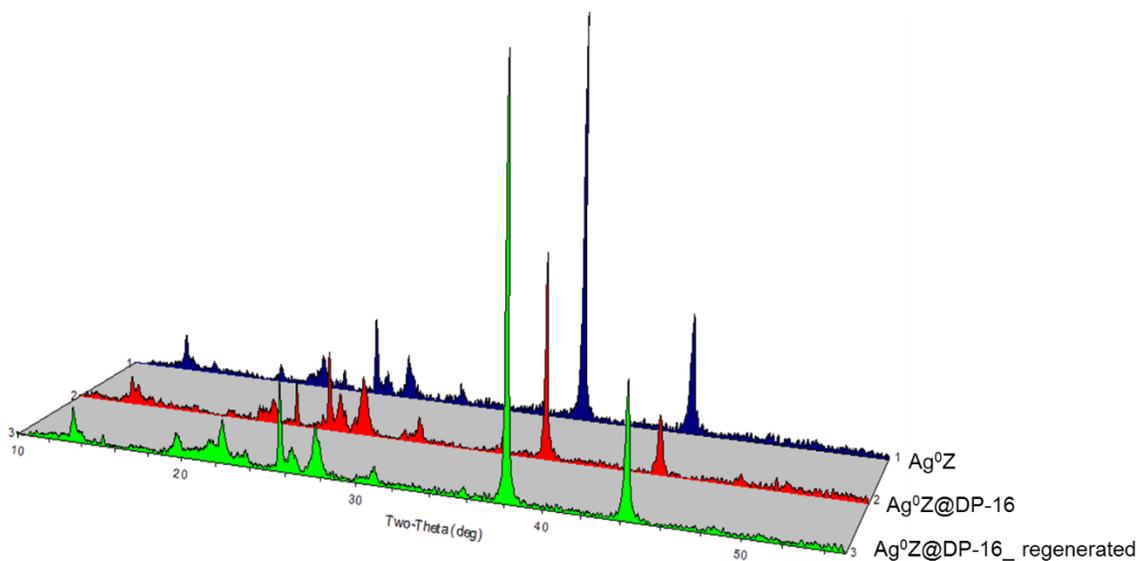
Figure 6-7. XRD patterns of Ag^0Z, Ag^0Z treated in the humid air flow of dew points -16 °C for 24 hr at 150 °C and consequently regenerated Ag^0Z.

The samples were also analyzed with Raman spectroscopy, which does not have the detection limit for non-crystals as the XRD. Therefore, any amorphous Ag oxides formed on the surface can be probed by Raman. The Raman spectra of the same samples as tested in XRD are shown **Figure 6-8**, **6-9** and **6-10**. As expected, the Ag in the unreduced AgZ ($250cm^{-1}$) can be detected as shown in the figures, which was not shown on the XRD pattern of AgZ. The intensity of Ag on AgZ was found lower than on Ag^0Z. This should be a result of migration of Ag to the surface during the reduction process, resulting in a higher Ag composition on the surface of Ag^0Z.

Results of Raman spectra agreed well with the XRD results. Similar decreases in Ag peaks were observed after treating in the humid air of different dew points and different periods. **Figure 6-8** shows a general slight reduction in Ag peaks as the dew point increased, except for DP0 and DP10 samples. This inconsistency may be due to a deviation of Ag content between the AgZ pellets resulted from the manufacturing process. Nevertheless, the decrease is insignificant, which is consistent with observations from XRD patterns. Furthermore, no new peaks of Ag oxides were observed on spectra of Ag^0Z treated in humid air, indicating that no amorphous Ag oxides were formed on the surface of Ag^0Z. According, the decrease of surface Ag content was likely due to a migration of Ag back into the mordenite crystal. This assumption is supported by the inset plot in **Figure 6-8**, where the intensity of peak (1) decreases more rapidly than peak (2) resulting in a peak shape similar to AgZ, which has Ag^+ inside the micropores/channels.

The decrease of Ag peaks in **Figure 6-9** is also consistent with the XRD patterns in **Figure 6-6**. The 6 hr treated Ag^0Z has higher intensity for Ag than the 24 hr and 72 hr treated Ag^0Z, and the latter two samples have the same intensity for Ag. This result

confirms the conclusion that the deactivation reaction of Ag^0Z in the humid air flow of dew point -16 ^oC at a temperature of 150^oC reaches equilibrium within 24 hr. The Raman spectrum of the regenerated Ag^0Z shown in **Figure 6-10** is close to the untreated Ag^0Z, which also indicates that the deactivated Ag can be re-reduced to Ag particles back on the surface.
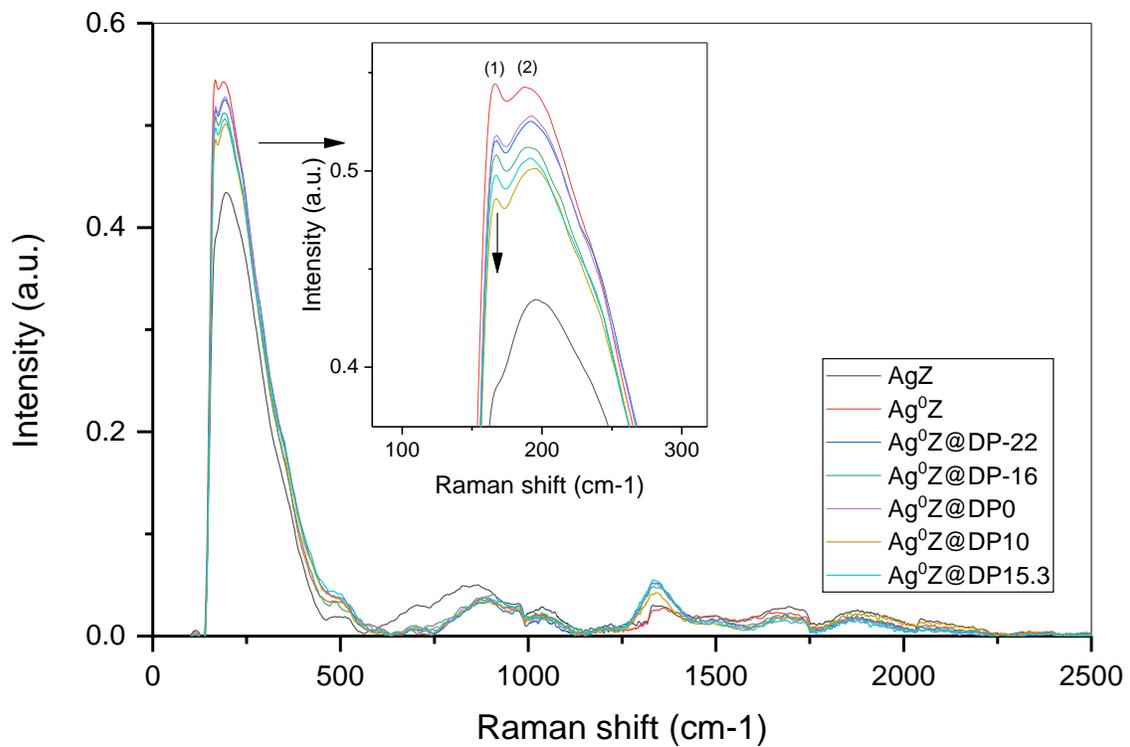
Figure 6-8. Raman spectra of Ag^0Z in Figure 6-5
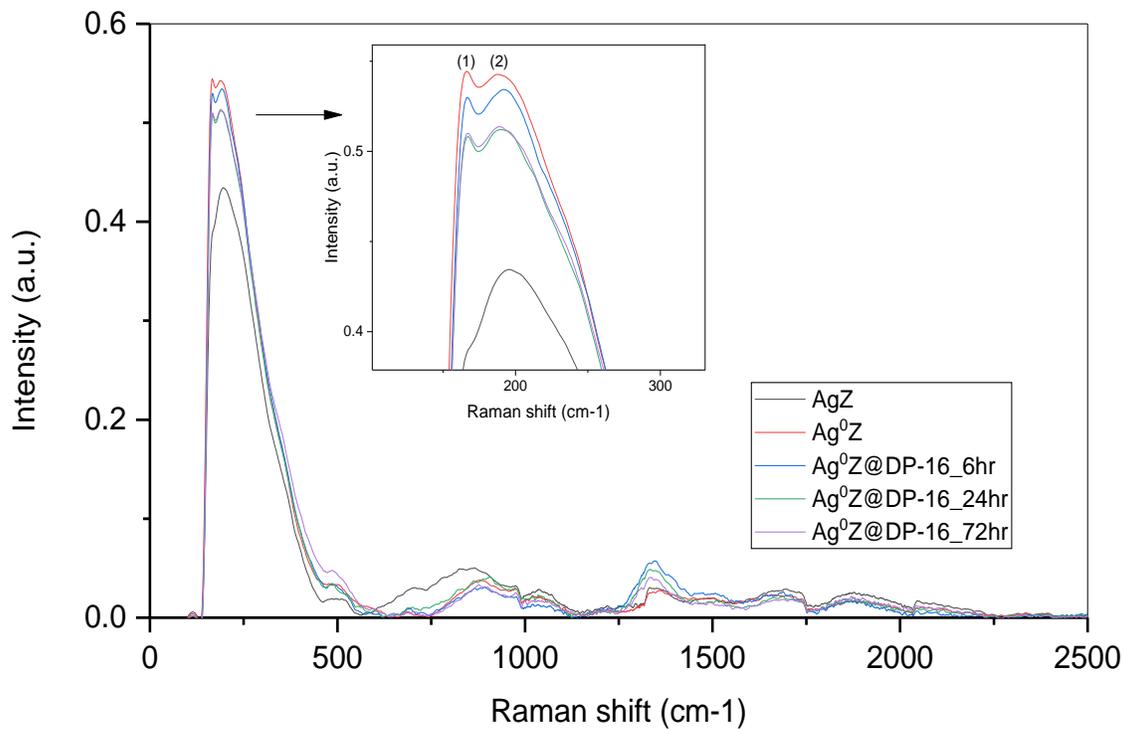
Figure 6-9. Raman spectra of Ag^0Z in Figure 6-6
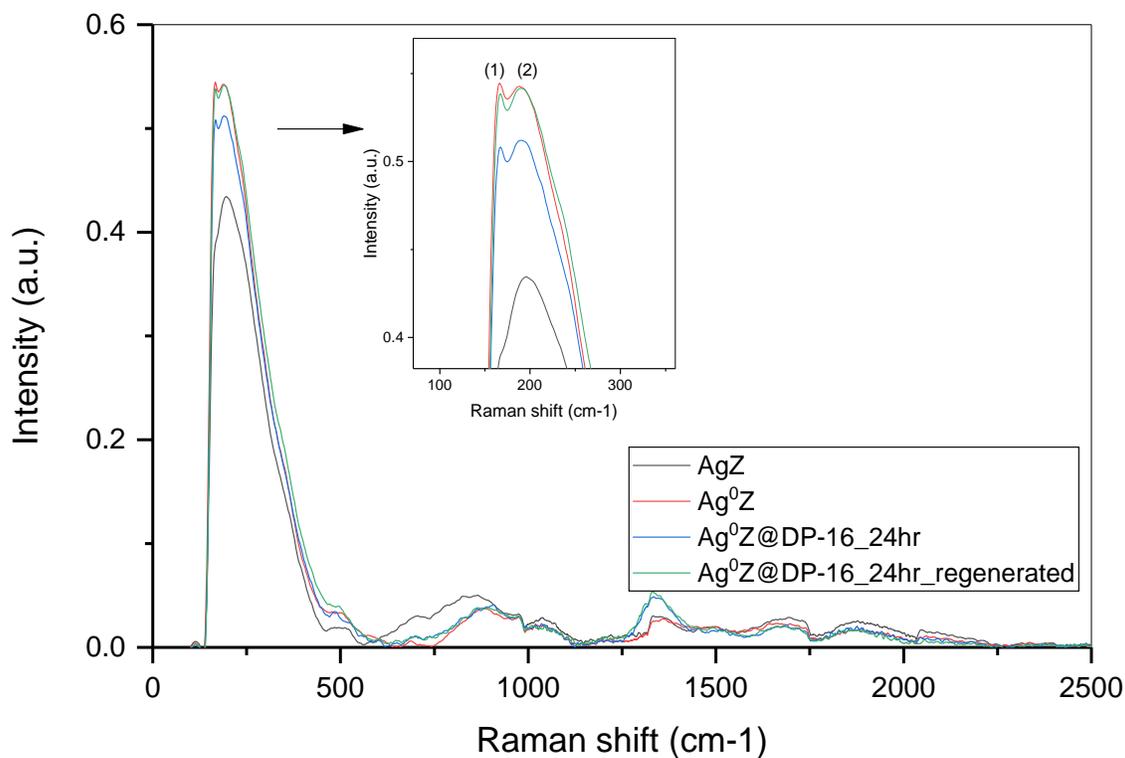
Figure 6-10. Raman spectra of Ag^0Z in Figure 6-7

To determine the mechanism for the deactivation or oxidation process of Ag^0Z in humid air gas stream. XPS analyses of the samples were performed to investigate the oxidation state of the Ag after treated in humid air flows. The results were reported recently by Nan et al.[159] in the study of aging processes of AgZ in nuclear off-gases. The samples were treated with off-gas components including water vapor (in the humid air of dew point -15 ℃) at 150 ℃ up to 6 months.

Figure 6-11 shows the spectra of Ag 3d region for Ag in standards and AgZ samples. The binding energy of Ag 3d 5/2 shifted from 368.4 eV to 367.6 eV when the Ag in AgZ was reduced to Ag^0 and formed Ag particles on Ag^0Z. The measured binding energies are in agreement with those measured by Aspromonte and coworkers.[146] When the Ag^0Z was treated in humid air for 2 months, the binding energy shifted back to a value of 367.9 eV. This should be due to the oxidation of a portion of the Ag particles as indicated by the XRD and Raman results. The BE value (367.9 eV) is in between those of Ag_2O (368.3 eV) and Ag^0Z, and it is also in between those of AgZ and Ag^0Z. Recall the results from the XRD and Raman that no Ag oxides were observed, the shift of binding energy back should be due to shift from Ag^0Z to AgZ upon humid air treatment.
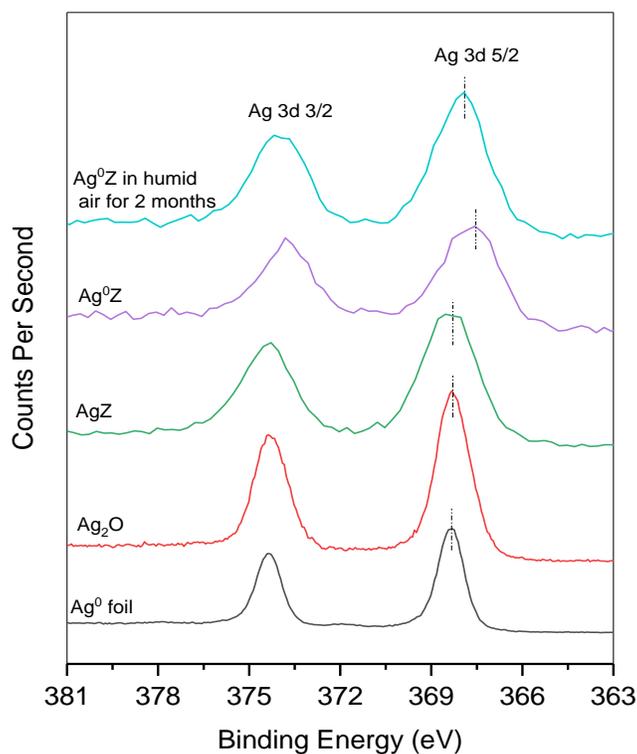
Figure 6-11. XPS spectra of Ag 3d for Ag standards and AgZ samples.

The deactivation mechanism was also investigated by XAFS analyses. The Ag spectra in the EXAFS region in **Figure 6-12a** show a shift of shape towards the directions demonstrated by the arrows when Ag^0Z in the humid air for 1, 2 and 4 months, indicating a change of oxidation state from Ag^0 to Ag^+. In addition, the treated samples had the same spectra. By comparing with the standards and untreated samples in **Figure 6-12b**, it was found that shift of shape in **Figure 6-12a** was towards the direction of AgZ instead of Ag_2O. This can be clearly observed by the first peak on the normalized spectra with the red arrow. Accordingly, it can be concluded that when treated in humid air, the Ag^0 particles were oxidized to Ag^+ and consequently migrated into the mordenite crystals.
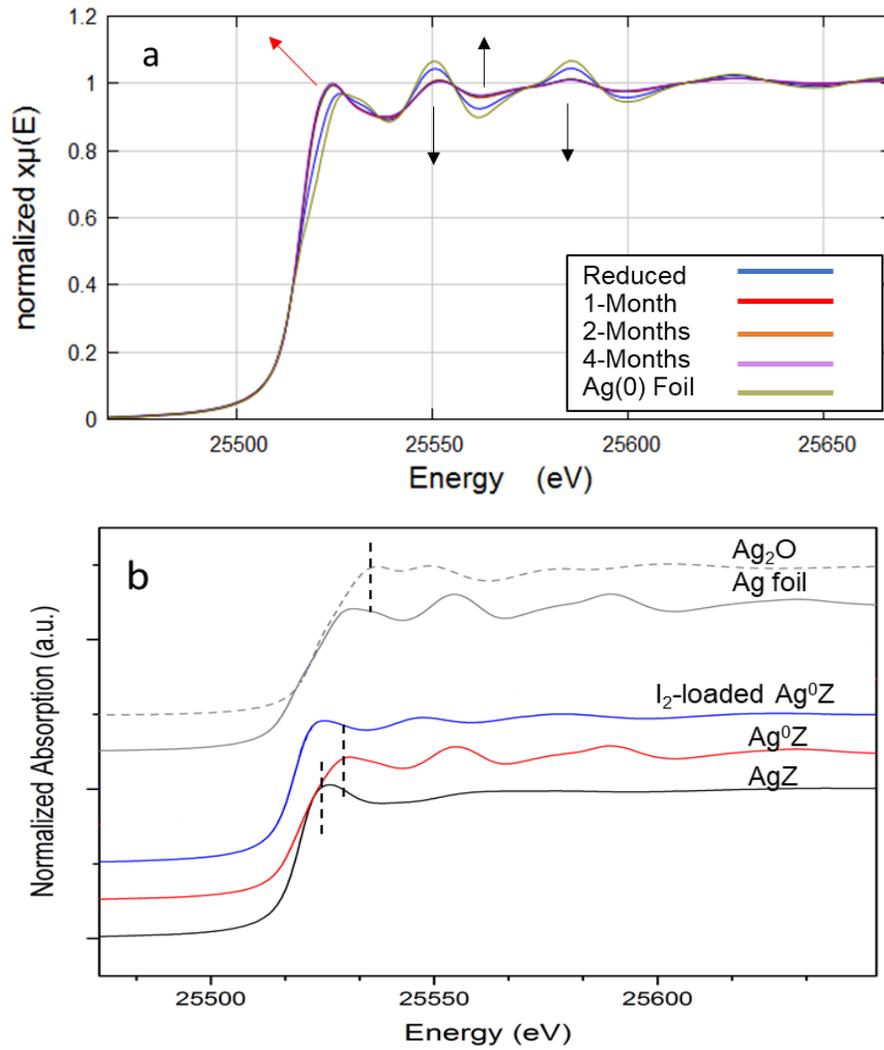
Figure 6-12. EXAFS of Ag^0Z samples (a) and Ag standards (b).

Accordingly, the deactivation of Ag^0Z in humid air stream involves both Ag oxidation and migration process. It is likely that the Ag particles were first oxidized by the O_2 and H_2O vapor to Ag oxides/hydroxides (Eq. 30 and 31), and the Ag^+ consequently migrated into the channels/pores of the mordenite crystals to replace the H^+ to bond with the active sites (Eq. 32). The H^+ was then combined with the O^{2-}/OH^- forming H_2O (Eq. 33

and 34). The Ag particles may be fully oxidized under ideal conditions. The deactivation

pathway is demonstrated in **Figure 6-13**.

$$O_2 + 4Ag = 4Ag^+ + 2\ O^{2-} \tag{30}$$

$$2H_2O + O_2 + 8Ag = 8Ag^+ + 4HO^- + 2\ O^{2-} \tag{31}$$

$$Ag^+ + HZ = AgZ + H^+ \tag{32}$$

$$2H^+ + O^{2-} = H_2O \tag{33}$$

$$H^+ + HO^- = H_2O \tag{34}$$
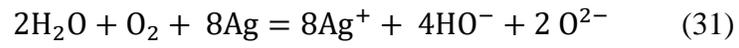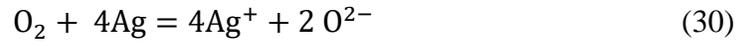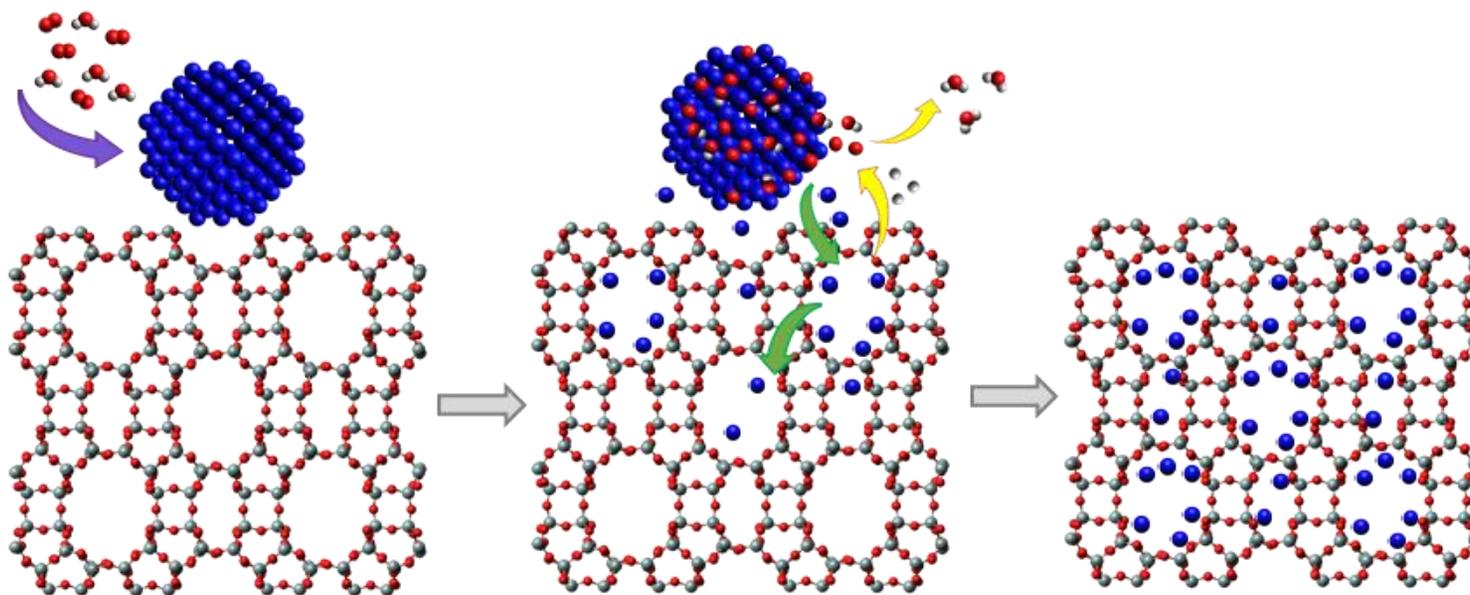
Figure 6-13. Deactivation pathway of Ag^{0}Z in humid air.

6.4. Conclusions

The investigation of I_2 and H_2O co-adsorption indicated that the capacity of Ag^0Z for I2 was decreased when co-adsorbing with water. A ~40 % relative loss in I_2 adsorption capacity was observed at an adsorption temperature of 150 ^oC in humid air streams of dew point -22 to 0 ^oC. By studying the Ag^0Z treated in the humid air of different dew points and treatment periods, it was found that the capacity loss was due to a chemical deactivation of the Ag in the Ag^0Z. The deactivation kinetics were found faster, reach equilibrium within 6 hr, compared with the I2 adsorption rate.

Through chemical analyses with XRD, Raman spectroscopy, XPS, and XAFS, the deactivation of Ag^0Z in the humid air was determined. It was found that, upon exposure to humid air, the Ag^0 particles in the Ag^0Z was oxidized to Ag^+ and then migrated to the mordenite crystals to replace the H^+ and bond to the mordenite framework.

The results provided valuable information for the design of the I_2 adsorption systems for nuclear off-gas treatment. For best use of the Ag^0Z adsorbent, water vapor should be removed from the off-gas streams in prior to passing through the Ag^0Z column to avoid deactivation of the adsorbent.

Chapter 7. Recommendations for Future Work

7.1. Aging Issues of Ag^0Z in Off Gases

Although Ag^0Z has been shown a good performance for iodine (CH_3I and I_2) adsorption by previous investigations and this work, there are several issues that need to be addressed to use Ag^0Z for treatment of nuclear-fuel reprocessing off-gas streams. One major problem is the loss of capacity due to aging processes when exposing to off gases including air, H_2O, NO and NO_2 over extended periods of time. As demonstrated by **Figure 7-1**, when the I_2 was captured by the front end of the Ag^0Z column, the rest of the off-gases will continue passing through the column, and the Ag^0Z at the end of the column will be exposed to these gases until the whole column is saturated. The exposure time could be up 6 months depending on the dimensions of the column. Therefore, the aging effect and mechanism must be determined.
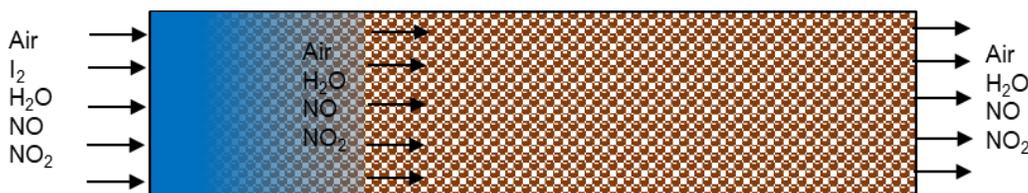
Figure 7-1. Demonstration of the aging process of a AgZ adsorption column in off-gases.

Even though the co-adsorption of I_2 and H_2O and the deactivation of Ag^0Z in humid air for short periods were studied in this work, long-term aging in gas streams including NO and NO_2 have not been adequately addressed. Previous studies have shown that the presence of NOx had a significant effect on the capacity of Ag^0Z.[79, 84-85, 92, 94, 96, 159-160] For example, Ag^0Z loses more than 90% of I_2 adsorption capacity when treated in a gas flow of 1% NO and 2% NO_2 for 1 month. However, the mechanisms of Ag^0Z deactivation in

NO and NO_2 are not clear yet. Understanding the mechanism of Ag^0Z deactivation in NOx is important for off-gas treatment system design and modification of the adsorbents to resolve the deactivation problems.

7.2. Organic Iodides Capture

In addition to the molecular iodine and methyl iodide which have been extensively studied in previous work, off-gas streams may also contain other organic iodides including both short chain and long chain alkyl iodides. These organic iodides were referred as penetrating gases because they were found difficult to be adsorbed by the adsorbent columns. According to report by Bruffey et al.,[161] which comprehensively summarized the information from previous studies on the organic iodides released during the nuclear fuel reprocessing process, the organic iodides potentially presented in the off-gases were mainly alkyl iodides ranged from C_1 iodide to C_{12} iodide. Among these, iodododecane (C_{12} iodide) could be most abundant organic form. In addition, these organic iodides will be mainly released into the vessel off-gases (VOG) at very low concentrations, ranging from 10 to 100 ppb. The low concentration also enlarges the difficulty in iodine capturing since the adsorption rate will be very low, resulting in a long-time aging of the adsorbent and a long saturation zone in the adsorption column.

For far, there are very few studies done on the adsorption of these organic iodides in VOG. The performance of adsorbents, adsorption mechanism and kinetics, as well as the effect of temperature and other co-adsorbing gases, are not clear yet. Therefore, future work should include a systematical study on adsorption of these organic iodides.

Notation

C_a Macropore gas concentration, mol/cm^3

C_b Gas concentration in bulk phase, g/cm^3

C_i Micropore gas concentration, mol/cm^3

C_{sa} Macropore adsorbed gas concentration, mol/cm^3

C_{si} Micropore adsorbed gas concentration, mol/cm^3

D_a Macropore diffusivity, cm^2/s

D_a' Macropore effective diffusivity, cm^2/s

D_i Micropore diffusivity, cm^2/s

D_i' Micropore effective diffusivity, cm^2/s

DP Dew point, ^{o}C

H_a Henry's law constant for macropore adsorption, cm^3/cm^3

H_i Henry's law constant for micropore adsorption, cm^3/cm^3

k_f External gas film mass transfer coefficient, cm/s

k_{LDF} Mass transfer coefficient of linear driving force model, time^{-1}

M_{AB} Average molecular weight of water and air, g/mol

n Number of micropheres per unite macrosphere volume

N_{degen} Scattering path

127

P Pressure, bar

q Total uptake at time t, g/g

q_e Total uptake at equilibrium, g/g

r_a Distance from macrosphere center, cm

r_i Distance from microsphere center, cm

R_a Macrosphere radius, cm

R_i Microsphere radius, cm

S Surface area, m^2/g

S_a Macropore surface area in Eq.1 and Eq.4, cm^2/cm^3

S_i Micropore surface area in Eq.2 and Eq.5, cm^2/cm^3

t Time

T Temperature, K

U_i Initial factional uptake rate, hr^{-1}

v_i Micropore volume, cm³/g

ρ_p Bulk density of pellet, g/cm^3

ν Atomic diffusion volume in Eq. 21

ε_p Porosity of pellet

ε_a Macropore porosity

ε_i Micropore porosity

$\sigma^2{}_i$ Relative mean square displacement of the scattering element

ΔE_0 energy shift of the photoelectron

ΔR_i Change in R_{eff}

Abbreviations

AgZ, silver-exchanged mordenite;

Ag^0Z, reduced silver-exchanged mordenite;

CFR, Code of Federal Regulations;

d-PDF / PDF, *(differential)*-Pair Distribution Function;

DOE, Department of Energy;

DOG, Dissolver off-gas;

DF, decontamination factor- the ratio between initial and final radioactivity following a

separation;

EPA, Environment Protection Agency;

EXAFS, extended x-ray absorption fine structure;

FCR&D, Fuel Cycle Research and Development;

LEL, lower explosive limit;

ICP-OES; inductively coupled plasma optical emission spectrometer;

NRC: Nuclear Regulatory Commission;

ppmv, parts per million by volume;

SEM-EDX, scanning electron microscopy- dispersive x-ray spectroscopy;

VOG, Vessel off-gas

XAFS, x-ray absorption fine structure;

XANES, x-ray absorption near edge spectrum;

XPS; x-ray photoelectron spectroscopy

XRD; x-ray diffraction

References

1.   Warner, E. S.; Heath, G. A., Life Cycle Greenhouse Gas Emissions of Nuclear Electricity Generation. *J. Ind. Ecol.* **2012,** *16*, S73-S92.

2.   Whitaker, M.; Heath, G. A.; O'Donoughue, P.; Vorum, M., Life Cycle Greenhouse Gas Emissions of Coal-Fired Electricity Generation. *J. Ind. Ecol.* **2012,** *16*, S53-S72.

3.   Nuclear Share of Electricity Generation in 2016. 19 April ed.; IAEA: 2017.

4.   Nandanwar, S. U.; Coldsnow, K.; Utgikar, V.; Sabharwall, P.; Eric Aston, D., Capture of harmful radioactive contaminants from off-gas stream using porous solid sorbents for clean environment – A review. *Chem. Eng. J.* **2016,** *306*, 369-381.

5.   Jubin, R. T. The Mass Transfer Dynamics of Gaseous Methyl-Iodide Adsorption by Silver-Exchanged Sodium Mordenite. The University of Tennessee, Knoxville, 1994.

6.   Soelberg, N. R.; Garn, T. G.; Greenhalgh, M. R.; Law, J. D.; Jubin, R.; Strachan, D. M.; Thallapally, P. K., Radioactive Iodine and Krypton Control for Nuclear Fuel Reprocessing Facilities. *Science and Technology of Nuclear Installations* **2013**, 12.

7.   Jubin, R. T.; DelCul, G.; Patton, B.; Owens, R.; Ramey, D.; Spencer, B. In *Advanced fuel cycle initiative coupled end-to-end research, development, and*

demonstration project: integrated off-gas treatment system design and initial performance-9226, WM2009 Conference, Phoenix, AZ, 2009.

8.   Mineo, H.; Iizuka, M.; Fujisaki, S.; Hotoku, S.; Asakura, T.; Uchiyama, G., Study on gaseous effluent treatment for dissolution step of spent nuclear fuel reprocessing. *NTIS Reports. NTIS No: DE2004-828968/XAB* **2002**.

9.   Zabaluev, Y., Management of radionuclides from reprocessing plant gaseous effluents. *IAEA Bull* **1979,** *21* (1), 23-31.

10.   Herrmann, F. J.; Motoi, V.; Herrmann, B.; Van Schoor, A.; Fang, D.; Fies, H. In *Retention and Measurement of Iodine-129 and of Organoiodine in the Offgas Streams of the Karlsruhe Reprocessing Plant WAK*, Proceedings of the 21st DOE/NRC Nuclear Air Cleaning Conference, 1990; pp 222-233.

11.   Robens, E.; Aumann, D., Iodine-129 in the environment of a nuclear fuel reprocessing plant: I. 127I and 127I contents of soils, food crops and animal products. *Journal of environmental radioactivity* **1988,** *7* (2), 159-175.

12.   Watanabe, Y.; Ikoma, T.; Yamada, H.; Suetsugu, Y.; Komatsu, Y.; Stevens, G. W.; Moriyoshi, Y.; Tanaka, J., Novel long-term immobilization method for radioactive iodine-129 using a zeolite/apatite composite sintered body. *ACS Appl Mater Interfaces* **2009,** *1* (7), 1579-84.

13.   Mineo, H.; Gotoh, M.; Iizuka, M.; Fujisaki, S.; Hagiya, H.; Uchiyama, G., Applicability of a model predicting iodine-129 profile in a silver nitrate silica-gel

column for dissolver off-gas treatment of fuel reprocessing. *Separ Sci Technol* **2003,** *38* (9), 1981-2001.

14.   EPA, Protection of environment: Chapter I-Environmental Protection Agency. Part 190-environmental radiation protection standards for nuclear power operations. Agency, U. E. P., Ed. US Environmental Protection Agency: Washington, DC, 2010; Vol. 40 CFR 190.10. .

15.   NRC, Standards for protection against radiation. US Nuclear Regulatory Commission: Washington, DC, 2012; Vol. 10 CFR 20.

16.   Strachan, D. M.; Chun, J.; Henager, C. H.; Matyas, J.; Riley, B. J.; Ryan, J. V.; Thallapally, P. K. *Summary report for the development of materials for volatile radionuclides*; FCRD-WAST-2010-000189; Pacific Northwest National Laboratory (PNNL), Richland, WA (US): 2010.

17.   Burger, L. L. *Determining criteria for the disposal of iodine-129*; Battelle Pacific Northwest Labs., Richland, WA (USA): 1980.

18.   Jubin, R. T.; Bruffey, S. H.; Strachan, D. M.; Soelberg, N. R.; Spencer, B. B.; Riley, B. J. *Performance Criteria for Capture and/or Immobilization Technologies*; INL/EXT--16-38035; ORNL/TM--2016-73; TRN: US1601583 United States 10.2172/1261239 TRN: US1601583 INL English; ; Idaho National Lab. (INL), Idaho Falls, ID (United States); Oak Ridge National Lab. (ORNL), Oak Ridge, TN (United States): 2016; p Medium: ED; Size: 35 p.

19. Soelberg, N. R.; Garn, T. G.; Greenhalgh, M. R.; Law, J. D.; Jubin, R.; Strachan, D. M.; Thallapally, P. K., Radioactive iodine and krypton control for nuclear fuel reprocessing facilities. *Sci. Technol. Nucl. Install.* **2013,** *2013*.

20. Gombert, D.; Counce, R.; Cozzi, A.; Crum, J.; Ebert, W.; Jantzen, C.; Jerden, J.; Jubin, R.; Kaminski, M.; Maio, V., Global nuclear energy partnership integrated waste management strategy waste treatment baseline study. *US DOE Report GNEP-WAST-WASTAI-RT-2007-000324, Idaho National Laboratory, Idaho Falls, ID, 69p* **2007**.

21. Holladay, D. W. *Literature survey: methods for the removal of iodine species from off-gases and liquid waste streams of nuclear power and nuclear fuel reprocessing plants, with emphasis on solid sorbents*; No. ORNL/TM-6350; Oak Ridge National Lab., TN (USA): Oak Ridge, TN (United States), 1979.

22. Haefner, D. R.; Tranter, T. J., Methods of gas phase capture of iodine from fuel reprocessing off-gas: a literature survey. *Idaho National Laboratory, Idaho Falls, ID* **2007**.

23. Haefner, D. R.; Law, J. D.; Tranter, T. J. *System design description and requirements for modeling the off-gas systems for fuel recycling facilities*; No. INL/EXT-10-18845; Idaho National Laboratory (INL): Idaho Falls, ID (United States), 2010.

24. Jubin, R. T.; Strachan, D. M.; Soelberg, N. R. *Iodine pathways and off-gas stream characteristics for aqueous reprocessing plants–A literature survey and*

assessment; Idaho National Laboratory (INL): Idaho Falls, ID (United States), 2013.

25.   Herrmann, F. J.; Motoi, V.; Fies, H.; Stojanik, B.; Furrer, J.; Kaempffer, R. *Testing an iodine filter for the vessel off-gas of the German industrial-scale reprocessing plant*; 1989.

26.   Goossens, W.; Baetsle, L.; Bruggeman, A.; Collard, G. In *Gas cleaning research and engineering in Belgium*, 15th Nuclear Air Cleaning Conference, Boston, MA, Boston, MA, 1979.

27.   Juhola, A. J., Iodine adsorption and structure of activated carbons. *Carbon* **1975,** *13* (5), 437-442.

28.   Furrer, M.; Buehler-Gloor, T. In *Revolatilisation of fission products, especially iodine, from water phases evaporating to dryness*, 2nd CSNI Workshop on Iodine Chemistry in Reactor Safety, Toronto, ON, Canada, Toronto, ON, Canada, 1989.

29.   Bhatia, S. K.; Liu, F.; Arvind, G., Effect of pore blockage on adsorption isotherms and dynamics: anomalous adsorption of iodine on activated carbon. *Langmuir* **2000,** *16* (8), 4001-4008.

30.   Gal, I. J.; Muk, A.; Todorovic, M.; Rajnvajn, J.; Cvjeticanin, D.; Vujisic, L. *Adsorption of methyl iodide on impregnated alumina*; 1975.

31.   Scheele, R. D.; Burger, L. L.; Halko, B. T., Comparison of silver sorbents for application to radioiodine control at the PUREX process facility modification. *PNL-6607 Pacific Northwest Laboratory, Richland, WA* **1988**.

32.   Scheele, R. D.; Burger, L. L.; Halko, B. T.; Waters, E. D.; Orme, R. M. *Performance of some silver sorbents for control of radioiodine from nuclear fuel operations*; PNL-SA-15691; Pacific Northwest Lab: Richland, WA (USA), 1988.

33.   Burger, L. L.; Scheele, R. D. *Iodine fixation studies at the Pacific Northwest Laboratory: Management modes for iodine-129*; PNL-SA-9829; Pacific Northwest Laboratory: Richland, WA, 1982.

34.   Pence, D. T.; Duce, F. A.; Maeck, W. J. *STUDY OF THE ADSORPTION PROPERTIES OF METAL ZEOLITES FOR AIRBORNE IODINE SPECIES*; Idaho Nuclear Corp., Idaho Falls: 1971.

35.   Pence, D. T.; Duce, F. A.; Maeck, W. J., Iodine adsorbents program, idaho chemical programs annual technical report fiscal year 1971. *ICP1006* **1972**.

36.   Wu, L.; Sawada, J. A.; Kuznicki, D. B.; Kuznicki, T.; Kuznicki, S. M., Iodine adsorption on silver-exchanged titania-derived adsorbents. *J. Radioanal. Nucl. Chem.* **2014,** *302* (1), 527-532.

37.   Riley, B. J.; Chun, J.; Ryan, J. V.; Matyas, J.; Li, X. S.; Matson, D. W.; Sundaram, S. K.; Strachan, D. M.; Vienna, J. D., Chalcogen-based aerogels as a multifunctional platform for remediation of radioactive iodine. *RSC. Adv.* **2011,** *1* (9), 1704-1715.

38. Riley, B. J.; Chun, J.; Um, W.; Lepry, W. C.; Matyas, J.; Olszta, M. J.; Li, X.; Polychronopoulou, K.; Kanatzidis, M. G., Chalcogen-Based Aerogels As Sorbents for Radionuclide Remediation. *Environ. Sci. Technol.* **2013,** *47* (13), 7540-7547.

39. Riley, B. J.; Pierce, D. A.; Chun, J.; Matyáš, J.; Lepry, W. C.; Garn, T. G.; Law, J. D.; Kanatzidis, M. G., Polyacrylonitrile-Chalcogel Hybrid Sorbents for Radioiodine Capture. *Environ. Sci. Technol.* **2014,** *48* (10), 5832-5839.

40. Subrahmanyam, K. S.; Sarma, D.; Malliakas, C. D.; Polychronopoulou, K.; Riley, B. J.; Pierce, D. A.; Chun, J.; Kanatzidis, M. G., Chalcogenide Aerogels as Sorbents for Radioactive Iodine. *Chem. Mater.* **2015,** *27* (7), 2619-2626.

41. Sava, D. F.; Rodriguez, M. A.; Chapman, K. W.; Chupas, P. J.; Greathouse, J. A.; Crozier, P. S.; Nenoff, T. M., Capture of Volatile Iodine, a Gaseous Fission Product, by Zeolitic Imidazolate Framework-8. *J. Am. Chem. Soc.* **2011,** *133* (32), 12398-12401.

42. Sava, D. F.; Chapman, K. W.; Rodriguez, M. A.; Greathouse, J. A.; Crozier, P. S.; Zhao, H.; Chupas, P. J.; Nenoff, T. M., Competitive I_2 Sorption by Cu-BTC from Humid Gas Streams. *Chem. Mater.* **2013,** *25* (13), 2591-2596.

43. Chapman, K. W.; Sava, D. F.; Halder, G. J.; Chupas, P. J.; Nenoff, T. M., Trapping Guests within a Nanoporous Metal–Organic Framework through Pressure-Induced Amorphization. *J. Am. Chem. Soc.* **2011,** *133* (46), 18583-18585.

44.   Hughes, J. T.; Sava, D. F.; Nenoff, T. M.; Navrotsky, A., Thermochemical Evidence for Strong Iodine Chemisorption by ZIF-8. *J. Am. Chem. Soc.* **2013,** *135* (44), 16256-16259.

45.   Sava, D. F.; Garino, T. J.; Nenoff, T. M., Iodine Confinement into Metal–Organic Frameworks (MOFs): Low-Temperature Sintering Glasses To Form Novel Glass Composite Material (GCM) Alternative Waste Forms. *Ind. Eng. Chem. Res.* **2012,** *51* (2), 614-620.

46.   Assfour, B.; Assaad, T.; Odeh, A., In silico screening of metal organic framework for iodine capture and storage. *Chem. Phys. Lett.* **2014,** *610–611*, 45-49.

47.   Nandanwar, S. U.; Coldsnow, K.; Utgikar, V.; Sabharwall, P.; Aston, D. E.; Zhang, Y., Synthesis and characterization of ETS-10: supported hollow carbon nano-polyhedrons nanosorbent for adsorption of krypton at near ambient temperatures. *Adsorption* **2016,** *22* (2), 129-137.

48.   Anson, A.; Maham, Y.; Lin, C. C. H.; Kuznicki, T. M.; Kuznicki, S. M., XPS Characterization of Silver Exchanged ETS-10 and Mordenite Molecular Sieves. *J. Nanosci. Nanotechnol.* **2009,** *9* (5), 3134-3137.

49.   Liu, Y.; Chen, F.; Wasylishen, R. E.; Xu, Z.; Sawada, J.; Kuznicki, S. M., A Study of Silver Species on Silver-Exchanged ETS-10 and Mordenite by XRD, SEM and Solid-State 109Ag, 29Si and 27Al NMR Spectroscopy. *J. Nanosci. Nanotechnol.* **2012,** *12* (8), 6420-6427.

50. Yang, J. H.; Shin, J. M.; Park, J. J.; Park, G. I.; Yim, M. S., Novel synthesis of bismuth-based adsorbents for the removal of 129I in off-gas. *J. Nucl. Mater.* **2015,** *457*, 1-8.

51. Yang, J. H.; Cho, Y.-J.; Shin, J. M.; Yim, M.-S., Bismuth-embedded SBA-15 mesoporous silica for radioactive iodine capture and stable storage. *J. Nucl. Mater.* **2015,** *465*, 556-564.

52. Outokesh, M.; Saket, A.; Ahmadi, S. J.; Hosseinpour, M.; Khanchi, A. R., Comparative Study on Adsorption of Iodine Vapor by Silica-Supported Cu Nanoparticles and Micronized Copper. *Ind. Eng. Chem. Res.* **2012,** *51* (47), 15315-15323.

53. Gombert, D.; Ebert, W.; Marra, J.; Jubin, R.; Vienna, J. *Global Nuclear Energy Partnership Waste Treatment Baseline*; INL/CON-08-13917; Idaho National Laboratory: Idaho Falls, Idaho, USA, 2008.

54. Haefner, D. R.; Tranter, T. J. *Methods of gas phase capture of iodine from fuel reprocessing off-gas: a literature survey*; INL/EXT-07-12299; Idaho National Laboratory: Idaho Falls, Idaho, USA, 2007.

55. Scheele, R. D.; Wend, C. F., Solidification and stabilization of silver mordenite used to control radioiodine emissions from Hanford's Waste Treatment Plant. *Annals of Nuclear Energy* **2015,** *78*, 40-48.

56.   Staples, B. A.; Murphy, L. P.; Thomas, T. R. *Airborne elemental iodine loading capacities of metal zeolites and a dry method for recycling silver zeolite*; No. CONF-760822--P1; Pacific Northwest Laboratory: Washington, D.C., 1976.

57.   Thomas, T. R.; Staples, B. A.; Murphy, L. P. *Development of Ag0Z for bulk 129I removal from nuclear fuel reprocessing plants and PbX for 129I storage*; CONF-780819--15; Idaho National Engineering Lab: Idaho 1978.

58.   Jubin, R. In *Organic Iodine Removal from Simulated Dissolver Off-Gas Streams Using Silver Exchanged Mordenite*, Proceedings of the 16th DOE Nuclear Air and Cleaning Conference, San Diego, CA, 1980; pp 20-23.

59.   Scheele, R.; Burger, L.; Halko, B.; Waters, E.; Orme, R. *Performance of some silver sorbents for control of radioiodine from nuclear fuel operations*; No. PNL-SA-15691; CONF-880815-10; Pacific Northwest Lab., Richland, WA (USA): 1988.

60.   Jubin, R. In *Organic iodine removal from simulated dissolver off-gas systems using partially exchanged silver mordenite*, Proceedings of the 17th DOE Nuclear Air Cleaning Conference, CONF-820833, 1983; pp 183-197.

61.   Scheele, R. D.; Wend, C. F.; Buchmiller, W. C.; Kozelisky, A. E.; Sell, R. L. *Preliminary evaluation of spent silver mordenite disposal forms resulting from gaseous radioiodine control at Hanford's Waste Treatment Plant*; PNWD-3225, WTP-RPT-039; Pacific Northwest Laboratory: Richland, WA, 2002.

62. Spencer, B. B.; Bruffey, S. H.; J, J. F. W. *Evaluation of iodine and water Co-adsorption on silver-functionalized aerogel*; ORNL/SPR--2015/176; Oak Ridge National Laboratory: Oak Ridge, TN (United States), 2015.

63. Nan, Y.; Lin, R.; Liu, J.; Crowl, T. B.; Ladshaw, A.; Yiacoumi, S.; Tsouris, C.; Tavlarides, L. L., Adsorption Equilibrium and Modeling of Water Vapor on Reduced and Unreduced Silver-Exchanged Mordenite. *Industrial & Engineering Chemistry Research* **2017,** *56* (28), 8095-8102.

64. Chibani, S.; Chebbi, M.; Lebegue, S.; Bucko, T.; Badawi, M., A DFT investigation of the adsorption of iodine compounds and water in H-, Na-, Ag-, and Cu-mordenite. *J Chem Phys* **2016,** *144* (24), 244705.

65. Yue Nan; Ladshaw, A. P.; Yiacoumi, S.; Tsouris, C.; DePaoli, D. W.; Tavlarides, L. L. In *Co-adsorption of I2 and H2O on Ag0Z*, 2016 AIChE Annual Meeting, San Francisco,CA, San Francisco,CA, 2016.

66. Nan, Y.; Ladshaw, A. P.; Yiacoumi, S.; Tsouris, C.; DePaoli, D. W.; Tavlarides, L. L., Co-adsorption of I2 and H2O on Ag0Z and Kinetics of Silver-Iodine Reaction. In *2016 ANS Anual Meeting*, Transactions of the American Nuclear Society, New Orleans, LA, 2016; Vol. 114, pp 165-166.

67. Lyon, K. L.; Welty, A. K.; Law, J.; Ladshaw, A.; Yiacoumi, S.; Tsouris, C. *Off-Gas Adsorption Model Capabilities and Recommendations*; INL/EXT--16-37975; TRN: US1601557 United States 10.2172/1260462 TRN: US1601557 INL English;

; Idaho National Laboratory (INL), Idaho Falls, ID (United States): 2016; p Medium: ED; Size: 40 p.

68.   Riley, B. J.; Vienna, J. D.; Strachan, D. M.; McCloy, J. S.; Jerden, J. L., Materials and processes for the effective capture and immobilization of radioiodine: A review. *Journal of Nuclear Materials* **2016,** *470*, 307-326.

69.   Jubin, R., Organic iodine removal from simulated dissolver off-gas streams using silver-exchanged mordenite. **1980**.

70.   Jubin, R. T. *The mass transfer dynamics of gaseous methyl-iodide adsorption by silver-exchanged sodium mordenite*; Oak Ridge National Lab: Oak Ridge, TN (United States), 1994.

71.   Scheele, R. D.; Burger, L. L.; Matsuzaki, C. L. *Methyl iodide sorption by reduced silver mordenite*; PNL-4489; Pacific Northwest Laboratory: Richland, WA 1983.

72.   Bryan, D.; Strachan, S.; Levitskaia, C.; Henager, T.; Thallapally, J.; Matyàš, P.; Weber, R.; Scheele, W.; Richard, Z. *Processes for Removal and Immobilization of 14 C, 129 I, and 85 Kr*; PNNL-18852; Pacific Northwest National Laboratory Richland, Washington 99352, 2009.

73.   Haefner, D. R.; Watson, T. L.; Jones, M. G. *Summary of FY 2010 Iodine Capture Studies at the INL*; INL/EXT-10-19657; Idaho National Laboratory (INL): Idaho Falls, ID (United States), 2010.

74. Paviet-Hartmann, P.; Kerlin, W.; Bakhtiar, S. *Treatment of gaseous effluents issued from recycling–A review of the current practices and prospective improvements*; No. INL/CON-10-19961; Idaho National Laboratory (INL): Idaho Falls, ID (United States), 2010.

75. Strachan, D. M.; Chun, J.; Matyas, J.; Lepry, W. C.; Riley, B. J.; Ryan, J. V.; Thallapally, P. K. *Summary report on the volatile radionuclide and immobilization research for FY2011 at PNNL*; Pacific Northwest National Laboratory (PNNL), Richland, WA (US), Environmental Molecular Sciences Laboratory (EMSL): 2011.

76. Soelberg, N.; Watson, T. *Iodine sorbent performance in FY 2012 deep bed tests*; INL/EXT-12-27075; Idaho National Laboratory (INL): Idaho Falls, ID, 2012.

77. Spencer, B. B.; Bruffey, S. H.; Jubin, R. T. *TEST PLAN TO DEMONSTRATE REMOVAL OF IODINE AND TRITIUM FROM*

SIMULATED NUCLEAR FUEL RECYCLE PLANT OFF-GAS STREAMS USING ADSORPTION PROCESSES; ORNL/LTR--2013/542; Other: AF5805000; NEAF327 United States 10.2172/1210127 Other: AF5805000; NEAF327 ORNL English; ; Oak Ridge National Lab. (ORNL), Oak Ridge, TN (United States): 2013; p Medium: ED; Size: 18 p.

78. Jubin, R. T. *Advances in Off-Gas Treatment for Used Nuclear Fuel Processing*; Oak Ridge National Laboratory (ORNL): 2014.

79.   Bruffey, S. H.; Jubin, R. T.; Patton, K. K.; Walker Jr, J. F. *Aging of iodine-loaded silver mordenite in NO2*; Oak Ridge National Laboratory (ORNL), Oak Ridge, TN (United States): 2014.

80.   Nenoff, T. M.; Rodriguez, M. A.; Soelberg, N.; Chapman, K. *Determine Mechanism of CH3I Capture in AgZ*; Sandia National Laboratories (SNL-NM), Albuquerque, NM (United States): 2014.

81.   Nenoff, T. M.; Soelberg, N. *Studies on the Mechanisms of Methyl Iodide Adsorption and Iodine Retention on Silver-Mordenite*; SAND2014--17740R; Other: 537547 United States 10.2172/1171585 Other: 537547 SNL English; ; Sandia National Laboratories (SNL-NM), Albuquerque, NM (United States): 2014; p Medium: ED; Size: 4 p.

82.   Patton, K. K.; Bruffey, S. H.; Jubin, J. T.; Walker Jr, J. F. *Iodine Loading of NO Aged Silver Exchanged Mordenite*; Oak Ridge National Laboratory (ORNL): Oak Ridge, TN (United States), 2014.

83.   Soelberg, N.; Watson, T. *Phase 2 Methyl Iodide Deep-Bed Adsorption Tests*; Idaho National Laboratory (INL), Idaho Falls, ID (United States): 2014.

84.   Bruffey, S.; Jubin, R. *Initial Evaluation of Effects of NOx on Iodine and Methyl Iodide Loading of AgZ and Aerogels*; Oak Ridge National Laboratory (ORNL), Oak Ridge, TN (United States), 2015; p 125.

85.   Bruffey, S.; Patton, K.; Walker Jr, J.; Jubin, R. *Complete NO and NO2 Aging Study for AgZ*; Oak Ridge National Laboratory (ORNL), Oak Ridge, TN (United States), 2015; p 128.

86.   Bruffey, S. H.; Jubin, R. T. *Recommend HIP Conditions for AgZ*; ORNL/SPR-2015/503; Oak Ridge National Laboratory: Oak Ridge, TN (United States), 2015.

87.   Soelberg, N. R.; Watson, T. L. *FY-2015 Methyl Iodide Deep-Bed Adsorption Test Report*; INL/EXT--15-36817; TRN: US1601199 United States 10.2172/1245523 TRN: US1601199 INL English; ; Idaho National Laboratory (INL), Idaho Falls, ID (United States): 2015; p Medium: ED; Size: 32 p.

88.   Nan, Y.; Tavlarides, L. L.; DePaoli, D. W., Adsorption of iodine on hydrogen‐reduced silver‐exchanged mordenite: Experiments and modeling. *AIChE Journal* **2017** *63* (3), 1024‐1035.

89.   Todd, T. A.; Braase, L. A. *Material Recovery and Waste Form Development FY 2015 Accomplishments Report*; INL/EXT--15-37053; TRN: US1600537 United States 10.2172/1238211 TRN: US1600537 INL English; ; Idaho National Laboratory (INL), Idaho Falls, ID (United States): 2015; p Medium: ED; Size: 179 p.

90.   Bruffey, S.; Jubin, R.; Jordan, J. *Organic Iodine Adsorption by AgZ under Prototypical Vessel Off-Gas Conditions*; ORNL/TM-2016/568; 2016.

91.   Soelberg, N.; Watson, T. *FY-2016 Methyl Iodide Higher NOx Adsorption Test Report*; INL/EXT-16-40087; Idaho National Laboratory: Idaho 2016.

92.   Jordan, J. A.; Jubin, R. T. *Stability of Tritium and Iodine Sorbents under Tritium-Pretreatment Off-Gas Conditions*; ORNL/SR-2017/162; Oak Ridge National Laboratory: Oak Ridge, TN, 2017.

93.   Spencer, B. B.; Bruffey, S. H.; Jordan, J. A.; Jubin, R. T. *Design of a Tritium and Iodine Removal System for Use with Advanced Tritium Pretreatment*; ORNL/SR-2017/116; Oak Ridge National Laboratory: Oak Ridge ,TN, 2017.

94.   Bruffey, S. In *Iodine Capture on Silver Mordenite: Effects of reduction, aging, and water adsorption*, JNFL/DOE/AREVA Technical Exchange, 2012.

95.   Jubin, R. T. In *Off- Gas Sigma Team: Recent Advances in the Capture / Sequestration of Volatile Radionuclides from Fuel Reprocessing*, 2012.

96.   R. T. Jubin; D. W. Ramey; B. B. Spencer; K. K. Anderson; Robinson, S. M. In *Impact of Pretreatment and Aging on the Iodine Capture Performance of Silver-Exchanged Mordenite* WM2012 Conference, Phoenix, AZ, Phoenix, AZ, 2012.

97.   Kaara K. Patton; S. H. Bruffey; R. T. Jubin; J. F. Walker, J. In *Effects of Extended In-Process Aging of Silver-Exchanged Mordenite on Iodine Capture Performance*, 33rd Nuclear Air Cleaning Conference, St Louis, MO, St Louis, MO, 2014.

98. Bruffey, S. H.; Jubin, R. T.; Jordan, J. A., Capture of Elemental and Organic Iodine from Dilute Gas Streams by Silver-exchanged Mordenite. *Procedia Chemistry* **2016,** *21*, 293-299.

99. Thomas, T. R.; Staples, B. A.; Murphy, L. P., Development of Ag^{0}Z for bulk ^{129}I removal from nuclear fuel reprocessing plants and PbX for ^{129}I storage. In *Proc. 15th DOE Nuclear Air Cleaning Conference, CONF-780819*, Boston, MA, USA, 1978.

100. Jubin, R. T., Organic iodine removal from simulated dissolver off-gas streams using partially exchanged silver mordenite. In *Proc. 16th DOE nuclear air cleaning conference, CONF-801038*, San Diego, CA, USA, 1980.

101. Beyer, H. K.; Jacobs, P. A., Chemical Evidence for Charged Clusters in Silver Zeolites. In *Stud. Surf. Sci. Catal.*, P.A. Jacobs, N. I. J. P. J.; Schulz-Ekloff, G., Eds. Elsevier: 1982; Vol. Volume 12, pp 95-102.

102. Nan, Y.; Ladshaw, A. P.; Yiacoumi, S.; Tsouris, C.; DePaoli, D. W.; Tavlarides, L. L., Adsorption of I2 from Off-Gases from Spent Fuel Reprocessing Plants. In *2015 ANS Annual Meeting*, Transactions of the American Nuclear Society: San Antonio, TX, 2015; Vol. 112 pp 57-58.

103. Zhao, H. Y.; Nenoff, T. M.; Jennings, G.; Chupas, P. J.; Chapman, K. W., Determining Quantitative Kinetics and the Structural Mechanism for Particle Growth in Porous Templates. *J Phys Chem Lett* **2011,** *2* (21), 2742-2746.

104. Shiojiri, M.; Hasegawa, Y.; Konishi, K., Reaction of iodine vapor with silver films in the β‑AgI phase region. *Journal of Applied Physics* **1973,** *44* (7), 2996-3000.

105. Chibani, S.; Medlej, I.; Lebègue, S.; Ángyán, J. G.; Cantrel, L.; Badawi, M., Performance of CuII‑, PbII‑, and HgII‑Exchanged Mordenite in the Adsorption of I2, ICH3, H2O, CO, ClCH3, and Cl2: A Density Functional Study. *ChemPhysChem* **2017,** *18* (12), 1642–1652.

106. Diaby, S., Effect of Water Adsorption on Cation-Surface Interaction Energy in the Na-Mordenite of 5.5: 1 Si/Al Ratio. *J Chem-Ny* **2016,** *2016* (2016), 2090-9063.

107. Devautour, S.; Abdoulaye, A.; Giuntini, J. C.; Henn, F., Localization of water molecules and sodium ions in Na-mordenite, by thermally stimulated current measurement. *Journal of Physical Chemistry B* **2001,** *105* (38), 9297-9301.

108. Douillard, J. M.; Maurin, G.; Henn, F.; Devautour-Vinot, S.; Giuntini, J. C., Use of dielectric relaxation for measurements of surface energy variations during adsorption of water on mordenite. *J Colloid Interf Sci* **2007,** *306* (2), 440-448.

109. Kawamura, Y.; Edao, Y.; Iwai, Y.; Hayashi, T.; Yamanishi, T., Hydrogen and water vapor adsorption properties on cation-exchanged mordenite for use to a tritium recovery system. *Fusion Engineering and Design* **2014,** *89* (7-8), 1539-1543.

110. Kim, S. I.; Aida, T.; Niiyama, H., Binary adsorption of very low concentration ethylene and water vapor on mordenites and desorption by microwave heating. *Separation and Purification Technology* **2005,** *45* (3), 174-182.

111.   Slinkin, A. A.; Kucherov, A. V., Formation of Radicals in the Adsorption of Olefins on H-Mordenite .3. Influence of Oxygen, Ammonia, Water, and SO2 on the Formation of Radical Particles and High-Temperature Conversions. *Kinet Catal+* **1983,** *24* (4), 811-817.

112.   Nan, Y.; DePaoli, D. W.; Tavlarides, L. L. In *Adsorption of Radioactive I2 and Tritiated Water from Spent Fuel Reprocessing Off-Gases by Reduced Silver Mordenite*, 2015 AIChE Annual Meeting, Salt Lake City, UT, Salt Lake City, UT, 2015

113.   Nan, Y.; DePaoli, D. W.; Tavlarides, L. L. In *Adsorption of iodine and water on reduced silver-exchanged mordenite*, 19th Symposium on Separation Science and Technology for Energy Applications, , Getlinberg, TN, , Getlinberg, TN, 2016.

114.   Lin, R. H.; Ladshaw, A.; Nan, Y.; Liu, J. X.; Yiacoumi, S.; Tsouris, C.; DePaoli, D. W.; Tavlarides, L. L., Isotherms for Water Adsorption on Molecular Sieve 3A: Influence of Cation Composition. *Industrial & Engineering Chemistry Research* **2015,** *54* (42), 10442-10448.

115.   Lin, R.; Liu, J.; Nan, Y.; DePaoli, D. W.; Tavlarides, L. L., Kinetics of Water Vapor Adsorption on Single-Layer Molecular Sieve 3A: Experiments and Modeling. *Industrial & Engineering Chemistry Research* **2014,** *53* (41), 16015-16024.

116.   Tavlarides, L. L.; Lin, R.; Nan, Y.; Yiacoumi, S.; Tsouris, C.; Ladshaw, A.; Sharma, K.; Gabitto, J.; DePaoli, D. *Sorption Modeling and Verification for Off-Gas Treatment*; DOE/NEUP--11-3175; Syracuse Univ., NY (United States);

Georgia Inst. of Technology, Atlanta, GA (United States); Prairie View A & M Univ., Prairie View, TX (United States); Oak Ridge National Lab.(ORNL), Oak Ridge, TN (United States): 2015.

117.   Lin, R.; Nan, Y.; DePaoli, D. W.; Tavlarides, L. L. In *Adsorption of Iodine and Water on Molecular Sieve 3A*, 2014 AIChE Annual Meeting, Atlanta, GA, Atlanta, GA, 2014.

118.   Brunauer, S.; Emmett, P. H.; Teller, E., Adsorption of gases in multimolecular layers. *Journal of the American Chemical Society* **1938,** *60*, 309-319.

119.   Harkins, W. D.; Jura, G., Surfaces of solids XIII A vapor adsorption method for the determination of the area of a solid without the assumption of a molecular area, and the areas occupied by nitrogen and other molecules on the surface of a solid. *Journal of the American Chemical Society* **1944,** *66*, 1366-1373.

120.   Barrett, E. P.; Joyner, L. G.; Halenda, P. P., The Determination of Pore Volume and Area Distributions in Porous Substances .1. Computations from Nitrogen Isotherms. *Journal of the American Chemical Society* **1951,** *73* (1), 373-380.

121.   Segre, C. U.; Leyarovska, N. E.; Chapman, L. D.; Lavender, W. M.; Plag, P. W.; King, A. S.; Kropf, A. J.; Bunker, B. A.; Kemner, K. M.; Dutta, P.; Duran, R. S.; Kaduk, J. In *The MRCAT Insertion Device Beamline at the Advanced Photon Source*, Synchrotron Radiation Instrumentation: Eleventh U.S. National Conference, New York, NY (USA), Pianetta, P., Ed. American Institute of Physics: New York, NY (USA), 2000; pp 419-422.

122. Abney, C. W.; Nan, Y.; Tavlarides, L. L., X-ray Absorption Spectroscopy Investigation of Iodine Capture by Silver-Exchanged Mordenite. *Industrial & Engineering Chemistry Research* **2017,** *56* (16), 4837-4846.

123. Teo, B. K., *EXAFS: Basic Principles and Data Analysis*. Springer: Verlag Berlin Heidelberg, 1986.

124. Ravel, B.; Newville, M., ATHENA, ARTEMIS, HEPHAESTUS: Data Analysis for X-ray Absorption Spectroscopy using IFEFFIT. *J. Synchrotron Radiat.* **2005,** *12* (4), 537-541.

125. Rehr, J. J.; Albers, R. C., Theoretical approaches to x-ray absorption fine structure. *Rev. Mod. Phys.* **2000,** *72* (3), 621-654.

126. Spreadborough, J.; Christian, J. W., High-Tempearture X-ray Diffractometer. *J. Sci. Instru.* **1959,** *36*, 116-118.

127. Wyckoff, R. W. G., The Crystal Structure of Silver Oxide (Ag$_2$O). *Am. J. Sci.* **1922,** *3*, 184-188.

128. Helmholz, L., The Crystal Structure of Hexagonal Silver Iodide. *J. Chem. Phys.* **1935,** *3*, 740-747.

129. Wyckoff, R. W. G., *Crystal Structures*. 2nd ed.; Interscience Publishers: New York, New York (USA), 1963.

130.   Wright, A. F.; Fender, B. E. F., The Structure of Superionic Compounds by Powder Neutron Diffraction. 1. Cation Distribution in α-AgI. *J. Phys. C: Solid St. Sci.* **1977,** *10*, 2261-2267.

131.   Calvin, S., *XAFS for Everyone*. CRC Press: Boca Raton, FL, 2013.

132.   Ruthven, D. M., *Principles of adsorption and adsorption processes*. John Wiley & Sons: 1984.

133.   Do, D. D., *Adsorption analysis: Equilibria and Kinetics*. Imperial College Press: London, 1998.

134.   Ruckenstein, E.; Vaidyanathan, A. S.; Youngquist, G. R., Sorption by Solids with Bidisperse Pore Structures. *Chem Eng Sci* **1971,** *26* (9), 1305-1318.

135.   Kärger, J.; Ruthven, D., Diffusion in zeolites. *Handbook of Zeolite Science and Technology* **1992,** *341*.

136.   Glueckauf, E.; Coates, J. I., Theory of Chromatography .4. The Influence of Incomplete Equilibrium on the Front Boundary of Chromatograms and on the Effectiveness of Separation. *J Chem Soc* **1947,** (10), 1315-1321.

137.   Sips, R., On the Structure of a Catalyst Surface. *Journal of Chemical Physics* **1948,** *16* (5), 490-495.

138.   Toth, J., State Equations of Solid-Gas Interface Layers. *Acta Chim Hung* **1971,** *69* (3), 311-317.

139.   Sips, R., On the Structure of a Catalyst Surface .2. *Journal of Chemical Physics* **1950,** *18* (8), 1024-1026.

140.   Honig, J. M.; Reyerson, L. H., Adsorption of Nitrogen, Oxygen, and Argon on Rutile at Low Temperatures - Applicability of the Concept of Surface Heterogeneity. *J Phys Chem-Us* **1952,** *56* (1), 140-144.

141.   Myers, A. L., Activity-Coefficients of Mixtures Adsorbed on Heterogeneous Surfaces. *Aiche Journal* **1983,** *29* (4), 691-693.

142.   Tien, C., *Adsorption calculations and modeling*. Butterworth-Heinemann: Newton, MA, 1994.

143.   Do, D. D., *Adsorption Analysis: Equilibria and Kinetics*. World Scientific: 1998; Vol. 2.

144.   Llano-Restrepo, M.; Mosquera, M. A., Accurate correlation, thermochemistry, and structural interpretation of equilibrium adsorption isotherms of water vapor in zeolite 3A by means of a generalized statistical thermodynamic adsorption model. *Fluid Phase Equilibria* **2009,** *283* (1-2), 73-88.

145.   Ladshaw, A.; Yiacoumi, S.; Tsouris, C.; DePaoli, D., Generalized gas-solid adsorption modeling: Single-component equilibria. *Fluid Phase Equilibria* **2015,** *388*, 169-181.

146.   Aspromonte, S. G.; Mizrahi, M. D.; Schneeberger, F. A.; López, J. M. R.; Boix, A. V., Study of the Nature and Location of Silver in Ag-Exchanged Mordenite

Catalysts. Characterization by Spectroscopic Techniques. *The Journal of Physical Chemistry C* **2013,** *117* (48), 25433-25442.

147.   Aspromonte, S. G.; Serra, R. M.; Miró, E. E.; Boix, A. V., AgNaMordenite catalysts for hydrocarbon adsorption and deNO x processes. *Applied Catalysis A: General* **2011,** *407* (1), 134-144.

148.   Aspromonte, S. G.; Miró, E. E.; Boix, A. V., FTIR studies of butane, toluene and nitric oxide adsorption on Ag exchanged NaMordenite. *Adsorption* **2012,** *18* (1), 1-12.

149.   Chapman, K. W.; Chupas, P. J.; Nenoff, T. M., Radioactive iodine capture in silver-containing mordenites through nanoscale silver iodide formation. *J Am Chem Soc* **2010,** *132* (26), 8897-9.

150.   Scheele, R. D.; Burger, L. L., Evaluation of Silver Mordenite for Radioiodine Retention at the Purex Process Facility Modification, PNL-626 1. *Pacific Northwest Laboratory (July 1987)* **1987**.

151.   Ranz, W. E.; Marshall, W. R., Evaporation from drops. *Chem Eng Prog* **1952,** *48* (3), 141446.

152.   Poling, B. E.; Prausnitz, J. M.; O'connell, J. P., *The properties of gases and liquids*. Mcgraw-hill New York: 2001; Vol. 5.

153. Reháková, M.; Sopková, A.; Šepelák, V.; Briančin, J.; Wadsten, T., Natural zeolitic material of the clinoptilolite type and its AgI form. *Journal of Inclusion Phenomena and Macrocyclic Chemistry* **1995,** *23* (2), 157-163.

154. Lemmon, E. W.; Huber, M. L.; McLinden, M. O., NIST reference fluid thermodynamic and transport properties–REFPROP. *NIST standard reference database* **2002,** *23*, v7.

155. Do, D. D., *Adsorption Science and Technology: Proceedings of the Second Pacific Basin Conference on Adsorption Science and Technology: Brisbane, Australia, 14-18 May 2000*. World Scientific: 2000.

156. Abdallah, K.; Grenier, P.; Sun, L. M.; Meunier, F., Nonisothermal adsorption of water by synthetic NaX zeolite pellets. *Chem Eng Sci* **1988,** *43* (10), 2633-2643.

157. Sing, K. S., Reporting physisorption data for gas/solid systems with special reference to the determination of surface area and porosity (Recommendations 1984),IUPAC Commission on Colloid and Surface Chemistry. *Pure Appl Chem* **1985,** *57* (4), 603-619.

158. Chapman, K. W.; Chupas, P. J.; Nenoff, T. M., Radioactive Iodine Capture in Silver-Containing Mordenites through Nanoscale Silver Iodide Formation. *Journal of the American Chemical Society* **2010,** *132* (26), 8897.

159. Nan, Y.; Abney, C.; Choi, S.; Tavlarides, L. L. In *Aging Processes of Ag-Exchanged Mordenite and Ag-Functionalized Silica Aerogel in Spent Nuclear Fuel*

Reprocessing Off Gases, 2017 AIChE Annual Meeting, Minneapolis, MN, Minneapolis, MN, 2017.

160.   Yue Nan; Seungrag Choi; AustinP. Ladshaw; Sotira. Yiacoumi; Costus. Tsouris; David W. DePaoli; Tavlarides., L. L., Aging processes of silver mordenite and silver functionalized aerogel in dry air, humid air and NO/N2. In *2017 ANS Anual Meeting*, Transactions of the American Nuclear Society 2017; Vol. 116, pp 130-132.

161.   Bruffey, S. H.; Spencer, B. B.; Strachan, D. M.; Jubin, R. T.; Soelberg, N. R.; Riley, B. J. *A Literature Survey to Identify Potentially Volatile Iodine-Bearing Species Present in Off-Gas Streams*; INL/EXT--15-35609 United States 10.2172/1235202 INL English; ; Idaho National Laboratory (INL), Idaho Falls, ID (United States): 2015; p Medium: ED; Size: 41 p.

Vita

NAME OF AUTHOR: Yue Nan

PLACE OF BIRTH: Changzhi, Shanxi, China

GRADUATION AND UNDERGRADUATE SCHOOLS ATTENDED:

Bachelor of Science, 2011;

Department of Chemical Engineering, Tianjin University of Science and Technology

Tianjin, China.

Master of Science, 2013;

Department of Biomedical and Chemical Engineering, Syracuse University

Syracuse, New York, USA.

POSSESSIONAL EXPERIENCE

Department of Biomedical and Chemical Engineering, Syracuse University

Teaching Assistant, 2013, 2014, 2015

Research Assistant, 2015 - present